

## Active Sensing-Based Prognostics of Structural Integrity in Composite Structures Utilizing Deep Learning

Gul, F.C.

**DOI**

[10.4233/uuid:242e006a-6027-47b8-9f65-8139ed040783](https://doi.org/10.4233/uuid:242e006a-6027-47b8-9f65-8139ed040783)

**Publication date**

2025

**Document Version**

Final published version

**Citation (APA)**

Gul, F. C. (2025). *Active Sensing-Based Prognostics of Structural Integrity in Composite Structures Utilizing Deep Learning*. [Dissertation (TU Delft), Delft University of Technology].  
<https://doi.org/10.4233/uuid:242e006a-6027-47b8-9f65-8139ed040783>

**Important note**

To cite this publication, please use the final published version (if applicable).  
Please check the document version above.

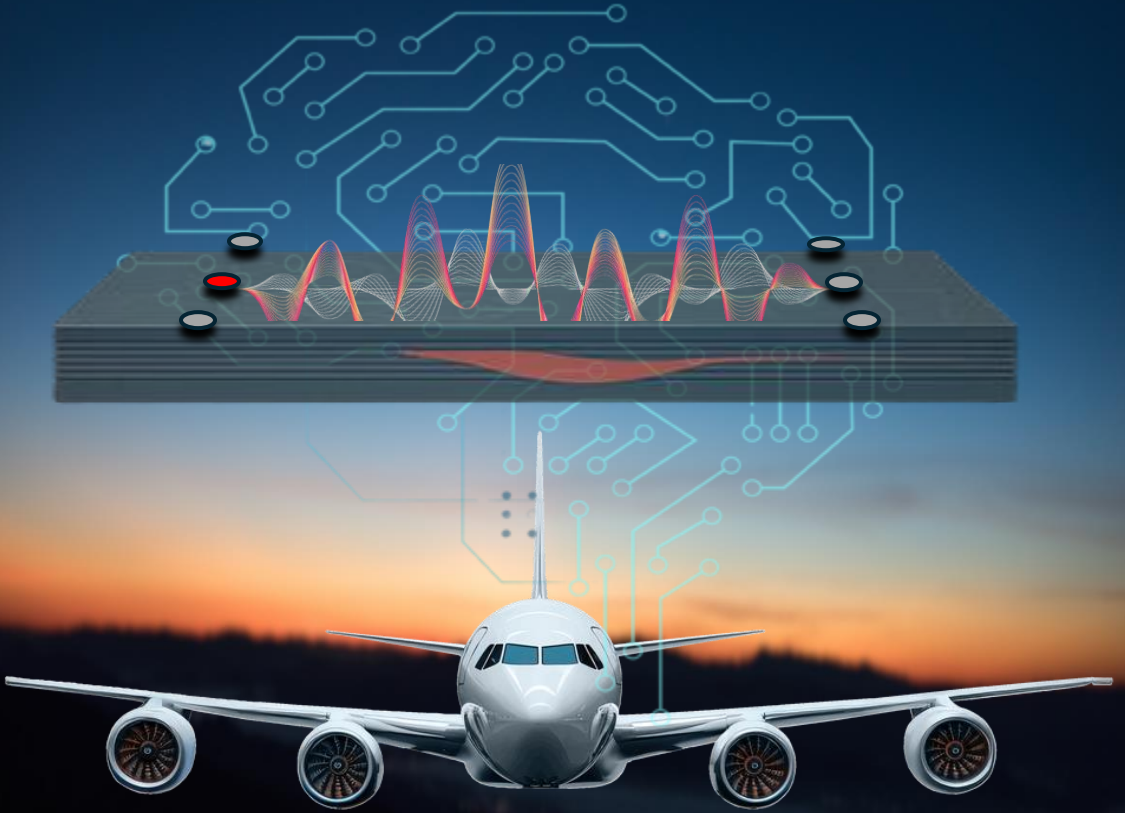
**Copyright**

Other than for strictly personal use, it is not permitted to download, forward or distribute the text or part of it, without the consent of the author(s) and/or copyright holder(s), unless the work is under an open content license such as Creative Commons.

**Takedown policy**

Please contact us and provide details if you believe this document breaches copyrights.  
We will remove access to the work immediately and investigate your claim.

**ACTIVE SENSING-BASED PROGNOSTICS  
OF STRUCTURAL INTEGRITY  
IN COMPOSITE STRUCTURES  
UTILIZING DEEP LEARNING**



**FERDA CANSU GÜL**

# **Active Sensing-Based Prognostics of Structural Integrity in Composite Structures Utilizing Deep Learning**



# **Active Sensing-Based Prognostics of Structural Integrity in Composite Structures Utilizing Deep Learning**

## **Dissertation**

for the purpose of obtaining the degree of doctor  
at Delft University of Technology  
by the authority of the Rector Magnificus Prof.dr.ir. T.H.J.J. van der Hagen,  
chair of the Board for Doctorates  
to be defended publicly on  
Thursday 25<sup>th</sup> September 2025 at 12:30 o'clock

by

**Ferda Cansu GÜL**

Master of Science in Information and Communication Engineering  
Istanbul Technical University  
born in Istanbul, Türkiye

This dissertation has been approved by the promotor.

Composition of the doctoral committee:

Rector Magnificus,	Chairperson
Prof. dr. ire R. Benedictus,	Delft University of Technology, promotor
Dr. D. Zarouchas,	Delft University of Technology, promotor

*Independent members:*

Prof. R.C. Alderliesten,	Delft University of Technology
Prof. I. Mueller,	Bochum University
Prof. N. Mechbal,	École Nationale Supérieure d'Arts et Métiers
Prof. R. De Breuker,	Delft University of Technology
Dr. N. Eleftheroglou,	Delft University of Technology



The thesis was conducted under the European Union's Horizon 2020 program, supported by Marie Skłodowska-Curie grant No. 860104, titled "GW4SHM: European training Network in Guided waves for Structural Health Monitoring".

Keywords: Structural health monitoring; Prognostics; Artificial intelligence; Deep neural networks; Guided waves; Data-driven models; Fatigue; Impact damage; Delamination; Composite structures.

*Printed by:* Ipskamp printing

*Front & Back:* Cover design by Ferda Cansu Gul, with AI-generated elements.

Copyright © 2025 by Ferda Cansu Gul

All rights reserved. No part of this publication may be reproduced, stored in a retrieval system or transmitted in any form or by any means, electronic, mechanical, photocopying, recording or otherwise, without the prior written permission of the author.

ISBN (E-book) 978-94-6518-122-6

ISBN (Paperback) 978-94-6384-846-6





# Summary

The aerospace industry has embraced composite structures like Carbon Fiber Reinforced Polymers (CFRP), which offer superior strength-to-weight ratios, improving fuel efficiency and reducing emissions. However, these advancements come with new challenges in the sense of complex damage mechanisms, particularly delamination, often invisible from the surface, can severely compromise structural integrity, making its timely diagnosis and prognosis essential to maintaining safety and reliability. This thesis explores innovative approaches to monitor impact-induced delamination progression and improve RUL predictions in CFRP structures. The motivation is, as the use of composite structures increases in high-stakes industries like aerospace, so too must the sophistication of the tools used to ensure their continued airworthiness. Monitoring delamination, a form of damage where layers within the composite separate under stress, is crucial and critical to preventing failure. Yet, understanding and predicting its progression under varying loads has remained elusive.

Therefore, this thesis undertakes an experimental and data-driven investigation to develop and validate advanced prognostic methodologies incorporating delamination progression and predicting the remaining useful life (RUL) of impacted composite structures under compressive fatigue loading. The conducted research begins with the design and implementation of a mechanical testing setup involving low-velocity impact testing of CFRP specimens, followed by adaptation to compression–compression (C-C) fatigue loading. Two active sensing-based structural health monitoring (SHM) techniques, Guided Waves (GW) and Electromechanical Impedance (EMI), are integrated into the experimental campaign, and delamination states are labeled using ultrasonic c-scan measurements to enable correlation with physical damage progression.

In the next stage, this thesis presents a series of novel data-driven prognostic frameworks aimed at understanding and predicting the RUL of composite structures subjected to compressive fatigue and experiencing impact-induced delamination-driven failure. The overall RUL prognostic strategy is structured around four primary approaches, each addressing a specific challenge in active sensing-based SHM and prognostics.

The first approach involves a detailed investigation into the diagnostic capabilities of GW and EMI-based damage indicators. Through advanced signal processing techniques, these indicators are evaluated for their sensitivity to delamination progression and their effectiveness in contributing to RUL predictions. This phase lays the foundation for understanding the diagnostic relevance of GW and EMI features in tracking fatigue-induced degradation, while also addressing key challenges related to modeling progressive, sub-surface damage under realistic loading conditions.

The second approach focuses on the integration of GW and EMI sensing modalities within the RUL prognostic framework using various fusion methodologies. This investigation explores how the complementary nature of these techniques improves prognostic accuracy across different initial impact severities and compressive fatigue regimes. By assessing the performance of each modality at different stages of damage evolution, including early onset and advanced delamination. This approach reveals how GW and EMI contribute differently to RUL prediction and how their integration enhances robustness across varied damage scenarios.

The third approach examines the relationship between delamination size prediction and RUL estimation using two distinct data-driven frameworks based solely on GW-derived damage indicators. The first

framework investigates the sensitivity of individual sensor–actuator paths to both delamination length and RUL estimation independently, providing insight into the spatial selectivity of damage detection and prediction. The second framework adopts a more generalized, sample-based perspective, analyzing correlations between predicted delamination size and RUL across specimens. This dual-level investigation offers valuable insights into how delamination growth dynamics influence fatigue life estimation and the degree to which shared indicators can reflect both physical damage and remaining life.

The final approach introduces a multi-level framework that combines GW signal representations with engineered features as parallel inputs to a deep neural network (DNN) architecture. Inputs such as signal envelopes, wavelet-transformed components, and damage indicators are processed collectively to model complex relationships between the sensing data and RUL outcomes. By embedding domain-specific knowledge into the model architecture, this approach improves predictive accuracy, generalization across loading conditions, and interpretability in varying delamination growth regimes.

Ultimately, this thesis is dedicated to presenting a comprehensive approach to monitoring and predicting the degradation of composite structures, addressing critical gaps in current SHM and RUL prognostic methodologies. By combining active sensing techniques with advanced AI-driven models, the research advances the field of SHM and provides a pathway toward more reliable, efficient, and safer maintenance practices in the aerospace industry. These contributions mark a significant step forward in ensuring the continued performance and safety of composite structures in aircraft, supporting the industry's shift towards lighter, more fuel-efficient designs while safeguarding against the hidden risks of delamination-induced failure.

# Samenvatting

In de afgelopen jaren heeft de luchtvaartindustrie composietstructuren zoals koolstofvezelversterkte polymeren (CFRP) omarmd, vanwege hun uitstekende sterkte-gewichtsverhouding. Dit leidt tot een verbeterde brandstofefficiëntie en lagere emissies. Deze vooruitgang brengt echter ook nieuwe uitdagingen met zich mee, vooral op het gebied van complexe schadevormen. Een belangrijke hiervan is delaminatie: een vorm van schade waarbij lagen in het materiaal van elkaar losraken. Omdat dit vaak niet zichtbaar is aan de buitenkant, kan het de structurele integriteit ernstig aantasten. Tijdige diagnose en prognose zijn dan ook essentieel voor het waarborgen van veiligheid en betrouwbaarheid.

Deze scriptie richt zich op innovatieve methoden om delaminatie, veroorzaakt door impact, te monitoren en de resterende levensduur (RUL) van CFRP-structuren beter te voorspellen. De motivatie hiervoor ligt in het feit dat, naarmate het gebruik van composieten in kritieke sectoren zoals de luchtvaart toeneemt, ook de technieken om hun luchtwaardigheid te waarborgen geavanceerder moeten worden. Het monitoren van delaminatie is cruciaal om falen van structuren te voorkomen. Toch blijft het begrijpen en voorspellen van de ontwikkeling van deze schade onder verschillende belastingen een uitdaging.

Daarom richt dit onderzoek zich op een experimentele en data-gedreven benadering om geavanceerde prognostische methoden te ontwikkelen en te valideren. Deze methoden houden rekening met de voortgang van delaminatie en zijn gericht op het voorspellen van de resterende levensduur van composietstructuren die blootgesteld zijn aan vermoeiingsbelasting onder druk. Het onderzoek start met het opzetten van een mechanische testopstelling, waarin CFRP-proefstukken worden blootgesteld aan impact met lage snelheid. Vervolgens worden deze onderworpen aan cyclische drukbelasting (compressie-compressie vermoeiing). Twee actieve meetmethoden voor structurele gezondheid (SHM) – geleidende golven (Guided Waves, GW) en elektromechanische impedantie (EMI) – worden geïntegreerd in het testtraject. Delaminatie wordt in kaart gebracht met behulp van ultrasonische C-scanmetingen, zodat de meetdata kunnen worden gekoppeld aan fysieke schadeontwikkeling.

In het vervolg presenteert deze scriptie een reeks vernieuwende, data-gedreven prognostische benaderingen die zich richten op het begrijpen en voorspellen van de resterende levensduur van composietstructuren onder drukvermoeiing en delaminatie als gevolg van impact. De algehele RUL-strategie bestaat uit vier hoofdbenaderingen, elk gericht op een specifieke uitdaging binnen actieve SHM en prognostiek.

De eerste benadering onderzoekt de diagnostische waarde van schade-indicatoren gebaseerd op GW en EMI. Door gebruik te maken van geavanceerde signaalverwerkingstechnieken worden deze indicatoren beoordeeld op hun gevoeligheid voor delaminatie en hun bijdrage aan RUL-voorspellingen. Deze fase vormt de basis voor het begrijpen van de rol van GW- en EMI-kenmerken in het volgen van schade onder realistische vermoeiingsbelasting.

De tweede benadering richt zich op de integratie van GW- en EMI-metingen binnen het RUL-raamwerk via verschillende fusietechnieken. Hier wordt onderzocht hoe deze technieken elkaar aanvullen en hoe dit de nauwkeurigheid van prognoses verbetert bij verschillende impactniveaus en vermoeiingsregimes. Door de prestaties van elke methode te evalueren bij zowel beginnende als gevorderde schade, wordt duidelijk hoe hun combinatie bijdraagt aan robuustere voorspellingen.

De derde benadering onderzoekt het verband tussen de voorspelling van de delaminatiegrootte en de RUL-inschatting, met twee data-gedreven modellen gebaseerd op uitsluitend GW-indicatoren. Het eerste model bekijkt de gevoeligheid van afzonderlijke sensor-actuator paden voor delaminatielengte en RUL afzonderlijk. Het tweede model kijkt naar het grotere geheel en analyseert hoe de voorspelde schadegrootte samenhangt met de resterende levensduur van verschillende proefstukken. Deze aanpak biedt waardevol inzicht in hoe schadegroei de vermoeiingslevensduur beïnvloedt.

De vierde en laatste benadering introduceert een meerlagig datafusie-model waarbij ruwe GW-signalen worden gecombineerd met bewerkte kenmerken als invoer voor een deep neural network (DNN). Invoervariabelen zoals signaalomhullende, waveletcomponenten en globale schade-indicatoren worden gezamenlijk verwerkt om complexe verbanden tussen meetdata en levensduur te modelleren. Door vakspecifieke kennis in de modelarchitectuur op te nemen, wordt de nauwkeurigheid, generaliseerbaarheid en interpretatie van de voorspellingen verbeterd.

Uiteindelijk biedt deze scriptie een integrale benadering voor het monitoren en voorspellen van degradatie in composietstructuren. Hiermee worden belangrijke tekortkomingen in de huidige SHM- en RUL-methoden aangepakt. Door actieve meetsystemen te combineren met geavanceerde AI-modellen, levert dit onderzoek een bijdrage aan de verdere ontwikkeling van SHM en biedt het handvatten voor betrouwbaardere en efficiëntere onderhoudspraktijken in de luchtvaartindustrie. Deze bijdrage is een belangrijke stap richting het veilig en duurzaam gebruik van lichtere, brandstofefficiënte vliegtuigstructuren, waarbij de verborgen risico's van delaminatie actief worden beheerst.

# Contents

1.Introduction .....	1
1.1. Background & Motivation .....	2
1.2. Review of Existing Research .....	4
1.3. Conclusion .....	13
1.4. Contributions.....	14
1.5. Thesis Outline .....	16
2.Methodological Framework .....	17
2.1. Introduction.....	20
2.2. Background of Methodological Components .....	21
2.2.1. C-C Fatigue Testing.....	21
2.2.2. Piezoelectric (PZT) Transducers .....	22
2.2.3. Electromechanical Impedance (EMI) Technique.....	23
2.2.4. Guided Wave (GW) Technique.....	23
2.3. Determining EoL .....	25
2.4. Signal Processing Techniques.....	26
2.4.1. Hilbert Transform .....	27
2.4.2. Continuous Wavelet Transform.....	27
2.4.3. Discrete Wavelet Transform.....	28
2.5. Deep Learning for Non-Linear Regression.....	29
2.5.1. Multilayered Perceptron .....	29
2.5.2. Convolutional Neural Networks.....	29
2.5.3. Long-Short Term Memory .....	30
2.5.4. Optimization and Regularization.....	32
2.5.5. Normalization .....	33
3.Compression-Compression Fatigue Testing after Impact.....	35
3.1. Introduction.....	36
3.2. CAI Test for Woven Composite Structures .....	36
3.2.1. Desing of the CAI Experimental Setup .....	36
3.2.2. Fatigue Testing .....	38
3.3. Delamination State Labels .....	40
3.3.1. Ultrasonic C-scan Technique.....	40
3.3.2. Determination of Threshold Levels.....	42
3.4. Implementation of Active-sensing based SHM Techniques in CAI Testing.....	44
3.4.1. SHM Implementation in CAI Testing .....	44
3.4.2. EMI Acquisition .....	45
3.4.3. GW Acquisition.....	45

4. Progressive Delamination Characterization via GWs & EMIs.....	51
4.1. Introduction.....	52
4.2. Methodology.....	52
4.2.1. EMI-Damage Indicator.....	52
4.2.2. Guided Wave Damage Indicators.....	53
4.2.3. Global DIs.....	57
4.3. EMI & GW DIs for Progressive Delamination Monitoring.....	57
4.4. Prognostic Metrics.....	64
4.5. Conclusion.....	66
5. RUL Prognosis via Integration of Active Sensing SHM Methods: EMI & GW.....	67
5.1. Introduction.....	68
5.2. Methodology.....	68
5.2.1. Input Organization.....	69
5.2.2. Model Architecture and Training-Testing.....	69
5.2.3. Fusion Methodology.....	71
5.3. Results.....	72
5.4. Conclusion.....	76
6. Prognosis of RUL with Delamination Growth via GW-SHM.....	77
6.1. Introduction.....	78
6.2. Methodology.....	78
6.2.1. Input Organization.....	78
6.2.2. Model Architecture.....	79
6.3. Results.....	80
6.3.1. Path-Sensitivity Analysis.....	80
6.3.2. Ensembled-Dataset-based Prediction.....	84
6.4. Discussion.....	85
6.5. Conclusion.....	86
7. Prognosis: Blending Deep Learning with Signal Processing.....	89
7.1. Introduction.....	90
7.2. Methodology.....	90
7.2.1. Input Organization.....	90
7.2.2. Model Architecture.....	92
7.3. Results.....	95
7.4. Discussion.....	100
7.5. Conclusion.....	100
8. Conclusion & Future Research.....	101
8.1. Discussion of Research Outcomes and Limitations.....	102
8.2. Suggestions for Future Work.....	105

---

8.3. Final Remarks .....	106
References .....	107
Acknowledgments .....	115
Curriculum Vitae.....	117
List of Publications.....	119



# Nomenclature

## Symbols

$N_{cycle}$	Number of cycles
$N_{path}$	Number of paths
$N_{DI}$	Number of DI
$F_{min}$	Minimum applied load
$F_{max}$	Maximum applied load
$\Psi(t)$	Wavelet function
$a_m^l$	Input neuron
$f_{exc}$	Excitation frequency
$\nu$	Exponential average of gradients
$\beta$	Exponential decay control parameter
$g$	Gradient
$\eta$	Initial Learning Rate
$\omega$	Weight
$s$	Exponential average of squares of $g$
$x$	One data point
$\bar{Y}_d^{l,m}$	Long-Short Term Memory
$\bar{Y}_d^{l,p}$	Multi-Layer Perceptron
$\bar{Y}_R^{l,m}$	Piezoelectric Transducer
$\bar{Y}_R^{l,p}$	Remaining Useful Life
$V_{wave}$	Wave velocity
$\lambda_{wave}$	Wavelength
$c_p$	Phase velocity
$c_g$	Group velocity
$\mu$	Mean value
$\sigma$	Standard deviation
$Z_p$	Impedance of PZT
$Z_s$	Impedance of structure

**Abbreviations**

AI	Artificial Intelligence
AE	Acoustic Emission
CAI	Compression After Impact
CBM	Condition Based Maintenance
CFRP	Carbon Fiber Reinforced Polymer
CNN	Convolutional Neural Network
CWT	Continuous Wavelet Transform
DI	Damage Indicator
DIC	Digital Image Correlation
DL	Deep Learning
DNN	Deep Neural Networks
DWT	Discrete wavelet transform
EMI	Electromechanical Impedance
EoL	End of Life
FBG	Fiber Optic Sensors
GW	Guided Wave
HT	Hilbert Transform
LOOCV	Leave one out cross validation
LSTM	Long-Short Term Memory
MAE	Mean Absolute Error
MARE	Mean Absolute Relative Error
MLP	Multi-Layer Perceptron
MSE	Mean Squared Error
PZT	Piezoelectric Transducer
RUL	Remaining Useful Life
ReLU	Rectified Linear Unit
SHM	Structural Health Monitoring
SGD	Stochastic Gradient Descent
WAP	Windowed Averaged Power
RMSD	Root Mean Squared Deviation

# List of Figures

Figure 1.1. Active sensing-based SHM framework for CBM.....	3
Figure 1.2. RUL prognostic elements. ....	4
Figure 1.3. The characteristic fatigue damage states during the fatigue life of composite laminates (adopted from [11]). ....	6
Figure 1.4. Delamination-induced failure modes under compressive loading.....	7
Figure 2.1. Methodological frameworks investigated in this thesis and their key componenets.....	20
Figure 2.2. Standard anti-buckling test fixture for ASTM D7137/D7137M [89].....	21
Figure 2.3. PZT sensor surface-attached on testing sample.....	22
Figure 2.4. Presentation of (a) disk shaped PZT with geometrical parameters (b) circular and rectangular PZT with wave-field direction [90].....	22
Figure 2.5. Thin plate configuration.....	24
Figure 2.6. (a) Symmetric $S_0$ and (b) antisymmetric $A_0$ modes of GWs. ....	25
Figure 2.7. Structural degradation through delamination damage and RUL relation. ....	26
Figure 2.8. Example of mother wavelets .....	28
Figure 2.9. Neuron functions in feed-forward propagation. ....	29
Figure 2.10. CNN architecture with input layer convoluntinal layer, pooling layer, fully connected layer and output layer. ....	30
Figure 2.11. A unit of a LSTM cell.....	31
Figure 3.1. (a) Large healthy state panel; (b) cutting layout. ....	36
Figure 3.2. Microscopic image from the side edge of cutted CFRP sample.....	36
Figure 3.3. Impact testing setup (left) and impact energy calculation parameters (right). ....	37
Figure 3.4. (a) Anti-buckling fixture and sensor-installed sample (b) SHM unit and fatigue testing MTS machine. ....	37
Figure 3.5. Data collection steps. ....	38
Figure 3.6. Fatigue loading and data acquisition steps. ....	39
Figure 3.7. Final failure; front view and side edge views of two different samples. ....	39
Figure 3.8. Pulse-echo NDT kit. ....	41
Figure 3.9. Ultrasonic c-scan images of delamination from six samples present gradual growth in their three-fatigue life level: initial, middle, final/threshold. ....	42
Figure 3.10. Sample 7 delamination labels. ....	43
Figure 3.11. a) Delamination growth until EoL, b) RUL.....	43
Figure 3.12. a) Measured delamination length for Sample 9, b) RUL definition, c) RUL for all samples.....	43
Figure 3.13. SHM framework integrating GW, EMI, and ultrasonic C-scan .....	44
Figure 3.14. (a) Schematic diagram of sensor placement (b) sensor network installed sample. ....	45
Figure 3.15. Admittance magnitude of no-damage samples for 6 PZTs.....	45
Figure 3.16. Excitation signal in time and frequency domain. ....	46
Figure 3.17. Signal pre-processing and denoising flowchart. ....	47
Figure 3.18. Raw GW signal cross-talk removal. ....	48
Figure 3.19. GW signal denoising steps.....	49
Figure 3.20. Surface-attached PZT network and actuator-sensor path labels. ....	50
Figure 3.21. Received GW signals from healthy state path no 5. ....	50
Figure 4.1. Initial and final state comparison for 6 PZTs of Sample 2. ....	52
Figure 4.2. Envelope representation of GW signals from the path no 3, 180 kHz center frequency excitation signal.....	55

Figure 4.3. GW signals CWT representation at each excitation frequency from the path no 3 in final delamination state of Sample 2. ....	56
Figure 4.4. Signal average power (AP) calculated from the path no 3 of Sample 2. ....	56
Figure 4.5. Methodological framework for global GW-DIs and EMI-DIs. ....	57
Figure 4.6. EMI-DIs and delamination growth for all samples in set. ....	59
Figure 4.7. GW-DIs for each excitation frequencies of all samples. ....	62
Figure 4.8. GW- DIs and delamination growth for all samples with highest score <i>f<sub>exc</sub></i> . ....	63
Figure 4.9. Monotonicity metric for (a) EMI-DIs and (c) GW-DIs; Correlation metric for (b) EMI-DIs and (d) GW-DIs. ....	65
Figure 4.10. Fitness for a) EMI-DIs per sample, b) EMI-DIs averaging all samples for each PZT. ....	65
Figure 4.11. Fitness for (a) GW-DIs averaged over all samples and (b) GW-DIs averaged over each DIs. ....	65
Figure 5.1. Schematic of proposed RUL prognostic. ....	68
Figure 5.2. Input set preparation steps. ....	69
Figure 5.3. DNN scheme for RUL prognostic framework. ....	70
Figure 5.4. Proposed fusion methodologies to integrate RUL predictions obtained from both EMI-based and GW-based prognostic models. Fusion 1 represents the weighted average ensemble (WAE), and Fusion 2 has a deep learning basis. ....	72
Figure 5.5. RUL prediction results. ....	73
Figure 5.6. RUL prediction accuracy scores for each sample. ....	74
Figure 5.7. Average normalized error for each sample. ....	75
Figure 5.8. Average normalized error for each RUL model. ....	75
Figure 6.1. Dataset types and learning models. ....	79
Figure 6.2. Error values for (a) delamination length prediction of each path (b) delamination length prediction of each cycle and for c) RUL prediction of each path d) RUL prediction of each cycle. ....	82
Figure 6.3. Comparison of the best results of delamination length prediction with the RUL predictions of the same path. ....	83
Figure 6.4. Comparison of the best results of RUL prediction with the delamination length predictions of the same path. ....	84
Figure 6.5. Test results of delamination length predictions. ....	85
Figure 6.6. Test results of RUL predictions. ....	85
Figure 7.1. Input organization based on GW signals in time and time-frequency domain and with GW-DIs. ....	91
Figure 7.2. Path-averaged correlation values for DI-Env and DI-CWT vs measured delamination length. ....	91
Figure 7.3. Overall proposed framework including base learners and fusion steps at different levels. ....	92
Figure 7.4. 1D CNN base learner. ....	93
Figure 7.5. MLP architecture for base and fusion learner. ....	94
Figure 7.6. LSTM fusion model. ....	94
Figure 7.7. Base learner prediction results with Level-1 fusion for the excitation frequency of highest accuracy. ....	97
Figure 7.8. RUL prediction from different levels (L1 and L2) composed of different models. ....	99

# List of Tables

Table 2-1. Target sets as delamination length and RUL. ....	26
Table 3-1. Test parameters of CAI fatigue testing .....	40
Table 3-2. Signal acquisition parameters. ....	46
Table 5-1. Hyperparameters of proposed models M-EMI and M-GW.....	71
Table 5-2. Hyperparameters of the model “M-fuse”.....	72
Table 6-1. Hyperparameters of learning model Type 1 in Framework #1.....	80
Table 6-2. Hyperparameters of learning model Type 2 in Framework #2.....	80
Table 6-3. Hyperparameters of learning model Type 3 in Framework #3.....	80
Table 7-1. CNN-Base learner architectural parameters. ....	93
Table 7-2. MLP-Base learner architectural parameters.....	93
Table 7-3. MLP-L1-Fusion model architectural parameters.....	95
Table 7-4. MLP-L3-Fusion model architectural parameters.....	95
Table 7-5. LSTM-L3-Fusion model architectural parameters. ....	95
Table 7-6. Base Learner average error values. ....	98
Table 7-7. Averaged MAPE error values for RUL prediction from each fusion level.....	100



# 1 Introduction

## 1.1 Background & Motivation

Driven by the need for lighter, more fuel-efficient, and high-performance aircraft, the aerospace industry has increasingly integrated composite materials into modern design and manufacturing. This transition has significantly improved aircraft performance, particularly in fuel efficiency and overall structural performance. Polymer composite materials, such as Carbon Fiber Reinforced Polymers (CFRP), are prized for their ability to offer high strength while reducing the overall weight of aircraft, leading to better fuel economy and lower emissions. For instance, Boeing's 787 and Airbus's A350 feature a high proportion of composite materials in their airframes with over 50% of the aircraft's structure is made from advanced composites [1]. However, alongside these benefits come unique challenges; their heterogeneous nature introduces complexities in their behaviors, particularly their susceptibility to impact damage. This damage can compromise the structural integrity of the aircraft's primary structural components, making it difficult to detect until the damage is severe. Consequently, the need for effective monitoring and prognostic systems has become critical in ensuring composite aerospace structures' continued safety and airworthiness.

The motivation for this research is deeply rooted in the necessity to enhance the safety and reliability of aerospace structures, particularly those made from advanced composite materials. The increasing reliance on these materials demands an equally advanced approach to their maintenance and monitoring. Delamination, a common and hazardous form of damage in composites, poses a significant challenge under fatigue conditions. Delamination occurs when layers within the structure separate, often in a manner that is not visible from the surface, making detection difficult. If left undetected, delamination may progress, leading to catastrophic failure of the component. This damage's hidden, progressive nature drives the urgency for advanced SHM systems that can detect and predict such damage in real-time before it reaches a critical stage, thus preventing potential failures.

RUL prognostics, one of the most challenging levels of SHM, involve estimating the time until a structure reaches a state that necessitates repair or replacement. It is vital for maintaining the safety and reliability of aerospace structures, as it allows for timely and informed maintenance decisions. By understanding and predicting the degradation process, RUL prognostics support a condition-based maintenance strategy, which optimizes maintenance schedules, reduces unnecessary downtime, and extends the life of critical components. The ability to predict accurately the RUL of composite structures is challenging, as it involves understanding complex degradation processes and accounting for the variability introduced by different operational and environmental conditions. Within the framework of SHM, the accurate prediction of a structure's RUL is crucial for several reasons:

- **Safety Assurance:** Accurate RUL prediction helps identify potential failure points before they lead to catastrophic events. By forecasting the lifespan of structural components, maintenance can be scheduled proactively, ensuring that repairs or replacements are performed before a component fails, thus maintaining the structure's safety.
- **Optimized Maintenance:** RUL prognostics enable the implementation of condition-based maintenance (CBM) strategies. Instead of relying on fixed maintenance schedules, CBM allows maintenance actions to be based on the actual condition of the structure. This approach can significantly reduce unnecessary maintenance tasks, lower operational costs, and minimize downtime.
- **Cost Efficiency:** By accurately predicting the remaining components' life, organizations can optimize repair and replacement activities. This reduces both the cost of premature replacements and the risk of unexpected failures, which can be costly in terms of both repair expenses and operational disruptions.
- **Enhanced Reliability:** Accurate RUL predictions improve the reliability of maintenance strategies by providing a clearer understanding of the degradation process and remaining lifespan. This leads

to more informed decision-making regarding when and how to perform maintenance, enhancing overall operational efficiency.

SHM systems, in general, use various sensing technologies and data analysis techniques to continuously monitor the health of structures, enabling real-time monitoring of the structure with the aim of performing damage diagnosis, i.e., identification, localization, quantification of damage, as well as prognosis, i.e., prediction of RUL and supporting informed maintenance decisions. SHM can be divided into passive and active sensing techniques. Passive sensing involves monitoring a structure by observing its natural response to environmental loads, vibrations, or changes without introducing external stimuli. In contrast, active sensing utilizes external stimuli, such as ultrasonic waves, vibrations, or thermal signals, actively applied to the structure to gather detailed data about its condition. In **Figure 1.2**, the SHM framework in the CBM context is shown for the lifetime of an aircraft.

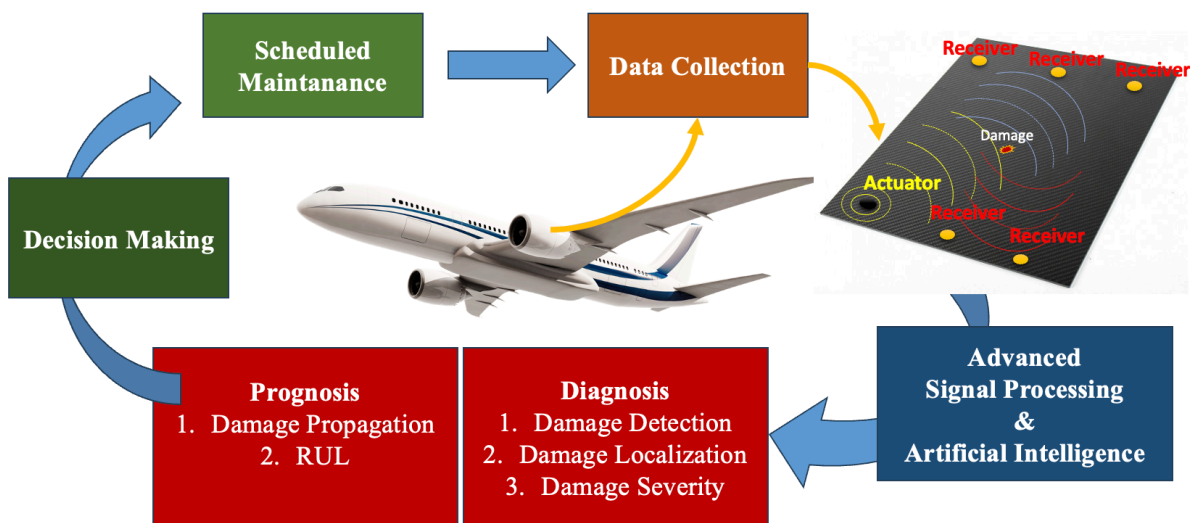


Figure 1.1. Active sensing-based SHM framework for CBM.

**Figure 1.2** illustrates the RUL prognostics from collected SHM data the correlation between the degradation of the composite structure. RUL for composite structures can be defined as the time or number of operational cycles that the structure can safely continue to function before it reaches a critical damage state. In composites, impact damage (e.g., from bird strikes or dropped tools) and delamination significantly reduce the load-bearing capacity and structural integrity over time. RUL estimation considers the extent of this damage, the rate of degradation, and the structure's ability to withstand further loading under operational conditions.

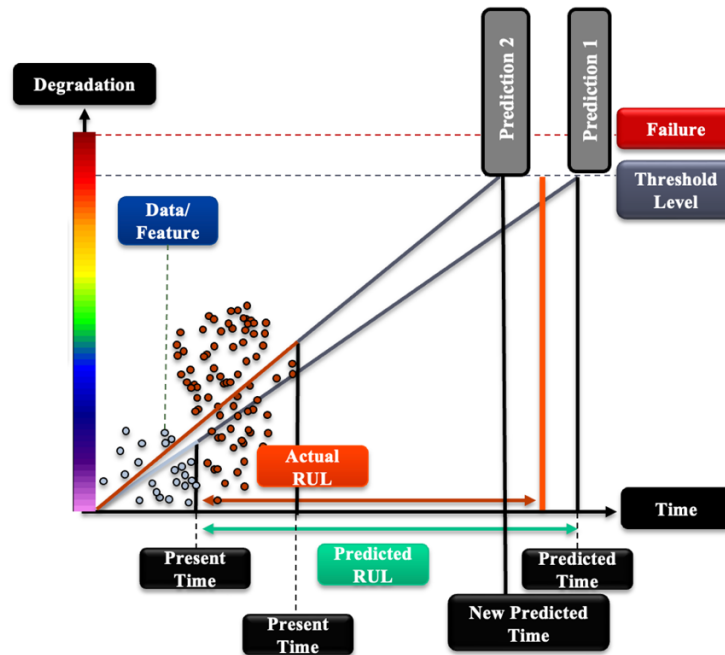


Figure 1.2. RUL prognostic elements.

Active sensing-based SHM techniques, such as GWs and EMI, offer promising solutions for structural assessment by enabling continuous, in-situ monitoring. A practical application of SHM in the aerospace industry can be seen in the Boeing 737 aircraft by Delta Air Lines, which utilizes Acellent's SMART Layer technology, where an integrated network of Piezoelectric transducers (PZT) sensors is attached to the aft pressure bulkhead. These PZT sensors enable real-time structural assessment by generating and receiving ultrasonic GWs, facilitating the detection and quantification of potential damage across a monitored area [2]. GWs, as one of the active sensing techniques, stand out due to their effectiveness in monitoring complex structures. GWs are particularly suited to composite structures used in aerospace due to their ability to propagate over long distances and through varied geometries with minimal energy loss. Integrating GWs into SHM frameworks enhances the ability to monitor complex damage mechanisms in composites, supporting more reliable and efficient maintenance practices and contributing to aerospace structures' overall safety and performance. Furthermore, combining GW technology with complementary SHM techniques, such as EMI monitoring, could further refine damage diagnostics by capturing localized and global structural states and contribute to RUL prognosis.

Advancing research on integrating active sensing-based SHM techniques into robust, data-driven prognostic models for monitoring composite structures under compressive fatigue conditions is essential for developing effective CBM strategies. This study aims to improve RUL prognosis by advancing the understanding of impact-induced delamination behavior under compressive loading, utilizing the GW technique, and complementing it with EMI for improved damage assessment. Ultimately, these advancements in RUL prognostics seek to improve the reliability and safety of aerospace structures, reinforcing the viability of composite materials in high-stakes applications.

## 1.2 Review of Existing Research

Accurately assessing delamination severity is complicated, as delamination may occur and grow at each layer in different shapes and may present an accelerated growth rate after a critical damage severity level. Moreover, determining the critical damage level is also problematic, as variations in initial damage, besides the operational and environmental conditions, may lead to degradation scenarios that differ drastically for each composite structure [3], [4], [5]. As a result, to avoid reaching a critical threshold level, it becomes

essential to uncover the delamination growth in real-time, and that necessitates the development of sophisticated prognostic models that reveal the delamination state and the RUL of the structure that may enable reliable and effective repair decisions that consequently enhance the safety and operational efficiency of composite structures.

This literature review examines the state of the art across five critical areas essential to understanding and advancing this field:

1. **Fatigue Life of Impacted Composite Structures:** Understanding the fatigue behavior of composite structures, especially the onset and growth of delamination due to impact, is foundational to assessing their long-term performance. Research in this area provides insights into how these damages initiate and evolve, which is vital for developing effective monitoring and prognostic strategies.
2. **RUL Prognostics of Composite Structures:** Accurate prediction of the RUL of composite components under various loading conditions is crucial for ensuring timely maintenance and preventing catastrophic failures. This review section will explore different prognostic models and their effectiveness in forecasting the lifespan of composite structures with existing or potential damage.
3. **Guided Wave Structural Health Monitoring (GW-SHM):** This section reviews the interaction between GWs and damage in composite structures, emphasizing the complexities arising from the anisotropic properties of composite materials and the heterogeneous nature of damage mechanisms. Furthermore, it examines the role of GW-based methods in RUL prognostics, discussing advanced signal processing techniques for extracting meaningful features and exploring the potential benefits of integrating complementary SHM approaches to enhance system reliability.
4. **Electromechanical Impedance Structural Health Monitoring (EMI-SHM):** While GW-SHM provides effective global monitoring, EMI techniques offer localized sensitivity to changes in structural properties. Exploring the EMI method allows for a comparative analysis, assessing how EMI can complement the GW approach to enhance the overall RUL prognostic purpose.
5. **Artificial Intelligence (AI)-based Prognostic Techniques:** The integration of AI into SHM systems offers significant potential for improving RUL prognosis. This section will review current advancements in AI applications for SHM, focusing on how they can enhance the effectiveness of both GW and EMI-based systems for RUL prognostics.

Each of these topics contributes to a comprehensive understanding of effectively monitoring and predicting damage and RUL in composite structures. By exploring these areas, this literature review will identify existing gaps and challenges, setting the stage for further research to develop more robust and accurate SHM systems tailored to the needs of modern aerospace applications.

### **Fatigue Life of Impacted Composite Structures**

Composite structures are inherently susceptible to various forms of damage, with impact damage particularly critical due to its potential to significantly reduce load-bearing capacity [6], [7]. Unlike metallic structures, which typically fail through predictable crack growth, composites exhibit more complex and less visible damage mechanisms, such as delamination, fiber-matrix debonding, and matrix cracking. Damage tolerance principles play a crucial role in structural design, certification, and lifecycle management to ensure the continued airworthiness of composite aircraft structures. The damage tolerance approach ensures that aircraft components can sustain operational loads despite the presence of damage, providing sufficient time for detection and repair. The European Union Aviation Safety Agency (EASA) outlines acceptable means of compliance (AMC) that emphasize the critical need for early detection and timely

repair of damage to uphold the damage tolerance characteristics of the structure [8]. Identifying the critical level of damage severity and predicting the time until a structure reaches its failure threshold is exacerbated by the inhomogeneous nature of composite structures, leading to unpredictable degradation patterns [3], [9], [10]. Therefore, developing reliable inspection and monitoring techniques is essential to assess damage evolution and ensure timely maintenance interventions accurately.

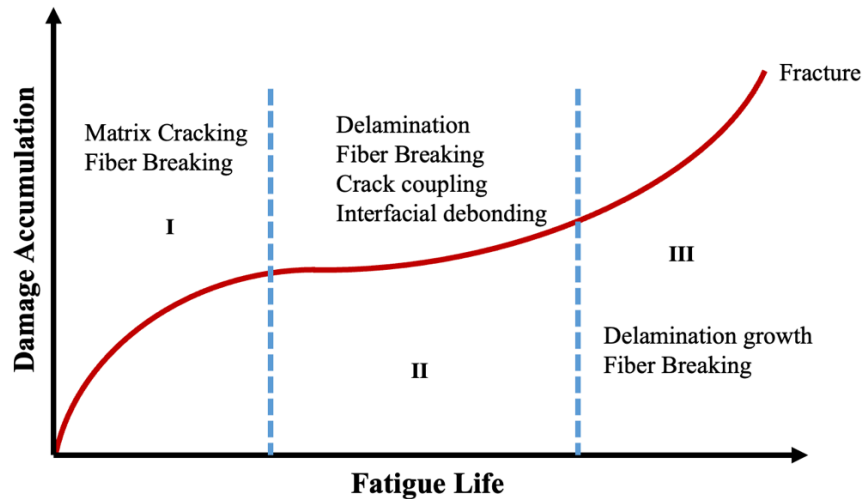


Figure 1.3. The characteristic fatigue damage states during the fatigue life of composite laminates (adopted from [11]).

**Figure 1.3** illustrates the fatigue damage accumulation process in composite structures over their fatigue life, which is divided into three distinct phases. Phase I represents the initial stage of damage formation, characterized by matrix cracking and fiber breaking at the micro-level. Micro-cracks begin to develop at this stage, but their impact on structural integrity remains minimal. The accumulation of damage progresses slowly as the fibers continue to bear the applied loads. Phase II marks the evolution and interaction of damage mechanisms. More complex forms of damage, including delamination, fiber breakage, crack coupling, and interfacial debonding, emerge and interact. This interaction accelerates the overall degradation process, leading to a progressive reduction in stiffness and load-bearing capacity. This phase is particularly critical as the combination of different damage modes enhances structural deterioration. Phase III is characterized by critical damage growth and fracture. Delamination growth and extensive fiber breakage dominate this stage, resulting in a rapid increase in the rate of damage accumulation. The structural integrity is severely compromised, and the structure can no longer sustain operational loads, ultimately leading to catastrophic failure [11], [12], [13]. An unexpected event, such as impact damage, may initiate delamination, fiber-matrix debonding, and with crack interactions, it can accelerate fatigue degradation. Pre-existing impact-induced delaminations propagate rapidly under cyclic loading, which can be categorized under phase III, causing a significant reduction in structural integrity and catastrophic failure. The presence of impact damage thus plays a crucial role in determining the fatigue life of composite structures, as it facilitates damage evolution and accelerates the transition from progressive degradation to structural failure [14], [15].

Delamination growth in composite structures behaves differently under tensile and compressive loading due to variations in stress distribution and failure mechanisms [16], [17]. Under tensile loading, delaminations primarily experience opening-mode (Mode I) loading, where tensile stresses act perpendicular to the crack plane, causing the laminate layers to separate. Since the fibers continue to bear most of the applied load, delamination growth remains gradual, with crack propagation following fiber-matrix debonding and progressive interfacial failure. Under compressive loading, delaminated regions lose out-of-plane stability, leading to buckling-driven failure mechanisms. The presence of delaminations

promotes shear-dominated (Mode II) and tearing (Mode III) failure, where the separated plies experience interlaminar sliding and kinking effects. Furthermore, in compression-after-impact scenarios, delamination growth is driven by the out-of-plane buckling of surface plies, which alters the local stress distribution and accelerates delamination progression [18], [19], [20]. Once the structure reaches a critical damage state or stiffness threshold, localized buckling of surface plies further accelerates degradation, significantly reducing the component's structural integrity [21], [22]. This progressive weakening can further escalate the risk of structural buckling, posing a severe threat to overall structural integrity. In Figure 1.4, the failure modes of impacted CFRP samples are shown after high-cycle compression-compression (C-C) fatigue loading. The images illustrate delamination-induced failure mechanisms, where pre-existing impact damage has progressively worsened due to cyclic compressive stresses.

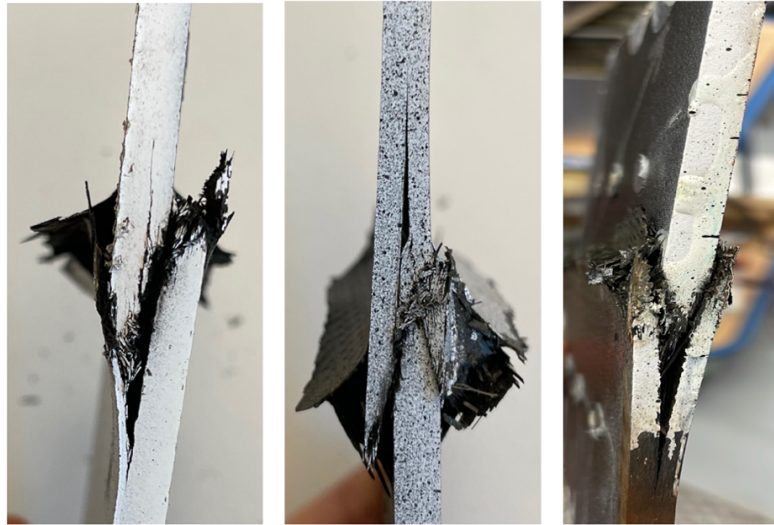


Figure 1.4. Delamination-induced failure modes under compressive loading.

Therefore, it is vital to monitor delamination growth in real-time to prevent reaching critical severity thresholds. Regulatory standards mandate thorough damage severity assessments to identify the potential locations, types, and sizes of damage before they reach critical thresholds, thus facilitating timely maintenance interventions. The challenge of monitoring delamination under compressive loading conditions is further intensified by its tendency to evolve in irregular patterns across multiple layers, often exhibiting unpredictable acceleration once a critical severity threshold is reached. Biagini et al. [23] investigate the sudden growth behavior associated with delamination and propose that its propagation under in-plane compressive loading likely involves intricate interactions between the composite layers and other damage mechanisms, such as matrix cracks. They highlight challenges with non-destructive inspections, noting that these methods, typically employed to measure delamination, might be obscured by the presence of larger delamination layers [13], [23]. Furthermore, variations in initial damage, compounded by differing operational and environmental conditions, can result in highly divergent degradation patterns across individual composite structures. Saleh et al. [24] investigate the Barely Visible Impact Damage (BVID) induced by single and multiple low-velocity impacts on specimens at different locations. Despite identical impact energies being applied, the fabric orientation and location of the damage significantly influence the propagation of delamination and consequently affect the residual strength of the composite structures.

Given the challenges outlined, accurately determining damage growth necessitates incorporating multiscale effects. However, integrating all relevant parameters simultaneously demands highly sophisticated and computationally intensive simulations or complex empirical equations [25], [26], [27]. These mentioned challenges necessitate consideration of the interaction of other damage mechanisms with the delamination in addition to initial damage state, loading history, environmental conditions, and material anisotropy for a

better description of delamination growth and, eventually, for an enhanced understanding of the contributions to the end-of-life (EoL) span of structures and so their RUL.

The complexity of delamination evolution and the unpredictable nature of its propagation under compressive fatigue conditions requires further research to enhance damage characterization techniques. A more comprehensive prognostic framework, one that refines delamination quantification methodologies, is required to achieve greater interpretability in RUL predictions. The following subsection “Prognosis of Composite Structures” critically examines prognostic methodologies, assessing their ability to model degradation phenomena and their effectiveness in accurately monitoring the structural integrity and predicting the RUL of composite structures.

### **Prognosis of Composite Structures**

In the literature, RUL prognostics have been studied for structures through a variety of SHM techniques tailored to specific applications [28], [29], including:

- Acoustic Emission (AE); which detects the high-frequency waves emitted by cracks or defects as they develop, providing early warning of potential structural failures [30].
- Fiber Optic Sensors (FBGs); utilized for their high sensitivity and ability to be embedded within composite structures, allowing for real-time strain measurement and damage detection [31].
- Electromechanical Impedance (EMI); offers localized damage detection, meaning it can precisely identify the presence and extent of damage in specific areas of interest [32].
- Ultrasonic Guided Waves or Lamb Waves for in-plane propagating guided waves (GWs); involves sending high-frequency sound waves through materials and analyzing their reflections to identify internal flaws [33].

Based on the system design and the integration of specific SHM technologies, various approaches can be adapted to implement prognostic methodologies, including data-driven, physics/model-based, or hybrid strategies [34], [35]. Integrating SHM data into model-based prognostic approaches necessitates knowledge of damage propagation mechanisms, which may restrict the model's ability to incorporate complex multi-scale effects. Data-driven techniques, on the other hand, do not rely on physical models; instead, they utilize SHM data to develop models that correlate these data with system degradation, subsequently using these models for RUL predictions. Lastly, hybrid approaches merge both data-driven and physics-based models, leveraging the strengths of each to enhance overall prognostic accuracy, yet, often require significant computational resources, as they must process both physics-based simulations and large-scale machine learning algorithms [36].

The composite structures' heterogeneous nature and the random initiation of various damage mechanisms add layers of complexity to understanding the damage process. This complexity has steered the focus towards data-driven methodologies, which offer the flexibility to adapt to the diverse and stochastic nature of damage in composite structures. Data-driven models are particularly offering high effectiveness in predicting RUL due to their ability to process large datasets with advanced machine learning and statistical techniques [37]. These models correlate large volumes of data with indicators of system degradation, ensuring robust prognostics based on comprehensive data analysis [38]. Data-driven approaches may leverage adaptive learning mechanisms to incorporate new information in real time, continuously refining prediction accuracy [39]. Moreover, they are capable identifying complex patterns that may not be captured by conventional model-based methods [40], [41]. This is particularly crucial for composite structures, where the inherently complex and multi-scale failure mechanisms, evolving under diverse loading conditions, challenge conventional modeling frameworks and necessitate the implementation of data-driven methodologies for enhanced RUL prognostics.

In data-driven methodologies, RUL prediction can be approached in two ways: either directly or through Damage Indicators (DIs) and Health Indicators (HIs). Direct RUL prediction methods aim to estimate the RUL of a composite structure directly from the data, typically without constructing intermediate models of the physical system. HI or DI-based RUL approaches involve extracting specific features or indicators from sensor data or signals that may represent the health state of the composite structure. While HIs may refer to a general projection regarding the health state of the structure, DIs may be aimed to be correlated to specific damage types or states depending on the system's condition. Those features related to the structure's health/damage state are then used to estimate the RUL. Both approaches have advantages and are chosen based on the application, availability of data, and computational resources. Direct RUL approaches offer simplicity and are suitable for scenarios with ample data. In contrast, feature-based approaches provide more interpretability and are often preferred in scenarios where specific damage mechanisms must be monitored and understood. Eleftheroglou et al. [42] explored RUL prognostics using AE techniques, where AE features were utilized as inputs for a data-driven prognostic model to predict the RUL of open-hole CFRP specimens under tensile fatigue loading. In this study, health state assessments and RUL prognostic is achieved based on a generalized homogeneous hidden semi-Markov approach, suggesting that other types of SHM data can be integrated into the proposed methodology as well. In the study of Galanopoulos G. et al. [43] strain-based health indicators are obtained via FBGs, and RUL is predicted for CFRP single-stiffened panels using Gaussian Process Regression. In the presented RUL prognostic methodologies, models are trained via HIs obtained from SHM data, targeting the RUL, while the direct and interpretable correlation of HIs with damage states of the structure is not clear. However, integrating damage characterization, particularly in terms of severity, and establishing its correlation with RUL prediction outcomes could significantly improve the reliability and interpretability of prognostics. This enhancement is crucial for informed decision-making in maintenance strategies, ensuring more effective and reliable structural health management [44].

To achieve this, active sensing-based SHM techniques provide a promising solution by enabling progressive data collection and real-time damage tracking, forming a crucial foundation for assessing structural integrity over time. Given the challenges associated with delamination growth under fatigue loading, GW-based monitoring offers a promising solution by providing continuous assessment of delamination severity as it evolves over the structure's service life. By capturing progressive damage accumulation, GW methods can enhance the reliability and accuracy of RUL predictions, making them representative of the structural degradation process. Additionally, EMI techniques offer a complementary approach that can enhance GW-based monitoring, particularly in localized damage assessment and high-frequency response analysis. While the next section will focus on GW-SHM and its role in damage diagnostics and RUL prediction, EMI based damage characterization and prognostics will be explored later, highlighting their potential to further refine structural health assessments and strengthen the link between damage states and RUL estimations.

### **Guided Wave Structural Health Monitoring (GW-SHM)**

GW-SHM is a rapidly advancing area in aerospace engineering due to its exceptional capability for damage diagnostics and its potential to contribute to RUL prognostics [45]. GWs or lamb waves refer to ultrasonic waves that propagate along the surface or through the thickness of a structure, making them highly effective for inspecting large areas from a limited number of sensor locations [46]. This characteristic makes GW-SHM an ideal choice for monitoring the structural integrity of complex aerospace components such as aircraft wings, fuselage sections, and other composite parts.

The presence and progression of damage can potentially be monitored through changes in the behavior of GWs, such as variations in wave velocity, attenuation, or mode conversion. These changes may indicate the location, presence, and severity of the damage. In this context, in earlier studies, GWs have been

investigated intensively for metallic structures in aerospace, and they demonstrated their strong capability in detecting, localizing, and sizing the structural damages under various loading conditions owing to GWs strong capability in interrogation of the structure. However, unlike metallic structures, the anisotropic nature of composite structures induces complicated interaction, which makes it challenging to analyze damage effects in the GW signal. Moreover, in the case of delamination, it occurs and grows in different sizes and shapes through the composite's layers, making it even more difficult to correlate the GW signals with the damage [47], [48], [49]. Considering the mode conversion characteristics of GW signals, progressive damage leads to alterations in the material properties throughout the fatigue life, introducing complexities in accurately modeling the frequency-dependent behavior of GWs at different structural states. These evolving material changes affect wave propagation dynamics, making it challenging to establish precise simulations that account for the continuous variation in wave dispersion, attenuation, and mode interactions as damage progresses [50], [51].

As previously mentioned, in a data-driven methodology, prognosis can be achieved via direct methodology, in which machine learning and statistical learning techniques are involved, or through feature extraction via signal processing and/or machine learning. Each technique may overcome specific challenges in converting GW signals to meaningful DIs. Nevertheless, the main disadvantage of machine learning techniques may be put forward in the sense that they require accurate labels to achieve the learning aspect for regression objectives despite their strong capability to handle large data. In that regard, signal processing techniques are well-adapted methods in the literature to extract damage-related information from GWs by representing them in the time-domain, frequency-domain, and time-frequency domain, independent of the target information's assignment [52], [53]. There is some well-adapted signal processing techniques enable to analyze GW signals to convert them to prognostic features. Hilbert Transform (HT) is one of the techniques that estimate the envelope of the signal through the analytical representation of the signal allows feature extraction in time-domain. Yue et al. [22] evaluate the correlation of HIs of GW signals with the global stiffness degradation of the stiffened structure, which is impacted and subjected to C-C fatigue. A mode conversion analysis has been adapted for S0 mode of GW signals via statistical methods to obtain GW-HIs, and the results demonstrate their potential in terms of their prognostic performance metrics scores. Another approach is that as GWs are non-stationary and time-varying signals, it is convenient to represent them through time–frequency analysis [54]. Short-time Fourier Transform (STFT) and Continuous Wavelet Transform (CWT) are some of the widely used methods in the literature and CWT is employed mainly for GWs as it allows for capturing localized features in the signal, making it suitable for analyzing signals with abrupt changes or transient events [55], [56], [57]. Larrosa et al. [58] conducted the study to demonstrate the capability of GW-DIs obtained via STFT analysis concentrating on A0 mode in classifying damage types via Gaussian discriminant analysis for CFRP coupons subjected to tensile fatigue loading. Efforts to monitor the growth of delamination have been undertaken in study of Liu et al. [59] employing GW-DIs with the implementation of the experimental study developed in [60] and correlation between delamination severity and GW-DIs is examined.

The effectiveness of GWs has been demonstrated for data-driven delamination detection, localization, and severity analysis in composite structures, with potential extension toward data-driven RUL prognosis. Given the fact that data-driven RUL prognostic models in the existing literature have infrequently utilized GW-SHM data as input, extensive research has been conducted on diagnostics with GWs. Considering the effectiveness of GW-DIs in damage characterization, incorporating these indicators into RUL prognostics offers considerable potential to enhance the precision and dependability of the predictions [61].

Despite their proven advantages in damage diagnostics, GWs face certain limitations. A major challenge is their susceptibility to environmental factors such as temperature fluctuations, humidity, and external vibrations, which can introduce noise into the signal, leading to possible errors in the analysis [62], [63]. Furthermore, despite the application of advanced processing techniques, the variability in fiber orientations, the presence of multiple composite layers, and the intricacy of damage mechanisms can still complicate the

analysis of GW signals, potentially affecting the accuracy of GW-SHM systems. Considering RUL prognostics with GWs, research gaps can be identified, as despite the demonstrated effectiveness of GW-DIs in damage diagnostics, their direct incorporation into RUL prognostic models remains limited in the literature. The anisotropic nature of composite structures, combined with the unpredictable growth of delaminations in varying shapes and sizes across multiple layers, complicates the establishment of a clear and quantifiable correlation between GW signals and progressive structural degradation. The inherent variability in damage evolution under fatigue loading presents a significant challenge in developing generalizable prognostic models based on GW data. Therefore, further research is needed to develop techniques for extracting reliable DIs from GW signals and to achieve robust RUL prognostic models capable of accurately capturing degradation trends. Moreover, a comparative and complementary study is needed to enhance the reliability of GW-based diagnostic and prognostic methodologies for that reason, the EMI technique will be investigated as a complementary approach to GW-based monitoring addressing the gap in the literature regarding the integration of multiple SHM techniques for both damage assessment and RUL prediction.

Moving forward, EMI-SHM will be explored in the next section, discussing its unique advantages and applications in SHM. This approach will ensure a holistic understanding of the potential for integrating various SHM methods to enhance overall system reliability and effectiveness in diagnosis and prognosis.

### **Electromechanical Impedance Structural Health Monitoring (EMI-SHM)**

A promising approach to enhancing the effectiveness of existing SHM methods lies integrating complementary techniques. By combining multiple SHM methods, the limitations inherent in one technique can be compensated for by the strengths of another, resulting in a more robust and reliable system for prognosis. This integrated approach improves the accuracy of structural assessments and enhances the reliability of RUL predictions, offering a more comprehensive solution for maintaining the integrity of critical structures [64], [65]. In this context, the EMI technique is applied in this study to complement the GW-SHM method. EMI technique is another active sensing technique that utilizes PZT transducers to measure the electrical impedance of a structure, which changes in response to damage. EMI provides high sensitivity to local damage, may allow for the early detection of small defects and micro-cracks [66]. EMI techniques also have the advantage of being less affected by the anisotropic properties of composite materials, which in fact complicate GW analysis. Additionally, EMI systems often require simpler hardware setups and can operate periodically which makes them a cost-effective and efficient solution for health monitoring in various aerospace and industrial applications [67].

EMI is a concept in the field of SHM involves the use of PZTs, which generate mechanical vibrations when subjected to an electrical signal, and can be used to monitor the structural integrity. In the context of SHM, these sensors can be bonded to the surface of the structure, and they emit high-frequency mechanical waves. The interaction between these waves and the structural elements results in impedance, a complex function of the mechanical properties of the material [68]. By analyzing the changes in the impedance signature, one can detect the presence of damage, such as cracks and delamination [32], [69]. This technique is susceptible to minor variations in structural properties, making it an effective method for diagnosis and prognosis. By comparing baseline impedance measurements with those taken over time, one can identify the onset and progression of damage. This real-time monitoring capability makes EMI a powerful tool for enhancing the safety and reliability of composite structures in various engineering applications.

DI extraction methods for EMI techniques are crucial for effectively identifying and quantifying structural damage. These methods typically involve analyzing changes in the impedance signature. The DIs are extracted by comparing the current impedance response with a baseline measurement, which is taken when the structure is known to be in a healthy state. Several methods can be used to extract these indicators, including root mean square deviation (RMSD), mean absolute percentage deviation, correlation coefficient

deviation, and cross-correlation analysis. These statistical DI extraction methods are commonly adapted for the EMI technique to assess structural integrity.

EMI is a highly localized damage detection method primarily utilized for pinpointing and assessing damage in specific areas of a structure. In this context, L. Yu et al. [70] study that the EMI method has shown sensitivity in damage detection and classification in composites using statistical damage indicators from experimental and simulation analysis. Delamination detection via the EMI method by combining experimental and simulated data to show the method's sensitivity to some parameters, such as the size and position of the delamination and the sensor investigated by Singh S. et al. [71] and Gresil M. et al. [72]. The results show that as the delaminated region is closer to the PZT, the deviation in the EMI spectrum is more significant.

GW and EMI techniques have independently demonstrated strong capabilities in SHM, yet their combined implementation remains largely unexplored, especially in the context of RUL prognostics. Despite their individual advantages, EMI's susceptibility to variations in local conditions and GW's sensitivity to material anisotropy and complex wave propagation behavior in composites pose challenges in accurately correlating diagnostic indicators with long-term structural degradation. To address these limitations, a hybrid SHM approach leveraging both GW and EMI could improve damage characterization and enhance the interpretability and accuracy of RUL predictions. Implementing GW-SHM and EMI-SHM together can provide a more comprehensive understanding of structural damage, integrating localized precision with expansive coverage to capture the full extent of degradation in composite structures. This dual approach can enhance the detection and analysis of structural health issues, offering a multi-faceted perspective essential for accurate diagnostics and prognostics, and by combining data-driven methodologies with advanced feature extraction techniques for DIs, a more robust and reliable SHM framework can be developed to improve long-term safety and maintenance strategies for aerospace and other critical structural applications.

EMI and GW-based DIs may provide a quantitative representation of damage evolution but require further correlation with actual failure progression. To achieve this, AI-based prognostic models are well-suited to establish data-driven relationships between DIs, damage severity, and RUL estimates, enhancing the accuracy and interpretability of predictions. The subsequent sub-section, "Artificial Intelligence (AI)-based Prognostic," will provide a more in-depth discussion on how AI technologies are leveraged to advance prognostic capabilities in this field.

### **Artificial Intelligence (AI)-based Prognostic**

Beyond traditional techniques, either signal processing or statistical techniques, machine learning methods have become essential in analyzing SHM data [73]. These methods systematize the process of detecting, localizing, and classifying structural damage, thereby enhancing the efficacy of SHM practices. In data-driven methodologies, machine learning methods are widely used which include Artificial Neural Networks (ANNs), Support Vector Machines, Random Forests, k-Nearest Neighbors, and Principal Component Analysis to detect, localize and classify the damage in composite structures [74]. Each of these techniques offers unique advantages for interpreting the complex and large-scale data generated by SHM systems [75], [76]. Deep learning is a subset of machine learning that primarily focuses on using ANNs as Deep Neural Networks (DNNs) with multiple layers to learn complex patterns and representations from data [77]. While traditional ANNs typically consist of a single hidden layer or a limited number of layers, DNN architectures employ deeper networks, meaning they have many layers, each capable of capturing increasingly abstract features. This depth enables deep learning models to automatically learn and extract features from raw input data, making them highly effective for GW analysis in composite structures [78], [79].

RUL prediction is inherently a non-linear regression task, and DNNs demonstrate significant potential in handling the complex patterns and non-linear relationships involved in such predictions [80], [81]. DNN models such as Convolutional Neural Networks (CNNs) and Recurrent Neural Networks further enhance the ability of ANNs to handle different types of data and extract relevant features without manual intervention. CNNs, with their ability to recognize spatial hierarchies, are particularly effective in analyzing GW signals when represented as images (e.g., time-frequency spectrograms) [82]. They automatically learn spatial features and patterns associated with different types of structural health conditions. CNN models have been previously explored for damage detection and sizing in the literature, as detailed in sources [76], [83]. In addition to their classification and regression capabilities, DNN models may involve multiple DL architectures and are trained to extract features that can further input the prognostic models. Moradi et al. [84] investigate HIs that serve as inputs for advanced predictive models, showing the capability of the CNN model as a base learner incorporating GW signals.

Beyond the capabilities highlighted earlier, DNN models offer significant adaptability for advanced fusion methodologies [85]. These models are particularly effective in synthesizing multilevel features gathered from extensive sensor networks or a combination of different SHM techniques. By leveraging such integrative approaches, DNN models can enhance the robustness and accuracy of predictive analytics, accommodating the complexity and variability inherent in real-world data. This ability to integrate diverse data sources and extract meaningful insights is crucial for developing more comprehensive and effective SHM systems that can predict and mitigate potential failures in complex engineering structures [86]. Broer et al. [87] show in their research that fusing two SHM techniques, AE and FBGs, may improve the intrinsic capacities of each method, which can be utilized more effectively, leading to synergistic effects that enhance damage diagnostics. In another study, Moradi et al. [88] suggest that fusing various AE features with semi-supervised learning techniques makes it possible to effectively use labelled and unlabeled data to develop reliable HIs that can be further utilized in RUL prognostics.

Despite advancements in DL-based prognostics, a critical research gap remains in developing RUL prediction frameworks for composite structures that directly and interpretably connect to the structural diagnostic state, capturing the realistic progression of damage. While DNNs exhibit strong predictive capabilities, their inherent black-box nature limits the interpretability of damage evolution, making it challenging to establish a direct correlation between structural degradation and RUL estimations. To ensure meaningful and reliable predictions, it is crucial to bridge this gap by enhancing the correlation between extracted features from SHM data and damage severity, acknowledging that a direct link to the underlying physical damage state remains challenging due to the inherent limitations of individual monitoring techniques. Addressing this limitation necessitates the development of approaches that integrate data-driven models with multi-level information integration, enabling more explainable and physically consistent RUL prognostics for composite structures.

### 1.3 Conclusion

In conclusion, following the literature review, the key research gaps can be explained as follows:

- The complexity of delamination evolution and its unpredictable propagation under compressive fatigue conditions pose significant challenges. Current methodologies lack a robust approach for accurately quantifying delamination severity and linking it to RUL predictions. Further research is needed to characterize delamination severity and integrate it into a comprehensive prognostic framework to improve interpretability and reliability in RUL estimations.
- To improve long-term safety and maintenance strategies for aerospace and other critical applications, there is a need to integrate data-driven methodologies with advanced feature extraction techniques to enhance RUL prognostics. This includes optimizing signal processing

techniques for GW signals, improving hybrid diagnostic models, and developing machine learning frameworks that can adapt to evolving structural degradation. A sophisticated SHM system combining AI-driven prognostics and multi-modal sensing techniques is necessary to advance RUL predictions' accuracy, interpretability, and applicability.

- Despite the proven advantages of GW for damage diagnostics, the integration of multiple SHM techniques remains an area requiring further exploration. There is a gap in the literature regarding the systematic integration of GW and EMI techniques for damage characterization and RUL prediction. A comparative and complementary study is needed to investigate these methods to improve the accuracy and reliability of prognostics methodologies.

Therefore, this research aims to develop and evaluate frameworks for monitoring damage progression and predicting the RUL as the time corresponding to a certain damage state of composite structures. In light of the identified gaps, the following section will elaborate on the novel contributions of this thesis, discussing in detail how these advanced methodologies enhance understanding of damage mechanisms and RUL prognosis by integrating AI capabilities into SHM systems. This integration represents a substantial advancement in the field of SHM, extending the frontiers of predictive accuracy and operational efficiency within critical aerospace applications. To achieve these advancements, several research questions must be addressed:

- How can advanced active-sensing techniques improve the assessment of damage severity in composite structures while addressing the challenges posed by material anisotropy and complex failure mechanisms?
- How can the severity of delamination be effectively integrated into data-driven RUL prognostic models for composite structures?
- What methodologies can be applied to improve the accuracy and generalization of RUL prognostics for impacted composite aerospace structures?

By answering these questions, this research will contribute to the development of more accurate and reliable RUL prognostic models, enhancing the safety and operational efficiency of composite structures in aerospace applications.

## 1.4 Contributions

Although various studies have proposed RUL prognostics for composite structures, more research should address the delamination propagation and its correlation with RUL using SHM data in a data-driven methodology. Additionally, while data-driven RUL prognostic models in the existing literature have infrequently utilized GW-SHM data as input in data-driven methods, extensive research has been conducted on diagnostics with GWs. Besides, EMI-based SHM has achieved significant interest in detecting local structural changes; even so, in-situ monitoring of composites in the sense of delamination propagation has limited application from an EMI-based SHM point of view. Moreover, most of these studies mainly focus on structural degradation under tensile fatigue conditions, which presents an area for further investigation to enhance RUL prognostics' predictive accuracy and applicability in impacted composite structures under varied compressive scenarios. Therefore, this research focuses on improving RUL prognosis by gaining a deeper understanding of impact-induced delamination under compressive loading conditions via the investigation of two active-sensing-based SHM applications: GW-SHM and EMI-SHM. Considering the outlined research gaps and the subsequent questions, the following studies are conducted to enhance understanding and address the identified challenges:

1. Monitoring of impact-induced progressive delamination under compressive in-plane fatigue conditions using two active sensing-based SHM techniques: GW and EMI.
2. Exploring the fusion capabilities of GW and EMI for improved RUL prognosis.

3. Data-driven diagnosis of delamination and its correlation with RUL prognosis.
4. Investigation of AI-based RUL prognostic methodologies leveraging diverse levels of GW-SHM features.

### **I. Monitoring of impact-induced progressive delamination under compressive in-plane fatigue conditions using two active sensing-based SHM techniques: GW and EMI.**

Considering that impact-induced delamination is a critical damage type that requires detailed inspections to maintain the reliable operation of the aircraft in this research two active sensing methods are adapted as SHM to monitor progressive delamination under C-C fatigue loading conditions. An integrated approach is applied in this study by adding the EMI technique to enhance the understanding and reveal an improved demonstration of damage propagation in composites, in addition to GW-SHM. Furthermore, as the correlation between delamination and GW and EMI signals requires careful analysis, advanced processing techniques are applied to extract features as DIs that are aimed to be sensitive to delamination.

In the context of GWs, GWs have frequency dependency, and their constitutional modes can be induced via frequency tuning. Most research in the literature discussed previously concentrates on mode analysis and conducts the processing techniques based on specific GW modes when it comes to applying signal processing techniques. Nevertheless, discovering GW modes that are purely sensitive to delamination is challenging, especially for complex structures such as woven composites. Moreover, as delamination happens in various shapes in composite layers, and it propagates stochastically under the fatigue conditions, this creates varied mechanical parameters at each layer and may challenge the determination of certain dispersion characteristics of GWs. Besides, mode separation can be a complex task when the propagation path presents a limited range between the boundaries and the damage, which may induce many reflections and overlapped signals, besides possible higher mode excitation, which may also be sensitive to variations in the damage area. Thus, GW-DIs are derived through signal processing using a mode-independent approach aiming at the delamination-sensitive portion of the GW signal.

Considering EMI-SHM capability detecting local structural changes a comparative analyze is conducted to monitor delamination propagation under C-C fatigue from the EMI-SHM and GW-SHM perspective. Within the methodology of this work, while SHM has been implemented through GWs and EMI, ultrasonic C-scan inspections are performed to label the severity of the damage during the fatigue life of each sample. Ultrasonic pulse-echo c-scan technique has been chosen in this work to label the damage state of samples because of its ability to provide through-depth information and its applicability to inspecting the samples while they are in the fixture and still under testing. C-C fatigue is achieved by targeting the characterization of the delamination progression and its contribution to end-of-life events. DIs are obtained from GW and EMI data from each tested sample based on advanced signal processing and statistical techniques to introduce and discuss the coherence between the SHM data and labelled delamination states measured via the C-scan method as a non-destructive technique.

### **II. Exploring the fusion capabilities of GW and EMI for improved RUL prognosis.**

This study proposes a novel framework for RUL prognostics for composite structures by integrating EMI and GW-based SHM methods into the prognostic methodology. The effectiveness of GWs and EMI-based RUL prognostics has been investigated by DIs used as input in a DNN model to predict RUL as output. DNN models excel in leveraging advanced fusion techniques, making them highly effective at integrating and synthesizing multi-level features from diverse SHM methods.

Thus, the novelty of this work lies in the fusion of GW and EMI techniques for the prediction of RUL, which is integrated into a comprehensive prognostic framework. Features derived from GW and EMI measurements were first analyzed for their correlation with measured delamination growth and then used as inputs for prognostic models developed using DNNs. This approach significantly enhances the accuracy

and reliability of RUL predictions as the proposed GW-EMI fusion models aim to harness the most effective predictions from each DI. The results demonstrated that while GW-DIs provide higher accuracy than EMI-DIs, proposed fusion methodologies offer significant advantages with promising capability and greater stability in enhancing the reliability of RUL predictions with lower error through the cycles of all samples. Utilizing these comprehensive integration strategies, DNNs significantly improve the precision of RUL prognosis, adeptly handling the complexities and variabilities typical of real-world data scenarios.

### **III. Data-driven diagnosis of delamination and its correlation with RUL prognosis.**

This study proposes a novel GW-SHM-based integrated prognostic approach that targets RUL and delamination size in a data-driven framework. In this study, delamination initiated by a low-velocity impact is considered the dominant damage mechanism that leads to the final failure of the samples. The prognostic concept aims to improve the learned representations' interpretability by targeting RUL and delamination size as separate outputs in the learning framework. A DNN model is implemented in this work as the prognostic model. Model architecture and hyperparameters are adapted and tuned according to the input and output sets, focusing on two objectives. The first is to investigate the contribution of various paths to the prognosis of RUL and delamination size in each sample domain. The second objective is to achieve a more generic prognostic model with ensembled GW-DIs from different samples arranged as the DNN model's input set. The proposed methodology enables monitoring the contributing damage mechanisms to the failure of the structure that results in a reliable and effective RUL prognosis.

### **IV. Investigation of deep learning-based RUL prognostic methodologies leveraging diverse levels of GW-features.**

Deep learning techniques such as CNNs offer substantial advantages in analyzing GW signals, particularly for SHM. CNNs excel in pattern recognition within complex signal data, making them ideal for identifying characteristic features of damage from GW recordings. Building on these strengths, as previously discussed, RUL prognostics can be implemented either directly or through feature-based methods. In this research, a novel data-driven prognostic framework is introduced. It includes two levels of prediction: a direct RUL prediction using a CNN as the base learner and a two-level fusion methodology that employs DIs through a DNN. This dual-layered framework effectively combines the strengths of direct and feature-based prognostics. By integrating CNNs for direct predictions and DNNs for feature integration, the framework enhances the predictive accuracy and reliability of the system, offering a robust solution for the proactive maintenance of critical structures.

## **1.5 Thesis Outline**

The thesis begins with an Introduction that sets the stage for the research topic, focusing on RUL prognostics and its critical role in ensuring the safety and integrity of structures. The following chapters are organized as follows:

**Chapter 2, Prognostic Methodology**, builds the methodology for achieving prognosis based on the utilized sensing methods. The theoretical background of the elements of active-sensing techniques in terms of PZT sensor technology, GW-SHM, and EMI-SHM is introduced. The DNN models designed to map GW and EMI data to target sets as regression learners in the prognostic frameworks in each approach are given together with the structural organization of target sets used to train predictive models.

**Chapter 3, Investigation of Delamination Growth under Compression After Impact (CAI)**, presents the experimental study on delamination behavior in composite structures subjected to CAI. The section on CAI Test for Woven Composite Structures details the design and setup of the experimental apparatus, emphasizing the design of the CAI experimental setup and the procedures for fatigue testing. These tests simulate real-world conditions, providing valuable data on how delamination progresses under compressive

stress. Implementation of active sensing techniques in CAI testing presents the integration of GW-SHM and EMI-SHM techniques into compressive fatigue testing. The data collection framework and the placement of sensors on the test samples will be detailed, with dedicated subsections for the specific application parameters of both the EMI and GW methods, discussing their implementation in the experimental setup.

**Chapter 4, Progressive Delamination Characterization via GWs & EMIs** is organized to present the study of impact-induced damage propagation in woven composite structures subjected to C-C fatigue loading, utilizing GW and EMI to characterize and monitor delamination progression. The chapter focuses on the feature extraction process for EMI and GW to obtain high-level DIs. Prognostic metrics for achieved DIs are presented and discussed.

**Chapter 5, RUL Prognosis via Integration of Active Sensing SHM Methods: EMI & GW**, focuses on integrating EMI and GW methods to improve RUL predictions employing a DNN model. It discusses the techniques used to merge data from different sensing methods, aiming to enhance the robustness and accuracy of RUL predictions.

**Chapter 6, Prognosis of RUL with Delamination Growth via GW-SHM**, a GW-SHM-based integrated prognostic approach that targets RUL and delamination size in a data-driven framework, is investigated in this study. This approach aims to enhance the learned representations' interpretability by treating RUL and delamination size as separate outputs in the model.

**Chapter 7, Prognosis of Delamination Induced Failure Blending Deep Learning with Signal Processing**, introduces a novel data-driven prognostic framework aimed at predicting the RUL. The framework employs a base learner level and a two-level fusion methodology, combining direct and feature-based prognostics for enhanced predictive accuracy.

**Chapter 8, Conclusion & Future Research**, provides a comprehensive summary of the research, reiterating the key findings and contributions of the thesis. Finally, suggestions for future work outline potential areas for further investigation, based on the limitations identified and the new questions raised by the study. This chapter aims to inspire continued research and development in the field of SHM and AI-based damage and RUL prognosis.



## **2 Methodological Framework**

## 2.1 Introduction

In this chapter, the general prognostic methodology developed in this thesis is presented along with the background of its key components. Figure 2.1 illustrates the frameworks investigated in this study. Experimental test procedures have been designed to monitor the progressive growth of delamination while systematically collecting SHM data; GW and EMI signals, complemented by ultrasonic C-scan inspections. The methodological elements cover the C-C fatigue testing procedures, including specified loading conditions and delamination monitoring techniques. Subsequently, the operational principles of PZT, the fundamentals of GW and EMI are presented to provide a deeper understanding of damage interaction within the signal. In the following third sub-section, the approach to organize the target sets based on the CAI testing dataset are briefly discussed to offer a comprehensive understanding of the overall framework. As the models are developed to predict RUL and damage severity using a regression approach, the target sets are designed to effectively train the prognostic models for RUL and damage severity. For each approach, the samples used in the prognostic methodology will vary based on the specific load scenarios being investigated. To map the GW and EMI information to the target vectors, DNN-based regressors are designed for each specific input set, tailored for distinct purposes. These DNN regressors are detailed in the final subsection, where their structures and underlying principles are explained to provide a clear understanding of their design and functionality.

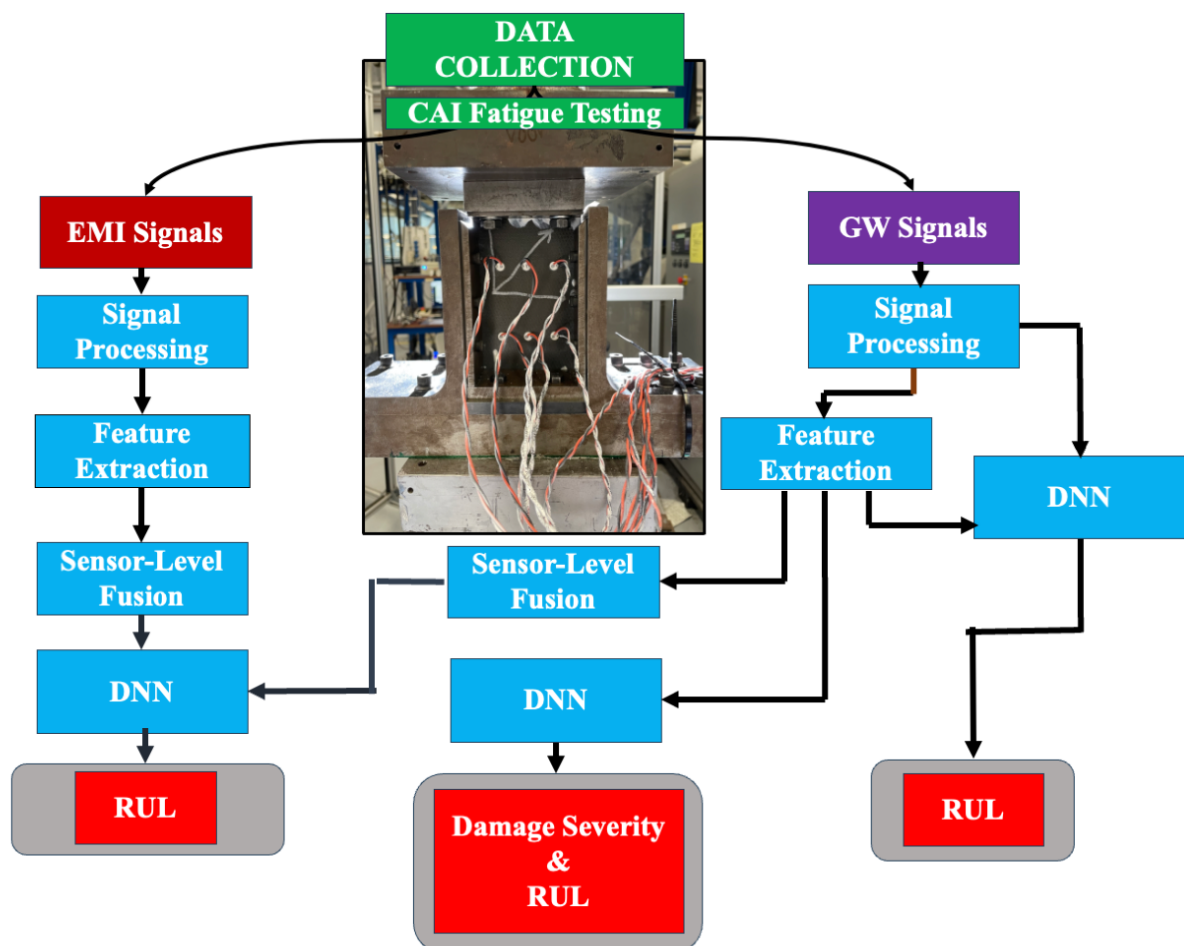


Figure 2.1. Methodological frameworks investigated in this thesis and their key components.

## 2.2 Background of Methodological Components

### 2.2.1 C-C Fatigue Testing

ASTM D7137 is designed to measure the residual compressive strength of composite materials after they have sustained impact damage. The test specimens are rectangular plates made from fiber-reinforced polymer matrix composites (e.g., carbon fiber, glass fiber composites). The dimensions of are proposed to be length of 100-150 mm, width of 100-125 mm, and thickness typically around 4-6 mm, depending on the material [89]. The composite specimen is first subjected to a low-velocity impact using a controlled drop-weight or pendulum mechanism. The impact induces an impact damage in the form of delamination combined with matrix cracks and fiber breakages without penetrating the material completely. Post-impact, the specimen are inspected to quantify the size of the damage area using methods like ultrasonic immersion testing or pulse-echo c-scan to verify damage severity and localization.

The damaged composite sample are placed in a compression test fixture, shown in **Figure 2.2**, where compressive load is applied perpendicular to the plane of the damage. The test setup must ensure that global buckling is prevented during compression testing with an anti-buckling fixture, holding the specimen without constraining it excessively. The end fixtures grip the specimen while allowing it to be loaded in compression. Careful alignment of the specimen is essential to prevent introducing unintended bending stresses. The failure modes in composite structures during compression testing after impact can vary and may occur in combination, including:

- Delamination buckling: A separation between layers of the composite, which reduces load-carrying capacity and leads to failure.
- Shear failure: Often occurs along the matrix or at the fiber/matrix interface due to the stress concentration around the damaged area.
- Fiber breakage: Under compressive loads, fibers may bend or break, leading to structural collapse.

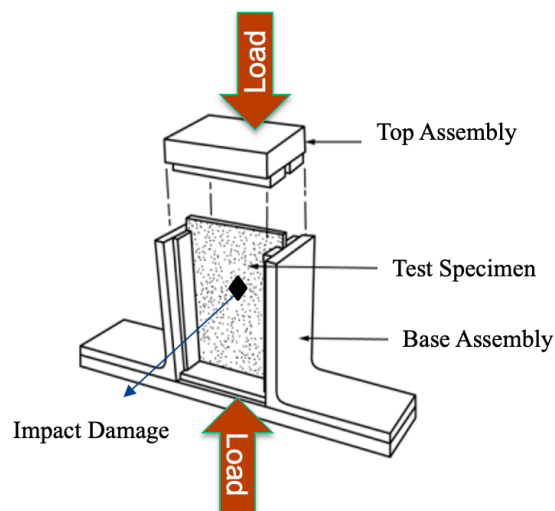


Figure 2.2. Standard anti-buckling test fixture for ASTM D7137/D7137M [89].

### 2.2.2 Piezoelectric (PZT) Transducers

During the compression experiment, the PZT sensors continuously monitor the structural health of the composite by detecting changes in wave propagation caused by internal damage. **Figure 2.3** represents the PZT network installed on a specimen that allows exciting and receiving signals for EMI and GW measurements.

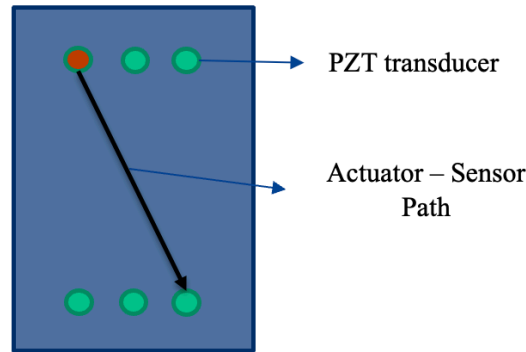


Figure 2.3. PZT sensor surface-attached on testing sample.

PZT transducers are piezoelectric materials employed with the principle of transforming electrical energy into mechanical energy and vice versa owing to the piezoelectric effect [90]. The shape of a PZT transducer plays an important role in activating and receiving GWs. Several factors influence the interaction between the transducers and the GWs in the structure: length of the transducer, excitation frequency, wavelength of the GW, thickness of the bonding [91]. In **Figure 2.4**, rectangular and circular shaped PZT transducers are shown. Their characteristic behaviors can be given as:

- A rectangular PZT actuator produces GWs with energy dominant in the direction perpendicular to its long length, showing strong directionality of wave generation.
- A circular PZT actuator generates a uniform and omnidirectional GW-field.

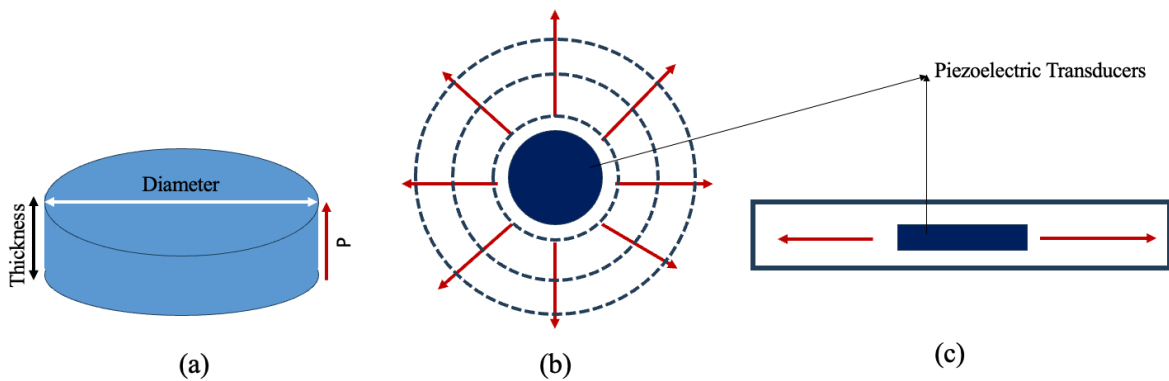


Figure 2.4. Presentation of (a) disk shaped PZT with geometrical parameters (b) circular and rectangular PZT with wave-field direction [90]

An optimal criterion for selecting the dimensions of a PZT element for wave actuator is:

$$Diameter_{\text{actuator}} = \frac{v_{\text{wave}}}{f} \left( n + \frac{1}{2} \right) = \lambda_{\text{wave}} \left( n + \frac{1}{2} \right), \quad n = 0, 1, 2, \dots \quad (2-1)$$

where  $Diameter_{actuator}$  is the diameter of the PZT,  $P$  is the polarization direction,  $V_{wave}$  is the wave velocity,  $\lambda_{wave}$  is the wavelength and  $f$  is the frequency. Ideally, GW frequency/wavelength tuning can be adjusted via the parameters of the PZT actuator.

### 2.2.3 Electromechanical Impedance (EMI) Technique

Impedance,  $Z$ , is a complex, frequency-dependent quantity representing the opposition a circuit presents to alternating current, characterized by both resistive and reactive components. Admittance,  $Y$ , is the inverse of impedance, and it is given by;

$$Y(\omega) = \frac{1}{Z(\omega)} \quad (2-2)$$

conversely, quantifies the ease with which current flows through the circuit, reflecting its conductive and susceptive properties. When damage occurs, the characteristic vibrational behavior of the structure changes, and these variations in vibration can be detected by measuring changes in complex electrical admittance. This measurement is possible due to the coupling between the PZT transducer and the host structure, which allows for the monitoring of structural health through the transducer's response to vibrational shifts. The complex electrical admittance expression is given in following equations for the electromechanical admittance and the mechanical impedance of the PZT patch:

$$Y(\omega) = j\omega \frac{w_p l_p}{h_p} \left[ \frac{Z_p(\omega)}{Z_p(\omega) + Z_S(\omega)} \frac{d_{31}^2 \bar{Y}_{11}^E \tan(\kappa l_p)}{\kappa l_p} + \bar{\epsilon}_{33}^T - d_{31}^2 \bar{Y}_{11}^E \right] \quad (2-3)$$

$$Z_p = \frac{\kappa w_p h_p \bar{Y}_{11}^E}{(j\omega) \tan(\kappa l_p)} \quad (2-4)$$

where  $Z_p$  and  $Z_S$  are the mechanical impedance of the PZT patch and the structure, respectively.  $Z_p$  is derived where  $\omega$  is the angular frequency of the excitation voltage,  $j$  is the imaginary number, and  $w_p, l_p$ , and  $h_p$  are the width, length, and thickness of the PZT patch, respectively.  $\bar{Y}_{11}^E$  is the complex Young's modulus,  $\bar{\epsilon}_{33}^T$  is the complex electric permittivity,  $d_{31}$  is the piezoelectric strain coefficient, and  $\kappa$  is the wave number [92].

### 2.2.4 Guided Wave (GW) Technique

GWs are a type of elastic wave that propagates in plate-like structures consisting of longitudinal and shear modes. Their characteristics are determined by the structural geometry, ply fiber direction, initial wave entry angle, and selected excitation signal and frequency [93]. For the free surfaces of the plate given in **Figure 2.5**, fundamental equations are given as following

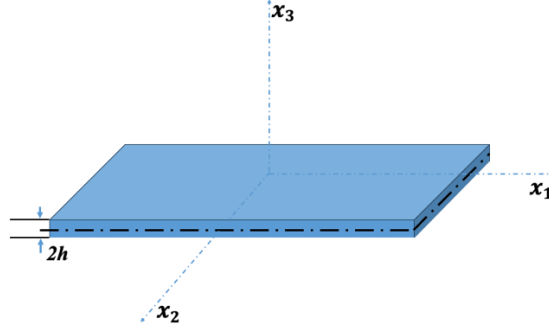


Figure 2.5. Thin plate configuration.

$$\frac{\partial^2 \phi}{\partial x_1^2} + \frac{\partial^2 \phi}{\partial x_3^2} = \frac{1}{c_L^2} \frac{\partial^2 \phi}{\partial t^2} \quad (2-5)$$

$$\frac{\partial^2 \psi}{\partial x_1^2} + \frac{\partial^2 \psi}{\partial x_3^2} = \frac{1}{c_T^2} \frac{\partial^2 \psi}{\partial t^2} \quad (2-6)$$

$$\phi = [A_1 \sin (px_3) + A_2 \cos (px_3)] \cdot \exp [i(kx_1 - \omega t)] \quad (2-7)$$

$$\psi = [B_1 \sin (qx_3) + B_2 \cos (qx_3)] \cdot \exp [i(kx_1 - \omega t)] \quad (2-8)$$

Assuming the component of stress in the  $x_3$  direction at  $x_3 = \pm d/2$  is zero. ( $x_3 = \pm d/2 = \pm h$ ) and no displacement in the  $x_2$  direction and no variation of any physical quantities in the  $x_2$  direction. General description of GWs propagating (Lamb waves) in an isotropic and homogeneous plate:

$$\frac{\tan (qh)}{\tan (ph)} = \frac{4k^2 qp \mu}{(\lambda k^2 + \lambda p^2 + 2\mu p^2)(k^2 - q^2)} \quad (2-9)$$

$$p^2 = \frac{\omega^2}{c_L^2} - k^2, q^2 = \frac{\omega^2}{c_T^2} - k^2, k = \frac{2\pi}{\lambda_{\text{nave}}} \quad (2-10)$$

$$c_L = \sqrt{\frac{E(1-\nu)}{\rho(1+\nu)(1-2\nu)}} = \sqrt{\frac{2\mu(1-\nu)}{\rho(1-2\nu)}} \quad (2-11)$$

$$c_T = \sqrt{\frac{E}{2\rho(1+\nu)}} = \sqrt{\frac{\mu}{\rho}} \quad (2-12)$$

$c_L$  is velocity of longitudinal mode,  $c_T$  is velocity of transverse/shear mode,  $\lambda$  is wavelength,  $\rho$  density of the plate,  $\mu$  shear modulus of the plate and  $E$  is the Young's modulus. GWs are the superposition of longitudinal and transverse/shear modes. GWs in plates exhibit multiple modes of propagation, primarily categorized into symmetric (S) and antisymmetric (A) modes. Each mode has distinct displacement patterns across the plate's thickness, which influence how they interact with defects and boundaries. At low frequencies, only the fundamental modes like  $S_0$  and  $A_0$  are dominant, traveling with minimal dispersion, making them suitable for long-range inspection. As the frequency increases, higher-order modes (e.g.,  $S_1$ ,  $A_1$ ) start propagating, which may exhibit significant dispersion, affecting their velocity and attenuation characteristics. This frequency dependence allows tuning of GW modes to optimize sensitivity for detecting specific types of defects or for inspecting plates of varying thicknesses, mostly applicable for isotropic materials and structures [94]. **Figure 2.6** presents the mode characteristics of GWs in plates.

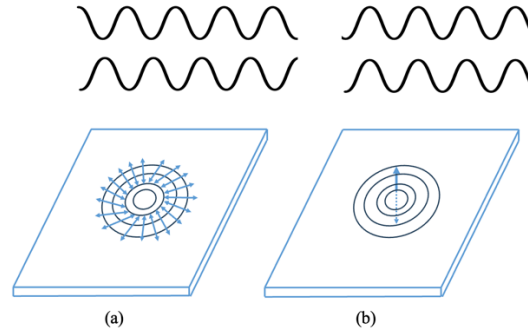


Figure 2.6. (a) Symmetric  $S_0$  and (b) antisymmetric  $A_0$  modes of GWs.

The phase velocity and group velocity can characterize the propagation of GWs  $c_g$ . The propagation speed of wave phases of particular frequency in the overall wave signals is given as in equation 2-13. The velocity with which the overall shape of the wave amplitudes (known as the modulation or envelope of the wave) is the group velocity, and its expression is given in equation 2-14. The group velocity is dependent on frequency  $f$  and plate thickness  $d$ . Group velocity is used for damage location/travel time calculation, and its velocity captured in experiments can be found as equation 2-15.

$$c_p = \frac{w}{2\pi} \lambda_{\text{wave}} \quad (2-13)$$

$$c_g(f, d) = dw \left[ d \left( \frac{w}{c_p} \right) \right]^{-1} = c_p^2 \left[ c_p - (f \cdot d) \frac{dc_p}{d(f \cdot d)} \right]^{-1} \quad (2-14)$$

$$f = \frac{w}{2\pi} \quad (2-15)$$

### 2.3 Determining EoL

The prognostic problem investigated in this thesis is a regression task, as it involves predicting continuous variables, RUL, and delamination length, based on extracted features from GW and EMI signals. RUL refers to the expected time or number of operational cycles in which the structure can safely continue functioning. RUL estimation considers the degradation rate and the structure's ability to withstand further loading under operational conditions before reaching a critical threshold level. This concept is illustrated in **Figure 2.7**, highlighting the relationship between delamination growth and the RUL determination strategy. Degradation is characterized by the growth of delamination length,  $RUL_{\text{threshold}}$  representing the point at which the degradation accelerates.  $c$  represents the time interval between the threshold point and the final failure. The final predicted time of the RUL model corresponds to the moment when this quantified maximum delamination length is achieved, rather than the complete structural failure. Therefore, the final prediction of the RUL model incorporates the  $c$  interval, which represents the time that the structure reaches a specific delamination length that defines its final delamination state. This delamination length is expected to vary across tested samples due to differences in loading conditions and initial damage characteristics.

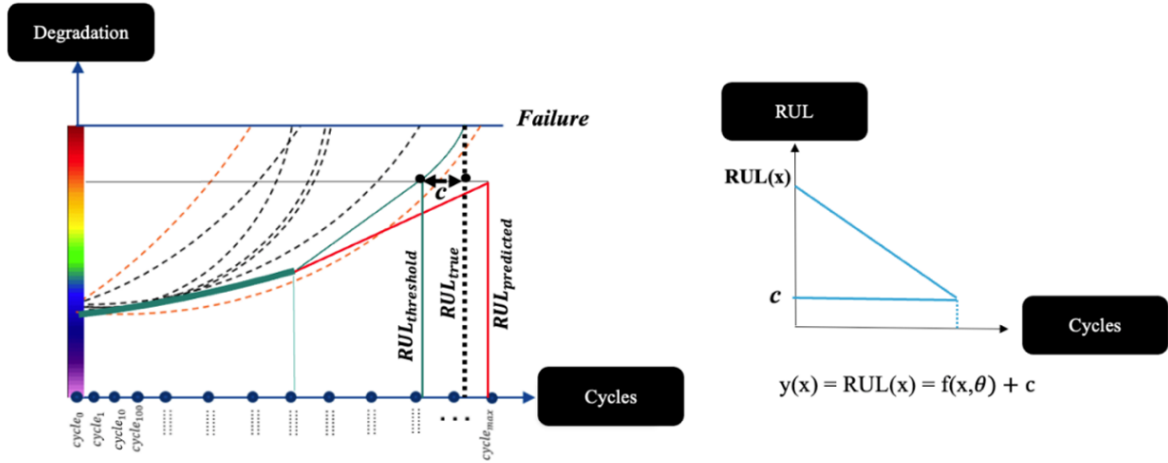


Figure 2.7. Structural degradation through delamination damage and RUL relation.

Due to the complex nature of damage evolution in composite structures, the relation between input features and target variables is typically nonlinear, influenced by factors such as anisotropic material behavior, stress redistribution, and frequency-dependent signal propagation. The input set consists of features derived from signal processing of the GW and EMI signals. The goal is to map each cycle step,  $t$ , which progresses from 1 to the final cycle step (a different value for each sample due to varying EoL spans), to the corresponding target information. The target set includes two primary vectors for each sample: one representing delamination length and the other representing RUL both for threshold level. The input sets consist of two- and three-dimensional data, and their organization, which varies across the studied frameworks, is detailed in the corresponding chapters. **Table 2.1** presents the one dimensional target vectors for the samples in the data set for RUL,  $y_R^{N_s t}$ , and delamination length,  $y_d^{N_s t}$  where  $N_s$  is number of tested sample and  $t$  is the data collection step during cycling loading. In this methodology, each predicted RUL value will be correlated to certain damage severity level.

Table 2-1. Target sets as delamination length and RUL.

#No of Tested Sample	Delamination Length	RUL
1	$[y_d^{11} \ y_d^{12} \ \dots \ y_d^{1t}]$	$[y_R^{11} \ y_R^{12} \ \dots \ y_R^{1t}]$
2	$[y_d^{21} \ y_d^{22} \ \dots \ y_d^{2t}]$	$[y_R^{21} \ y_R^{22} \ \dots \ y_R^{2t}]$
3	$[y_d^{31} \ y_d^{32} \ \dots \ y_d^{3t}]$	$[y_R^{31} \ y_R^{32} \ \dots \ y_R^{3t}]$
...	.	.
...	.	.
$N_s$	$[y_d^{N_s 1} \ y_d^{N_s 2} \ \dots \ y_d^{N_s t}]$	$[y_R^{N_s 1} \ y_R^{N_s 2} \ \dots \ y_R^{N_s t}]$

## 2.4 Signal Processing Techniques

In SHM, particularly for GWs, the selection and application of appropriate signal processing methods are essential for accurate damage characterization and feature extraction. Due to the anisotropic medium of composite materials frequency dependent GW signals result in signal that processing via traditional time or frequency domain analyses may not sufficiently capture the subtle features associated with damage

progression. To address these challenges, this study employs time–frequency domain techniques, namely the Hilbert Transform (HT) and Wavelet Transform (WT) to extract damage-sensitive features from raw sensing data.

#### 2.4.1 Hilbert Transform

The HT is widely used in SHM to obtain the *analytic signal* of a real-valued time series, enabling the extraction of envelope and instantaneous phase information. In this study, the envelope signal, derived from the HT, is used as a feature representation for GW signals, as it provides indication of energy variations may be associated with the presence and progression of delamination. Since damage typically induces attenuation and scattering in GWs, the envelope of the signal becomes an informative metric for monitoring energy loss and localizing structural changes. Mathematically, the analytic signal  $s_a(t)$  is expressed as:

$$s_a(t) = s(t) + j\mathcal{H}\{s(t)\} \quad (2-16)$$

where  $s(t)$  is the real-valued input signal and  $\mathcal{H}\{s(t)\}$  is its Hilbert Transform. The envelope is then calculated as:

$$\text{Envelope}(t) = |s_a(t)| = \sqrt{s(t)^2 + \mathcal{H}\{s(t)\}^2} \quad (2-17)$$

This envelope signal is further used in the development of damage indicators and input features for deep learning-based prognostic models.

#### 2.4.2 Continuous Wavelet Transform

The CWT provides a time, frequency representation of a signal by decomposing it into wavelets, localized oscillatory functions that can capture transient features in both time and frequency domains [95]. Unlike the STFT, which uses fixed-size windows, the CWT adapts its time–frequency resolution through scaling and translation of the analyzing wavelet [96]. Let  $x(t) \in L^2(\mathbb{R})$  be a continuous signal. The CWT  $x(t)$  with respect to a wavelet  $\psi(t) \in L^2(\mathbb{R})$  is defined as:

$$\mathcal{W}_x(a, b) = \int_{-\infty}^{\infty} x(t) \cdot \frac{1}{\sqrt{|a|}} \psi^* \left( \frac{t-b}{a} \right) dt \quad (2-18)$$

where  $a \in \mathbb{R}^+$  is the scale parameter (inversely proportional to frequency),  $b \in \mathbb{R}$  is the translation parameter (shifts the wavelet in time),  $\psi(t)$  and is the mother wavelet, a function that satisfies the admissibility condition:

$$C_\psi = \int_{-\infty}^{\infty} \frac{|\hat{\psi}(\omega)|^2}{|\omega|} d\omega < \infty \quad (2-19)$$

where  $\hat{\psi}(\omega)$  is the Fourier transform of  $\psi(t)$ ,  $*$  denotes complex conjugation. The time-frequency resolution of CWT depends on the selected mother wavelet. Commonly used wavelets include Morlet and Complex Gaussian wavelets, each offering different trade-offs between time and frequency localization. In **Figure 2.8** some example of motherwavelets that can be used in the transform are shown [97].

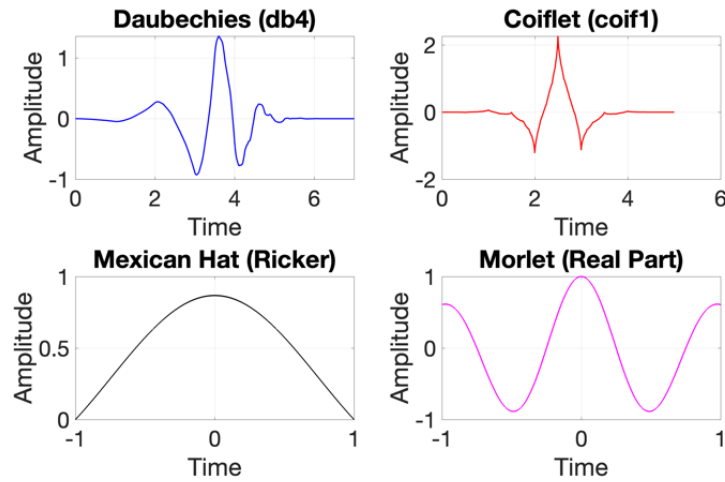


Figure 2.8. Example of mother wavelets.

The CWT coefficients  $\mathcal{W}_x(a, b)$  represent the similarity between the signal and the scaled, shifted wavelet. High coefficients indicate strong correlation at a particular scale and time, making CWT ideal for detecting localized signal features such as abrupt changes, reflections, or dispersive components.

The scalogram, defined as  $|\mathcal{W}_x(a, b)|^2$ , is often used to visualize signal energy distribution across time and frequency. CWT is redundant and continuous in both scale and time, which leads to high resolution representations but also greater computational cost. For applications requiring precise detection of non-stationary behavior or fine grained spectral content, CWT remains a preferred tool.

### 2.4.3 Discrete Wavelet Transform

The Discrete Wavelet Transform (DWT) is a multi-resolution, non-redundant transform that decomposes a signal into approximation and detail components across multiple levels [98]. Unlike the Continuous Wavelet Transform (CWT), which analyzes signals continuously over a range of scales and time shifts, DWT operates on discrete scales and time positions, resulting in a more computationally efficient and compact representation. In this study, DWT is explicitly utilized at the denoising step. The denoising process involves decomposing the signal into wavelet components and applying thresholding to the detail coefficients, which predominantly contain high-frequency noise. The DWT denoising step effectively retains the underlying structural information while reducing the influence of measurement noise and environmental disturbances by suppressing or removing these noise-dominated components and reconstructing the signal using the modified coefficients. This approach enhances the clarity and reliability of the raw GW signals prior to further analysis [99].

The DWT of a discrete signal  $x[n] \in \ell^2(\mathbb{Z})$  is based on a two-channel filter bank structure comprising: a low-pass filter  $h[n]$  to extract approximation coefficients and a high-pass filter  $g[n]$  to extract detail coefficients. The decomposition at level  $j$  is defined by:

$$A_j[k] = \sum_n h[n - 2k] \cdot A_{j-1}[n], D_j[k] = \sum_n g[n - 2k] \cdot A_{j-1}[n] \quad (2-20)$$

where  $A_j[k]$  are the approximation coefficients at level  $j$ ,  $D_j[k]$  are the detail coefficients at level  $j$ ,  $A_0[k] = x[k]$  is the original signal, down sampling by a factor of 2 is applied after filtering to ensure orthogonality. The filters  $h[n]$  and  $g[n]$  are derived from the scaling function  $\phi(t)$  and the wavelet function  $\psi(t)$ , which satisfy the two-scale equations:

$$\phi(t) = \sum_n h[n] \cdot \phi(2t - n), \psi(t) = \sum_n g[n] \cdot \phi(2t - n) \quad (2-21)$$

## 2.5 Deep Learning for Non-Linear Regression

DL has emerged as a powerful tool for solving regression tasks. In DNN, the regression task is accomplished by training a neural network to map the input features to the desired output through a series of hierarchical transformations [100]. The core of DNN models is MLP, which consists of multiple layers of interconnected neurons. Each neuron performs a weighted sum of its inputs, followed by a non-linear activation function, allowing the network to capture complex patterns in the data. In addition to fully connected networks like MLPs specialized architectures such as CNN and LSTM networks are also effective for regression tasks. MLPs are versatile and commonly used for general regression problems, while CNNs excel when the input data has spatial structure, such as images or time-series data, by automatically learning relevant features through convolutional layers. LSTMs, on the other hand, are designed for sequential data, capturing long-term dependencies and temporal patterns, making them well-suited for tasks like time-series forecasting [101].

### 2.5.1 Multilayered Perceptron

In a standard MLP architecture for regression, multiple hidden layers are placed between the input and output layers. The depth of the network, reflected by the number of layers, enables the model to learn abstract representations of the input, which is particularly beneficial in handling high-dimensional or non-linear relationships. In **Figure 2.9**, a neuron in a hidden layer is illustrated in a feed-forward propagation. The term  $a_m^l$  denotes the input from connected neurons in the previous layer, where  $m$  represents the number of neurons, and  $w$  is the weight with an associated bias term  $b$ . The activation function,  $func_{act}$  can be either linear or nonlinear and allows MLP to capture complex data patterns. Well-adapted activation functions include the rectified linear unit (ReLU), sigmoid, and hyperbolic tangent (tanh) [102].

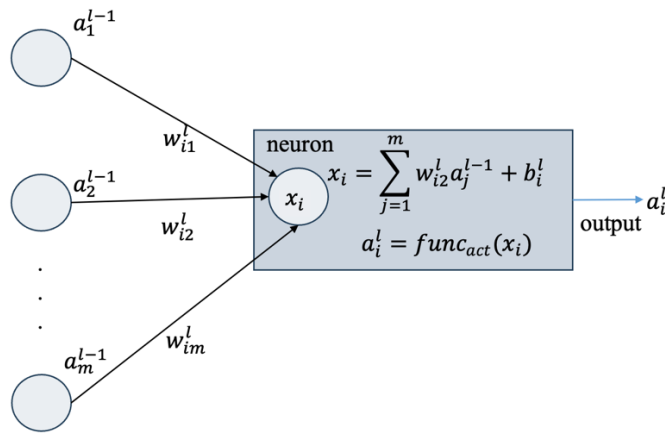


Figure 2.9. Neuron functions in feed-forward propagation.

$$\text{ReLU}(x) = \max(0, x) \tag{2-22}$$

$$\text{sigmoid}(x) = \frac{1}{1+e^{-x}} \tag{2-23}$$

$$\text{tanh}(x) = \frac{e^x - e^{-x}}{e^x + e^{-x}} \tag{2-24}$$

### 2.5.2 Convolutional Neural Networks

CNNs are a specialized class of DL models designed to process data with a grid-like structure, such as images, video frames, or even time series. **Figure 2.10** demonstrate the CNN architecture along with its constituent layers. The core building block of a CNN is the convolutional layer, which applies a set of filters (or kernels) across the input data to detect local patterns. This operation is essential because it allows the network to recognize features such as edges, textures, and shapes by capturing spatial hierarchies of data. As the network deepens, the layers build up these features into increasingly complex representations,

enabling the model to perform tasks like image classification, object detection, and facial recognition with high accuracy [103].

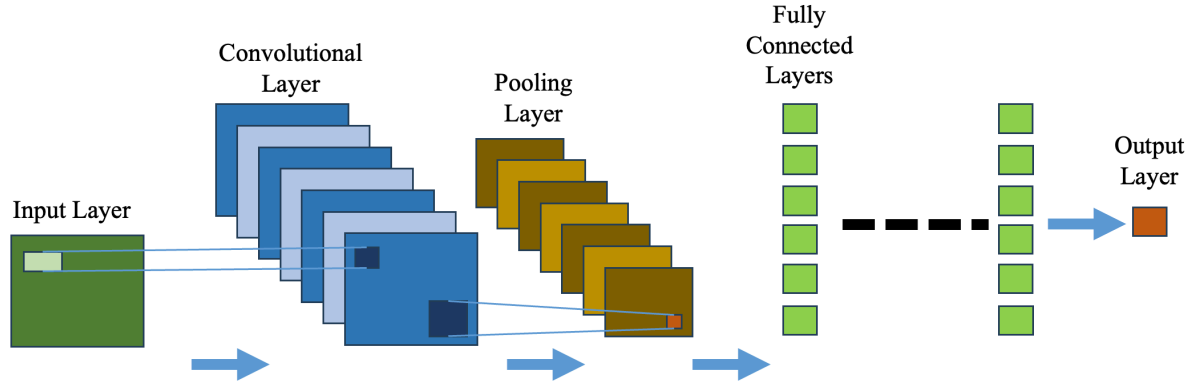


Figure 2.10. CNN architecture with input layer convolutional layer, pooling layer, fully connected layer and output layer.

CNNs incorporate pooling layers, which serve to reduce the spatial dimensions of the data while preserving the most significant information. Maxpooling is the most common technique, where the maximum value within a defined window is selected. This process not only reduces the computational load but also introduces a form of spatial invariance, making the model less sensitive to small shifts or distortions in the input. Following these layers, the network typically includes fully connected layers, where the high-level features extracted by the convolutional and pooling layers are combined to make final predictions. The entire network is trained end-to-end using backpropagation, allowing it to optimize its filters and weights to minimize the error in predictions.

$$(f * I)(x, y) = \sum_{i=0}^m \sum_{j=0}^n f(i, j) \cdot I(x + i, y + j) \quad (2-25)$$

$$p = \max\{x_1, x_2, \dots, x_n\} \quad (2-26)$$

While CNNs are often associated with 2D data like images, they can also be adapted for 1D data, such as time series. In a 1D CNN, the convolutional filters slide along one dimension of the data, making them ideal for capturing temporal patterns in sequences [104]. This approach is particularly effective for tasks like time series regression, where the goal is to predict a continuous output based on past values in a sequence [105]. By applying 1D convolutions, the network can learn to detect trends, cycles, and other temporal structures, making it a powerful tool for forecasting and analyzing time-dependent data. In time series regression, the 1D CNN processes the input sequence to extract meaningful features, which are then used to predict future values or identify underlying patterns in the data.

### 2.5.3 Long-Short Term Memory (LSTM)

LSTM is a type of Recurrent Neural Network architecture designed to learn and remember long-term dependencies in sequential data. Introduced by Hochreiter and Schmidhuber in 1997 [106], LSTMs are specifically engineered to address the limitations of traditional RNNs, which struggle with the vanishing gradient problem, making them ineffective at capturing long-term dependencies. **Figure 2.11** presents an LSTM unit with input and output parameters.

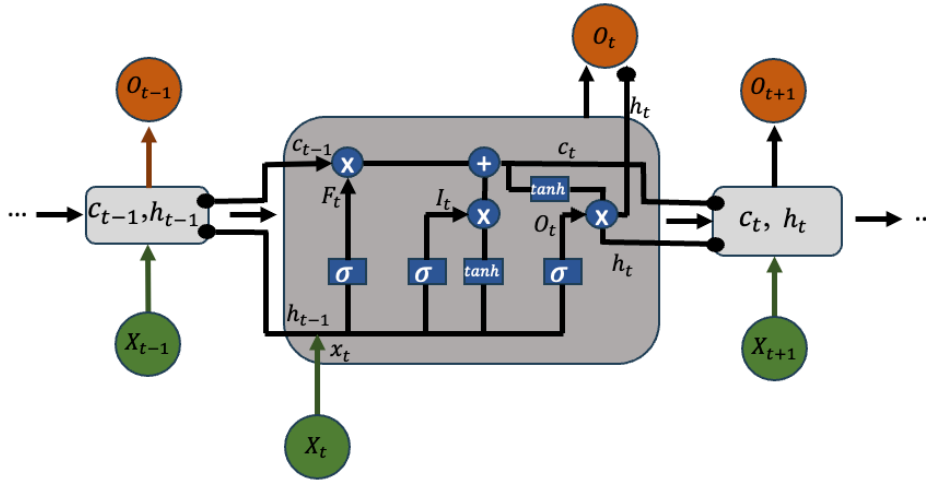


Figure 2.11. A unit of an LSTM cell.

1. **Memory Cell:** At the core of LSTM is the memory cell, which retains information over time. The cell state acts as a highway, with minimal linear interactions, allowing information to flow unchanged, thereby preserving long-term memory.
2. **Gates:** LSTMs utilize a series of gates to regulate the flow of information into and out of the cell. These gates are controlled by learned weights that decide which information is relevant to keep or discard:

- **Forget Gate (\$F\_t\$):** decides what portion of the cell state should be forgotten. It takes the current input and the previous hidden state as input and outputs a number between 0 and 1 for each number in the cell state, where 1 means “completely keep this” and 0 means “completely forget this”.

$$F_t = \sigma(W_f \cdot [h_{t-1}, x_t] + b_f) \tag{2-27}$$

- **Input Gate (\$I\_t\$):** This gate determines what new information should be stored in the cell state. It decides which values to update using a combination of the current input and the previous hidden state.

$$i_t = \sigma(W_i \cdot [h_{t-1}, x_t] + b_i) \tag{2-28}$$

- **Output Gate (\$O\_t\$):** This gate decides what the next hidden state should be, which is also used for predictions. It controls how much of the cell state should be output.

$$o_t = \sigma(W_o \cdot [h_{t-1}, x_t] + b_o) \tag{2-29}$$

3. **Cell State Update:** The cell state is updated based on the input and forget gates. The input gate modulates which new information flows into the cell state, while the forget gate controls the decay of old information.

$$C_t = f_t * C_{t-1} + i_t * \tilde{C}_t \tag{2-30}$$

where  $\tilde{C}_t$  is the candidate cell state, computed as:

$$\tilde{C}_t = \tanh(W_C \cdot [h_{t-1}, x_t] + b_C) \tag{2-31}$$

4. **Hidden State Update:** The hidden state, which is passed to the next time step and used for making predictions, is updated based on the output gate and the cell state.

$$h_t = o_t * \tanh (C_t) \quad (2-32)$$

#### 2.5.4 Optimization and Regularization

Training a DNN model for regression involves adjusting neuron weights and biases to minimize a loss function, which measures the difference between predicted outputs and actual labels. This is achieved using optimization algorithms such as stochastic gradient descent or its variants, like Adam [107].

Adam is an adaptive optimization algorithm, given in equations 2-25; 2-28, where  $\eta$  is the initial learning rate,  $g_t$  is the gradient at  $t$  each feedforward iteration along  $\omega_t$ ,  $v_t$  is the exponential average of gradients along  $\omega_t$ ,  $s_t$  is the exponential average of squares of gradients along  $\omega_t$  and  $\beta_1, \beta_2$  are hyperparameters to control the exponential decay rates of the moving averages. Adam optimization maintains two moving averages of the gradients and adapts learning rates for different parameters based on their historical gradients, often leading to faster convergence and greater robustness to noisy gradients compared to traditional SGD methods.

$$N_t = \beta_1 * v_{t-1} - (1 - \beta_1) * g_t \quad (2-33)$$

$$s_t = \beta_2 * s_{t-1} - (1 - \beta_2) * g_t^2 \quad (2-34)$$

$$\Delta\omega_t = -\eta \frac{v_t}{\sqrt{s_t + \epsilon}} * g_t \quad (2-35)$$

$$\omega_{t+1} = \omega_t + \Delta\omega_t \quad (2-36)$$

Two widely utilized loss functions in learning models are the Mean Squared Error (MSE) and the Mean Absolute Error (MAE). These functions play a critical role in guiding the optimization process by quantifying the discrepancy between the predicted outputs and the actual target values, thereby influencing the model's ability to generalize and perform effectively on unseen data. MSE is a commonly used metric to evaluate the accuracy of a predictive model. It measures the average squared difference between actual and predicted values. By squaring the differences, it penalizes larger errors more than smaller ones, making it useful when significant errors need to be emphasized. Since MSE squares the error terms, it gives greater weight to larger errors, making it particularly sensitive to outliers. The MAE is a straightforward loss function that calculates the average of absolute differences between actual and predicted values. It is widely used for evaluating regression models because it directly measures the magnitude of errors in the same unit as the data. The mean absolute percentage error (MAPE) is a metric used to measure the accuracy of a predictive model. It calculates the average percentage error by comparing the actual and predicted values. MAPE is useful because it expresses errors as a percentage, making it easy to interpret and compare across different datasets. However, one of its limitations is that it becomes problematic when actual values contain zero, as division by zero is undefined.

$$MSE = \frac{1}{n} \sum_{i=1}^n (y_i - \hat{y}_i)^2 \quad (2-37)$$

$$MAE = \frac{1}{n} \sum_{i=1}^n |y_i - \hat{y}_i| \quad (2-38)$$

$$MAPE = \frac{1}{n} \sum_{i=1}^n \left| \frac{y_i - \hat{y}_i}{y_i} \right| \times 100 \quad (2-39)$$

where  $y_i$  represents the actual values,  $\hat{y}_i$  represents the predicted values,  $n$  is the total number of observations.

Dropout is a regularization technique used to mitigate overfitting in DNNs by reducing the risk of complex co-adaptations among neurons during training. It achieves this by randomly dropping out a subset of neurons in each training iteration, forcing the network to develop more robust and generalized representations. The mathematical formulation for the dropout layer is expressed as follows:

$$\hat{w}_j = \begin{cases} 0, & \text{with } P(c) \\ w_j, & \text{otherwise} \end{cases} \quad (2-40)$$

where  $\hat{w}_j$  is the diluted row and  $P(c)$  is the probability  $c$  to remove a row in the weight matrix [108].

During the training phase, the model iteratively adjusts its parameters to minimize the loss function, which quantifies the difference between predicted and actual values. MSE is used to measure performance throughout the training process in the proposed learning frameworks. To efficiently update the model, data is divided into smaller subsets known as batches, allowing mini-batch gradient descent to optimize learning. A portion of the dataset is reserved randomly for validation to ensure the model generalizes well to unseen data. The validation loss is continuously monitored to track the model's performance. Early stopping is used during the training phase, which is not traditionally classified as a core regularization technique, but it serves as an implicit form of regularization by preventing excessive training and overfitting. Unlike explicit regularization methods that modify the model parameters or loss function, early stopping limits the number of training iterations by stopping training when the validation loss stops improving. This prevents the model from learning patterns that do not generalize well while also improving computational efficiency. Early stopping also improves computational efficiency by avoiding unnecessary training beyond the point of diminishing returns. After training, the model undergoes testing on an unseen dataset to evaluate its generalization ability.

### 2.5.5 Normalization

Normalization is a crucial preprocessing step in DL that transforms input features into a common scale to improve model performance and training stability. This helps prevent issues related to large or inconsistent feature magnitudes, allowing neural networks to converge faster and generalize better. Two widely used normalization techniques are [0,1] normalization, also known as Min-Max Scaling, and Z-score standardization, also known as Standardization. Normalization, or Min-Max Scaling, transforms the data into a fixed range, typically between 0 and 1, ensuring that all features contribute proportionally to the model. It is calculated using the following formula  $x$  is the original value and  $x_{norm}^{(i)}$  denote the normalized value for the  $i$ -th data point.  $x_{max}$  refers the maximum value within the vector of a degradation history corresponding to each DI.

$$x_{norm}^{(i)} = \frac{x^{(i)} - x_{min}}{x_{max} - x_{min}} \quad (2-41)$$

This technique is useful when data is bounded and needs to be mapped to a fixed interval, which is especially beneficial for activation functions like sigmoid and ReLU, as they are sensitive to input scales. However, Min-Max scaling can be affected by outliers since extreme values directly influence the transformation. Standardization involves transforming the data to have a mean of 0 and a standard deviation of 1. This process ensures that the features are centered around zero and have a consistent scale, making it easier for the model to converge during training. The transformation is performed using the Eq. (2-34) where  $X$  is the original feature value,  $\mu$  is the mean of the feature,  $\sigma$  is the standard deviation of the feature, and  $X'$  is the standardized value.

$$X' = \frac{X - \mu}{\sigma} \quad (2-42)$$

In this study, Z-score standardization is applied to the time history of each path for each sample when incorporating data from multiple paths and specimens, ensuring a mean of zero and a standard deviation of one to mitigate scale variations. For single-sample-based analyses, Min-Max normalization is employed to rescale data to a common range, preserving relative feature distributions when the focus is in one specimen domain [109].

## **3 Compression-Compression Fatigue Testing after Impact**

### 3.1 Introduction

This chapter presents the conducted CAI testing from two perspectives: the first is from a mechanical point of view, with two sub-sections: CAI test and delamination state quantification, and the second is SHM implementation. Under the CAI test section, design parameters are given for sample preparation, impact testing, and fatigue testing. The following second subsection is devoted to present ultrasonic C-scan technique and labeling each sample's different delamination stages during their fatigue life. This chapter also discusses the integration of GW-SHM and EMI-SHM techniques into compressive fatigue testing. The data collection framework and the placement of sensors on the test samples are detailed, with dedicated subsections for the specific applications of both the EMI and GW methods, providing essential experimental parameters and discussing its application in the setup.

### 3.2 CAI Test for Woven Composite Structures

#### 3.2.1 Desing of the CAI Experimental Setup

A large woven-type CFRP plate shown in **Figure 3.1** with a thickness of 5.5 mm has been sampled according to the ASTM D7136 [110] for CAI testing. The total number of identical samples cut out from the large plate is 15, with each sample having dimensions of 100 mm in width and 150 mm in length. **Figure 3.2** displays the edge image of one cut sample captured using a microscope.

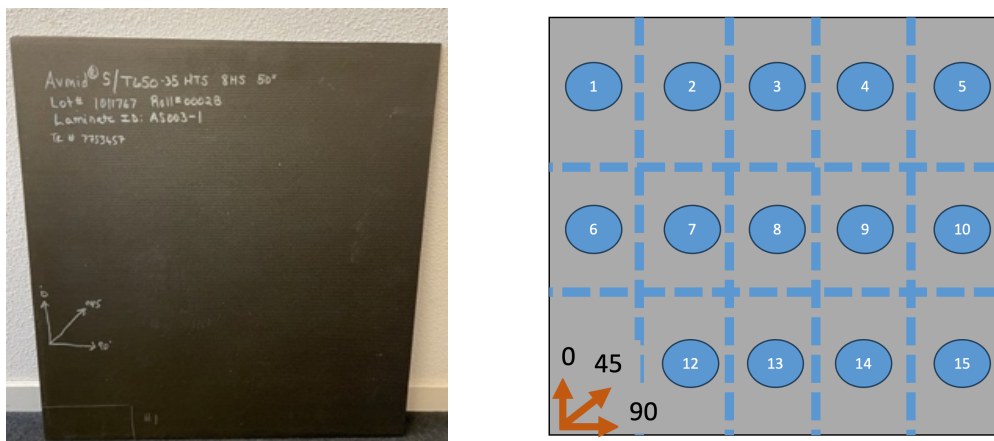


Figure 3.1. (a) Large healthy state panel; (b) cutting layout.

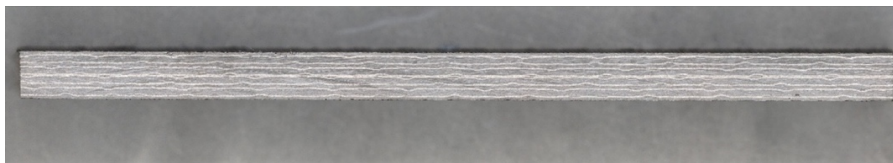


Figure 3.2. Microscopic image from the side edge of the cut CFRP sample.

The impact testing conducted with an impact tower creates low-velocity impacts prior to fatigue testing, providing valuable data on how initial damage affects the long-term durability and performance of the studied structures. **Figure 3.3** shows the sample installed in the impact testing setup. The impact energy is considered as the initial potential energy of the system, and it is calculated using Eq. (3-1), where  $mg$  represents the total weight of the tip and attached masses, and  $h$  is the distance from the sample's surface to the impact tip. Figure 2 illustrates the impact testing setup used to induce initial impact damage in each sample.

$$\text{Impact energy} = mgh \quad (3-1)$$

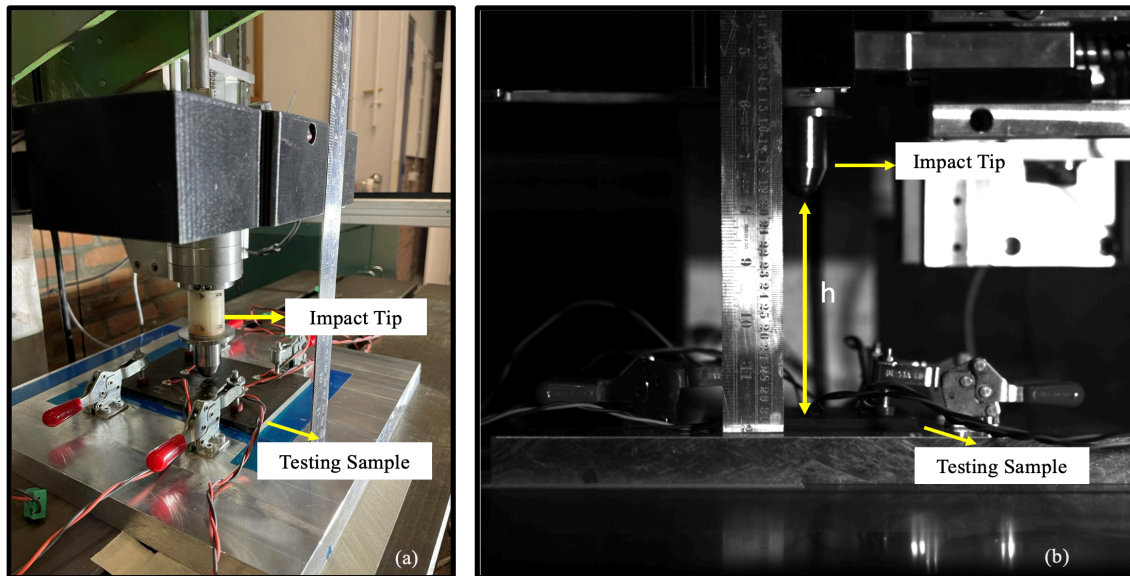


Figure 3.3. Impact testing setup (left) and impact energy calculation parameters (right).

**Figure 3.4** displays the experimental setup, presenting the impact testing, fatigue testing, and the anti-buckling fixture used in testing to prevent global buckling, along with the SHM unit, which facilitates data collection during fatigue testing. The acquisition step of the experiment is achieved through multiple data acquisition systems: GW, EMI, and pulse-echo ultrasonic C-scan. DIC measurement is configured with two cameras to measure the displacement variations in  $x$ ,  $y$ , and  $z$  coordinates through high-resolution images to obtain strain variations. DIC data has not been used in the scope of this thesis, yet, all data collected through the experiment can be found in [111]. The equipment list in the GW & EMI unit consists of a signal generator, EMI analyzer, multiplexor, oscilloscope, and computer.

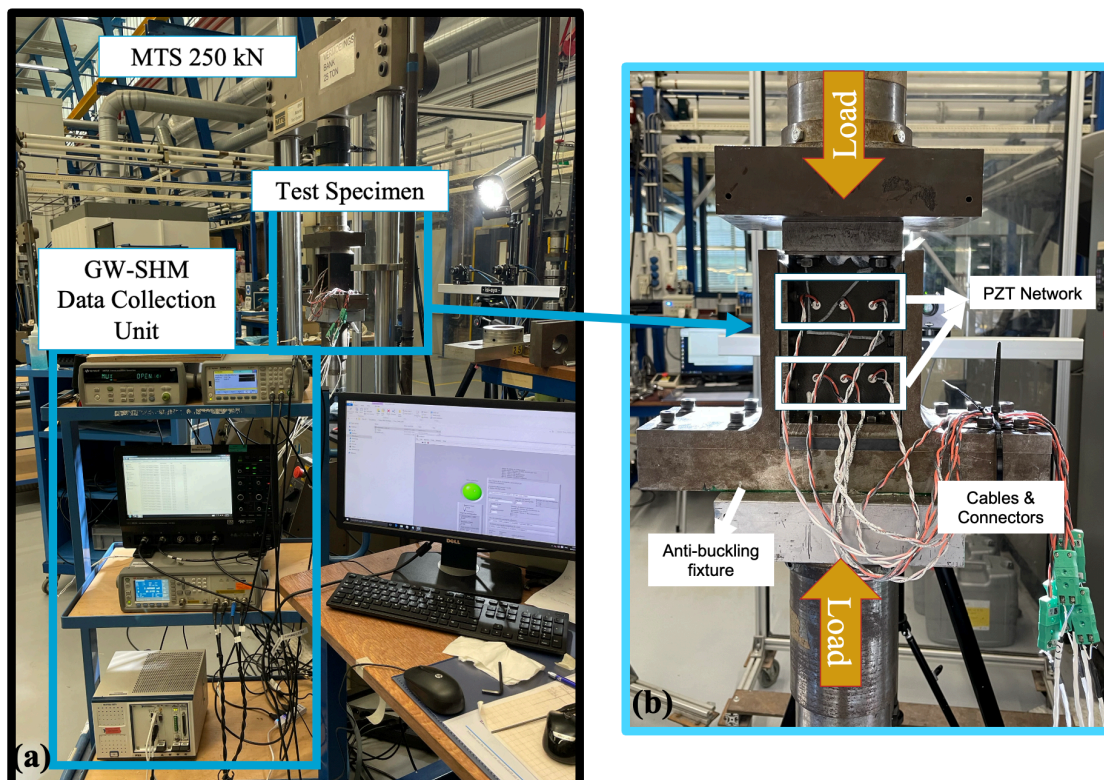


Figure 3.4. (a) Anti-buckling fixture and sensor-installed sample (b) SHM unit and fatigue testing MTS machine.

The data collection steps can be seen in **Figure 3.5**. In the initial phase of the experiment, the healthy state data was collected. In the second phase, low-velocity impact damages were introduced to the samples with a drop-weight tower, and another data acquisition step was conducted for after-impact state samples. While the healthy state and after impact state acquisition steps have been done in free boundary conditions, which means the sample was not located inside the fixture, and no in-plane stress was introduced, cycle 0 indicates that data was collected under low-stress conditions under the boundary conditions. In later processing, to compare fatigue data, cycle 0 has been used as reference/base state signal as data acquisition has been done under the same conditions with cycle 0 for each sample during the fatigue testing.

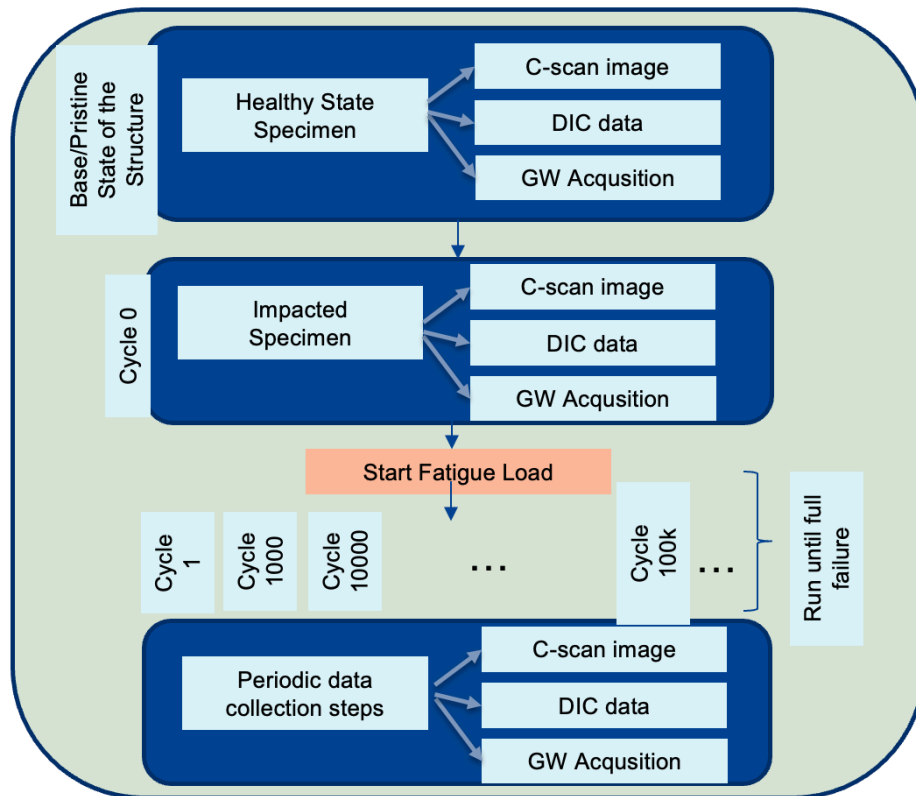


Figure 3.5. Data collection steps.

### 3.2.2 Fatigue Testing

Before initiating the fatigue testing, three impacted samples were tested under quasi-static (QS) compression to determine the fatigue loading parameters. The fatigue force has been aimed at 75% of the maximum QS stress. However, the variations in impact damages, in terms of their severity, affect the maximum load level for each sample. Eventually, this fact causes a variation in maximum load values, and thus, the applied load levels have been adjusted according to the impact damage severity. Data collection steps during the fatigue testing are implemented after each QS and cyclic loading by holding the  $F_{min}$  constant. Fatigue testing starts with a slow cycle with a 1 Hz frequency, and later cycles are executed with a 5 Hz frequency with a load ratio of 10. **Figure 3.6** shows the graphic illustration of the applied force during the fatigue testing.

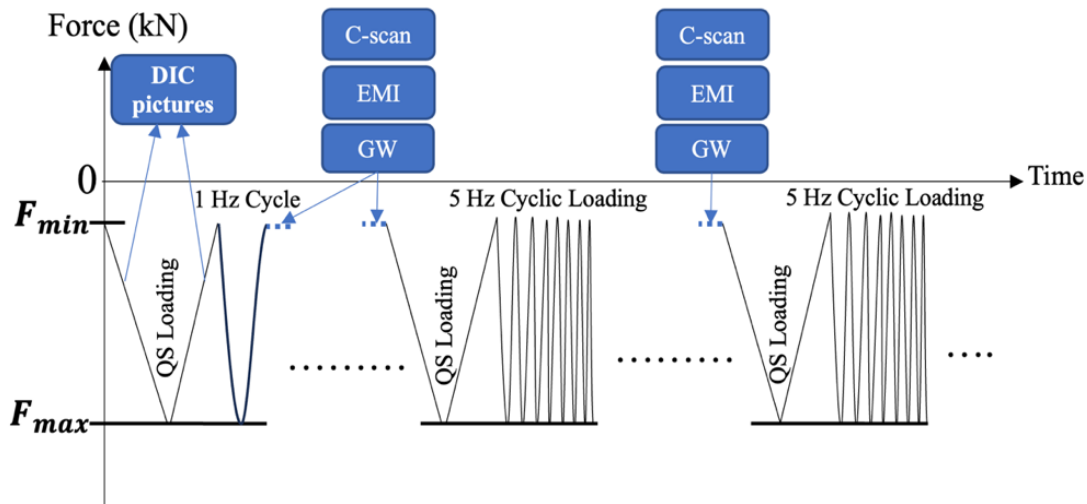


Figure 3.6. Fatigue loading and data acquisition steps.

In the dataset, constant load has been applied to five samples: Samples 2, 7, 9, 13, 14, and 15. Sample 8 and Sample 11 have also been fatigued under constant amplitude load, and then the applied force is increased incrementally at the later cycles to investigate the gradually growing delamination. With a similar approach, Sample 2 is also subjected to constant loading except for its first loading cycle, in which the applied maximum load was higher than the defined fatigue force. Sample 10 initially experienced a higher load level before gradually decreasing force over later cycles. Sample 12 was subjected to a lower load level, and its load was gradually increased over the following cycles. Consequently, constant and non-constant fatigue conditions were explored within the dataset, and their details are given in **Table 3.1**. At the included cycle steps column cycle numbers highlighted with red colour indicates the cycle steps interpolated in DI extraction phase. **Figure 3.7** shows the end-of-life state inside the fixture and side edges for two different samples. At the end-of-life state no data could have been acquired as the sensors were dispatched due to catastrophic failure event.



Figure 3.7. Final failure; front view and side edge views of two different samples.

Table 3-1. Test parameters of CAI fatigue testing

Samples	Impact Energy (joule)	Max/Min Force (- kN/- kN)	EoL (fatigue cycles) x1000	Number of Measurement Steps	Max Applied Force (kN)	Prognostic Framework Included Cycle Steps 1 + x1000
Sample 2	19.45	$\frac{135}{13.5}$	79	12	-140	1-10-20-30-40-50-60-70
Sample 7	15.35	$\frac{140}{14}$	40,5	8	-140	1-5-10-15-20-25-30-35-40
Sample 8	15.35	$\frac{135}{13.5}$	2175	18	-145	1-10-20-30-40-50-60-70-80-90-100-150-200-210
Sample 9	15.35	$\frac{140}{14}$	97,2	14	-140	1-10-20-30-40-50-60-70-80-85-90-95
Sample 10	15.35	$\frac{135}{13.5}$	6,6	8	-150	1-2-3-4-5-6
Sample 11	15.35	$\frac{140}{14}$	183,7	20	-150	1-20-30-40-50-60-70-80-90-100-120-130-150-160-170-180
Sample 12	19.45	$\frac{130}{13}$	38,5	9	-137	1-5-10-15-20-25-30-35
Sample 13	16.31	$\frac{140}{14}$	27,9	7	-140	1-5-10-15-20
Sample 14	15.35	$\frac{140}{14}$	21,3	7	-140	1-5-10-15-20
Sample 15	16.31	$\frac{135}{13.5}$	15,5	9	-135	1-2.5-4-7-8.5-10-11.5-13-14.5

### 3.3 Delamination State Labels

#### 3.3.1 Ultrasonic C-scan Technique

During the tests, the non-destructive test (NDT) kit (facilitated by the Dolphitech technology), shown in **Figure 3.8**, operates on the pulse-echo principle with an excitation center frequency of 8 MHz. It facilitates the reconstruction of delamination images through post-processing in two methods: one involves amplitude variation and the other utilizes time-of-flight information, enabling the acquisition of delamination images throughout the thickness. A low-pass filter is applied to the C-scan images as a post-processing step. The obtained images are presented in **Figure 3.9** for samples 2, 7, 9, 10, 14, and 15, as the delamination growth was present and could be captured via C-scan measurement. The initial damage states of Sample 8 and 11 demonstrated no measurable variation, which may be considered as they remained under the critical fatigue load limit or could be considered as an accumulation phase. Sample 12 and 13 are other two samples not listed in the C-scan results because of the high-noise effect in the images; thus, a linear growth regime is considered for samples 12-13. In C-scan images, the darkest blue color represents the last layer through the thickness. Delamination's shape varied in each sample, and its propagation acceleration differed at each

layer. It should be noted that the first ~1mm thickness of each sample is neglected to reduce the noise originated due to the reflection between the probe and the rough surface of woven samples. Despite this, it is evident in C-scan images that at the final state of delamination, called the threshold level, the deepest layer presents a noticeably higher growth rate in all the samples except Sample 10. In this study, the quantification method is chosen to be one-dimensional: the length in the direction of delamination growth manifests perpendicular to the direction of the applied load.

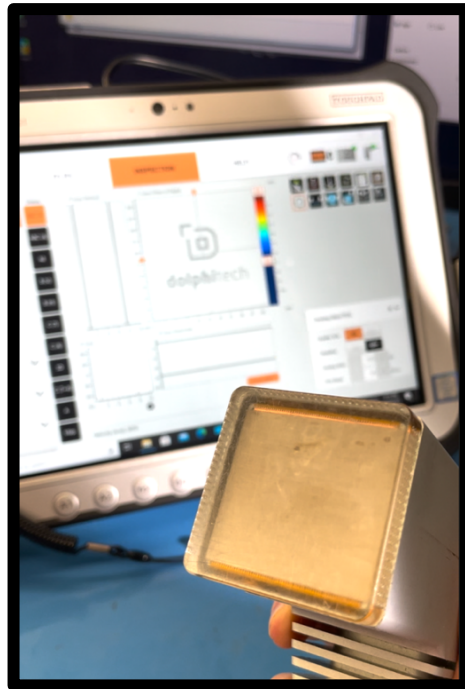
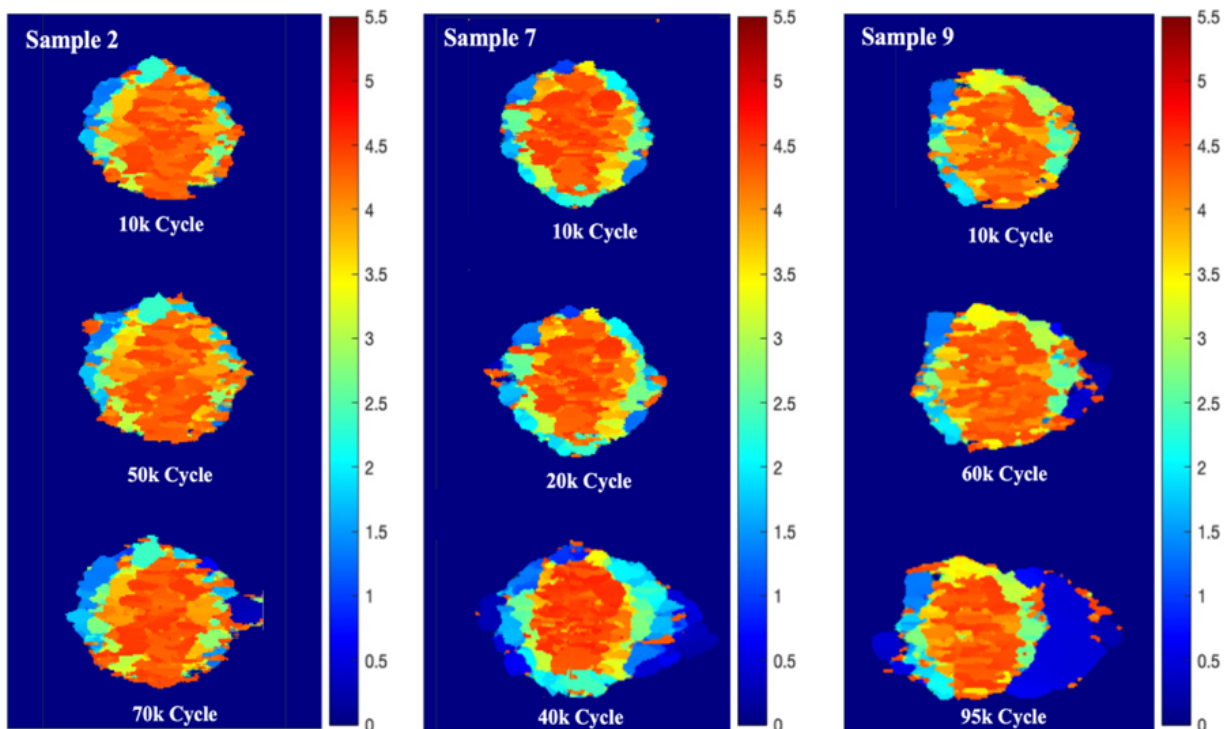


Figure 3.8. Pulse-echo NDT kit.



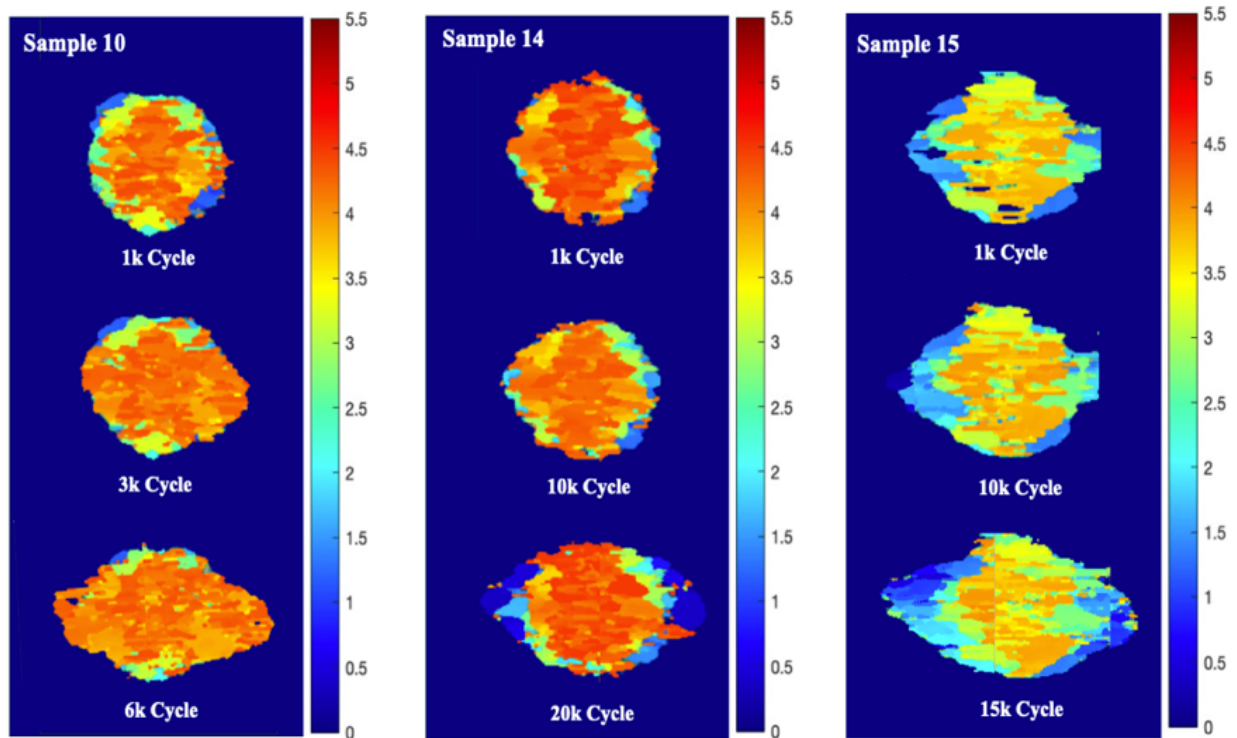


Figure 3.9. Ultrasonic c-scan images of delamination from six samples present gradual growth in their three-fatigue life level: initial, middle, final/threshold.

### 3.3.2 Determination of Threshold Levels

**Figure 3.10** shows the maximum measured length of delamination monitored via C-scan for Sample 7. As seen in the figure, a one-dimensional quantification method is employed in this study for the maximum length of the delamination growth that occurs perpendicular to the direction of the applied load. An equal final length is defined for the EoL of all the samples, with the evidence of delamination reaching both edges of the sample in the growth direction, which is limited by the width of the sample. Among the samples in the dataset, Sample 12 and Sample 13 are two samples whose damage state was not able to be labeled via C-scan because of the high-noise effect in the images; thus, these two samples were not involved in the prognostic models that target delamination length as the output. **Figure 3.11** represents the dataset showing the measured maximum delamination length of the samples during their fatigue life, corresponding RULs, assigned threshold, and all samples' measured delamination in their threshold. The term "threshold" level, given in **Figure 3.11**, occurs in the cycle step that is followed by a fast delamination propagation, resulting in final failure. Therefore, it indicates the last cycle step that allows for data acquisition and the damage length measurement. The threshold level is measured as a different value for each sample, and it is attributed as the critical damage length for the tested samples.

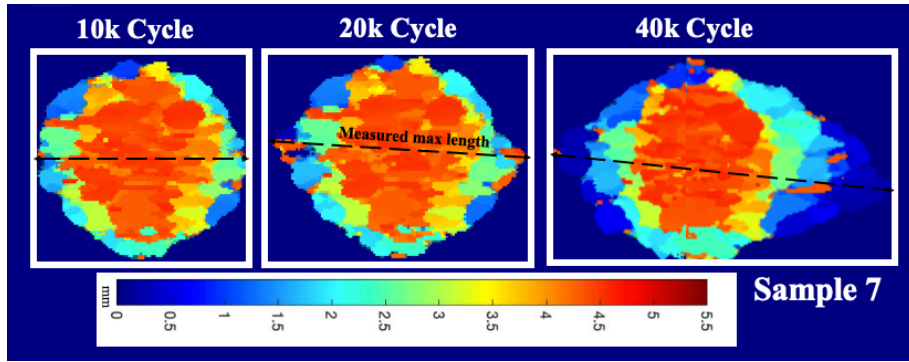


Figure 3.10. Sample 7 delamination labels.

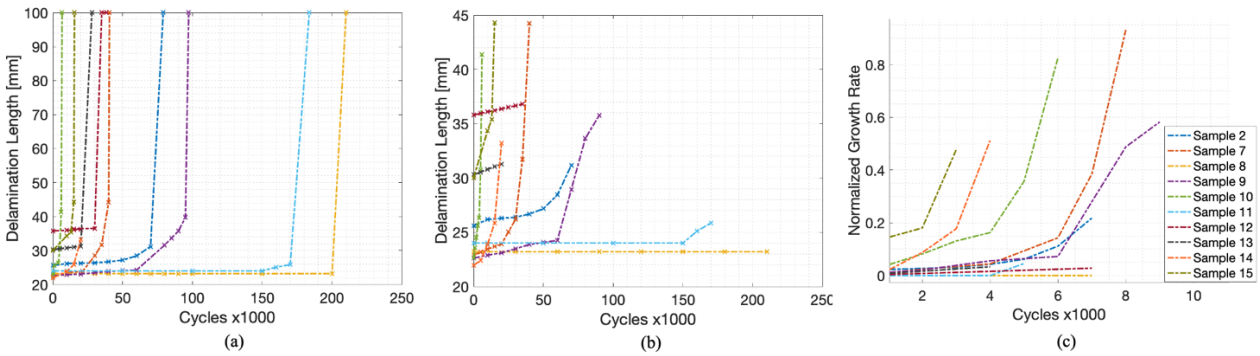


Figure 3.11. a) Delamination growth until EoL, b) RUL

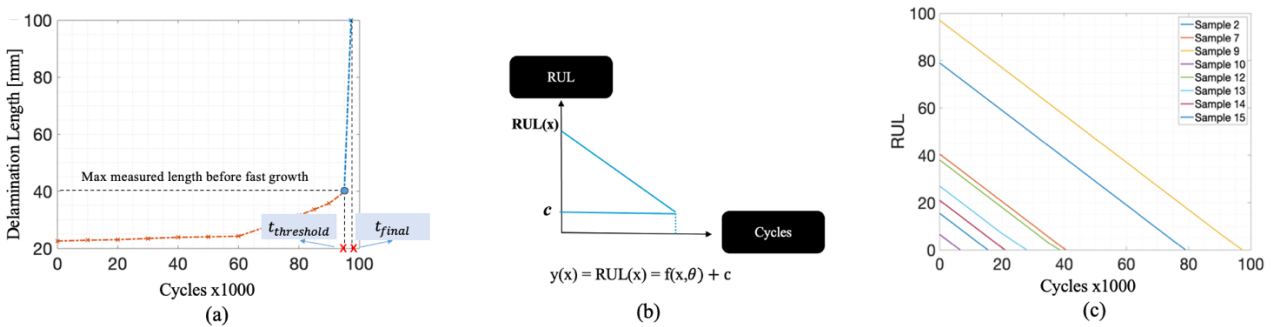


Figure 3.12. a) Measured delamination length for Sample 9, b) RUL definition, c) RUL for all samples.

It is important to note that a one-dimensional length-based measurement for severity quantification is inherently limited, as it cannot capture the variations in delamination across multiple layers or account for mixed damage types that co-occur within the structure. As a result, this approach provides only a partial representation of actual delamination severity. However, the maximum measured delamination length can still offer valuable insight into the overall progression of damage throughout the fatigue life of the sample. The measured delamination lengths (MDL) are indicated in **Figure 3.11**, for ten samples, where the threshold level shows the last step that allows for data collection before the failure.

According to **Figure 3.11**, below arguments can be given:

- The same initial impact energy induces delamination that varies in size and shape, resulting in different delamination growth rhythms and end-of-life (EoL) time.
- The maximum final delamination length is assumed to be identical for all the samples because it is constrained by the fixture, which is 100 mm in width. However, the delamination state in threshold level is different for each sample.

- As samples experience the load longer without a fast delamination growth, the delamination length in threshold state can reach a smaller value than the samples with delamination grow faster in earlier cycles. This situation can be seen between Sample 7, Sample 8, Sample 9, and Sample 11.

### 3.4 Implementation of Active-sensing based SHM Techniques in CAI Testing

#### 3.4.1 SHM Implementation in CAI Testing

A comprehensive SHM framework is achieved integrating GW, EMI, and ultrasonic techniques to monitor and analyze the progression of damage under fatigue loading in composite samples. **Figure 3.13** illustrates the components of this framework with the samples tested under C-C fatigue. GW signals provide insights into changes in material properties over time by analyzing wave propagation and amplitude variations, while EMI signals focus on frequency-based impedance changes to detect localized damage. Additionally, ultrasonic C-scan inspections offer visual confirmation of internal damage, such as delamination, at various fatigue cycles, complementing the data obtained from GW and EMI techniques. **Figure 3.14** contains the schematic diagram showing the placement of PZTs for GW signals and EMI data. The sensor network used for GW and EMI applications has 6 PZT transducers that are linearly distributed at the top and bottom sections of the sample. LOCTITE EA 9394 AERO [112] is a two-part structural paste adhesive is used to attach PZTs on the surface of the CFRP test samples. PIC255 type PZT disk transducers have been used in this experiment with a diameter of 8 mm, thickness 0.5 mm, with diameter and thickness frequency constants  $N_p$  and  $N_t$ ; 2000 and 1420 respectively where further information can be found in [113]. The length of the soldered cables is adjusted to 50 cm.

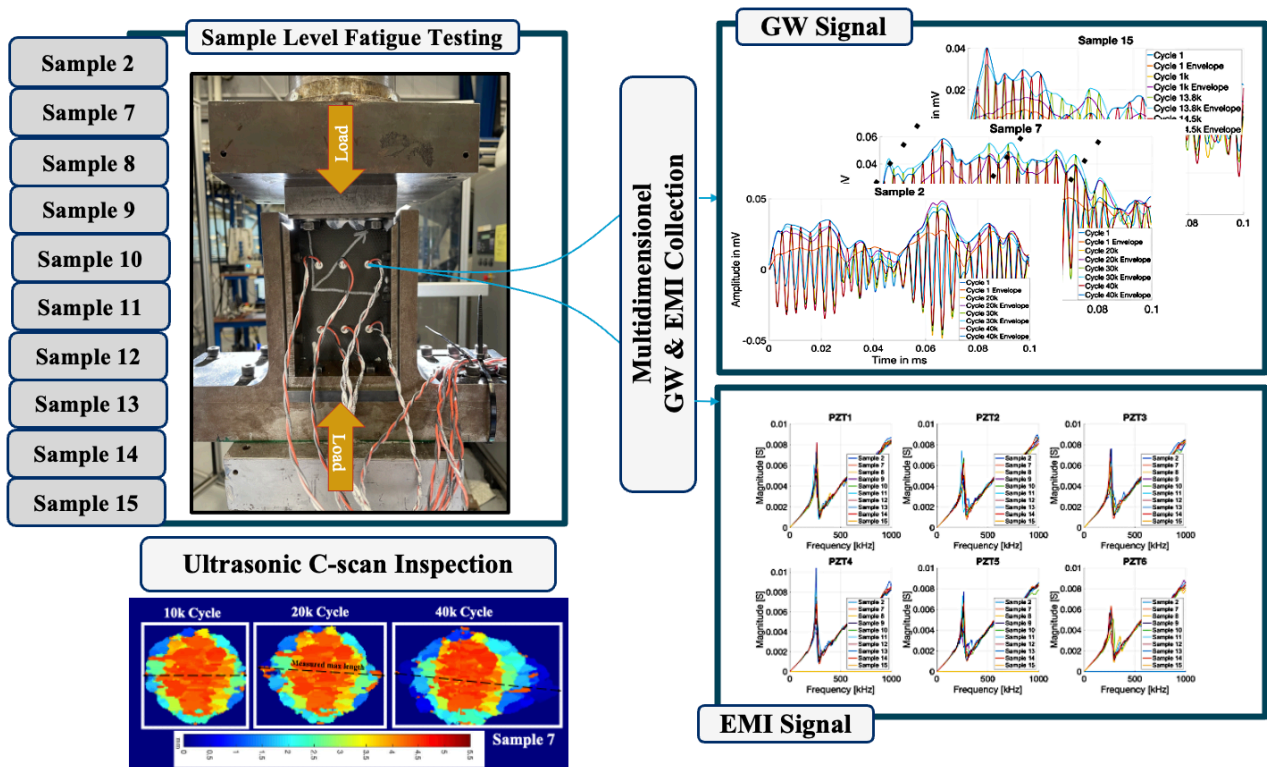


Figure 3.13. SHM framework integrating GW, EMI, and ultrasonic C-scan

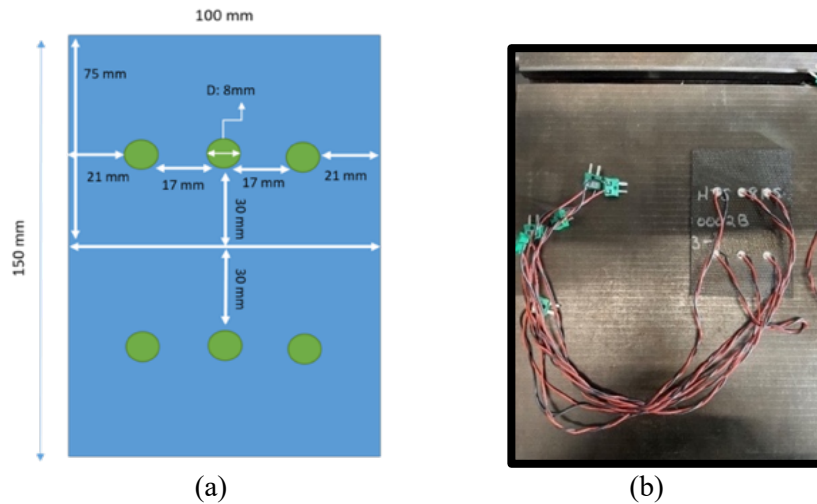


Figure 3.14. (a) Schematic diagram of sensor placement (b) sensor network installed sample.

### 3.4.2 EMI Acquisition

An alternating voltage is applied in a frequency range of 1 Hz to 1 MHz in this experiment. The resonant frequency occurs around  $280 \text{ kHz} \pm 10 \text{ kHz}$ , which matches the calculated resonant frequency through the diameter of PZT transducer PIC255 according to the given parameters in experimental setup section. Admittance has been measured for each six PZT at each acquisition step together with the GW signals. The measured admittance signatures of attached PZTs on healthy state samples are given in **Figure 3.15**. The resonant frequency occurs around  $280 \text{ kHz} \pm 10 \text{ kHz}$ , which is calculated as  $250 \text{ kHz}$  the calculated resonant frequency through the diameter of PZT transducer PIC255 with the ratio of  $N_p$  and diameter of PZT which is  $8 \text{ mm}$ .

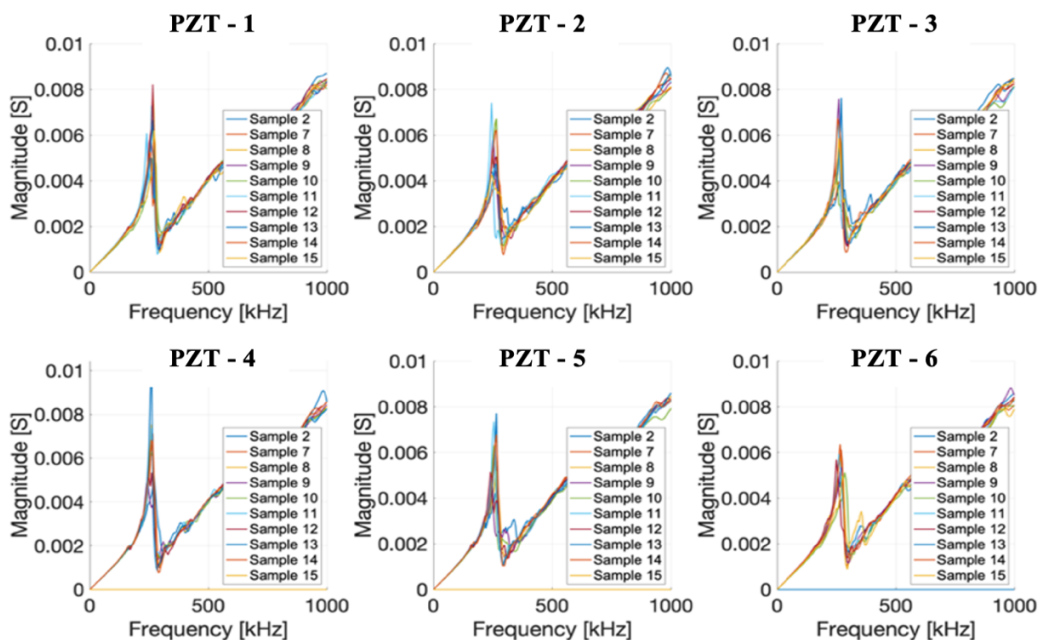


Figure 3.15. Admittance magnitude of no-damage samples for 6 PZTs.

### 3.4.3 GW Acquisition

The acquisition of GW data is performed using six PZT operating in a pitch-catch configuration. In this setup, each one PZT serves as the excitation source, generating GW signals, while the remaining five PZTs sequentially receive the transmitted signals. The experimental data acquisition parameters are presented in

Table 3.2. In this table,  $F_{s_{receive}}$  denotes the sampling frequency for receiving,  $F_{s_{exc}}$  represents the sampling frequency for excitation,  $T_{s_{receive}}$  refers to the receiving time duration, while  $T_{s_{exc}}$  corresponds to the excitation duration.  $t_{acq}$  is total duration of acquisition time.

Table 3-2. Signal acquisition parameters.

Parameter	Value
$F_{s_{receive}}$ (1/s)	5e6
$F_{s_{exc}}$ (1/s)	25e6
$T_{s_{receive}}$ (s)	2e-7
$T_{s_{exc}}$ (s)	4e-8
$t_{acq}$ (ms)	5

### 3.4.3.1 Excitation Signal

In the experiment, GW excitation signals are performed as 2-cycle tone-burst signals at the center frequency  $f_{exc}$  of 100 kHz, 120 kHz, 140 kHz, 160 kHz, and 180 kHz. The equation for the excitation signal is given as following:

$$x(t) = \frac{A}{2} \left[ 1 - \cos\left(\frac{2\pi f_{exc}}{N_{cycle}} t\right) \right] \sin(2\pi f_{exc} t) \quad (3-2)$$

where  $A=10V$ ,  $N_{cycle} = 2$ . Excitation signal is presented in **Figure 3.16** showing the excitation signal in time and frequency domain for each center frequency of excitation signal with power spectral density which describes how the power of a signal is distributed across different frequencies, representing the signal's power per unit frequency (e.g., W/Hz) and is computed as the squared magnitude of the Fourier Transform normalized by signal duration.

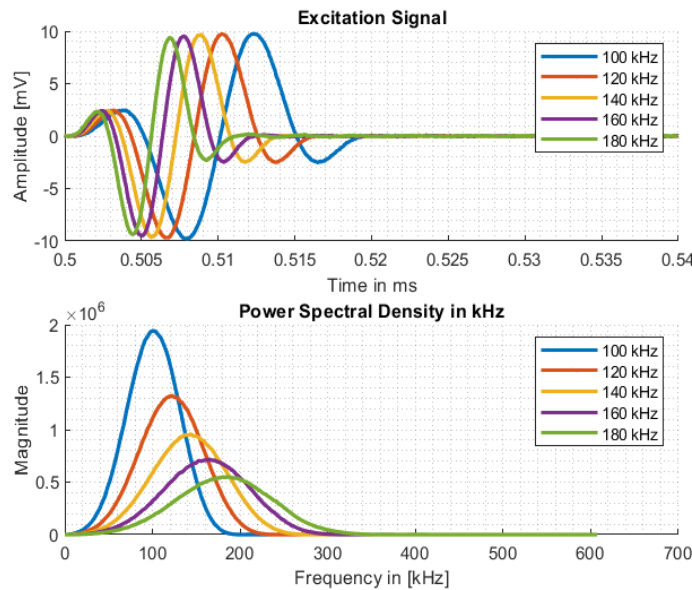


Figure 3.16. Excitation signal in time and frequency domain.

### 3.4.3.2 Received Signal

Accurate interpretation of GW signals requires careful signal pre-processing to mitigate noise, cross-talk, and unwanted frequency components. The steps outlined in this study, shown in **Figure 3.17**, the proposed methodology consists of two main phases: Pre-Processing and Denoising. The pre-processing phase consists of detrending, length reduction, cross-talk removal to refine the raw signal and residue signal calculation to eliminate unwanted components. At the pre-processing stage, after the crosstalk in the signal is removed and the length is reduced to total 1401 sample in the signal and the residue signal is obtained by subtracting the growing cycle signals from the base state cycle 0 signal to remove boundary reflection effects effectively isolating the changes introduced by structural damage. This is followed by the denoising phase, where a band-pass filter is applied to preserve relevant frequency components before DWT denoising is performed to further suppress noise. The methodology presented here ensures that only meaningful signal components are retained, minimizing distortions and improving the accuracy of GW-based prognostics.

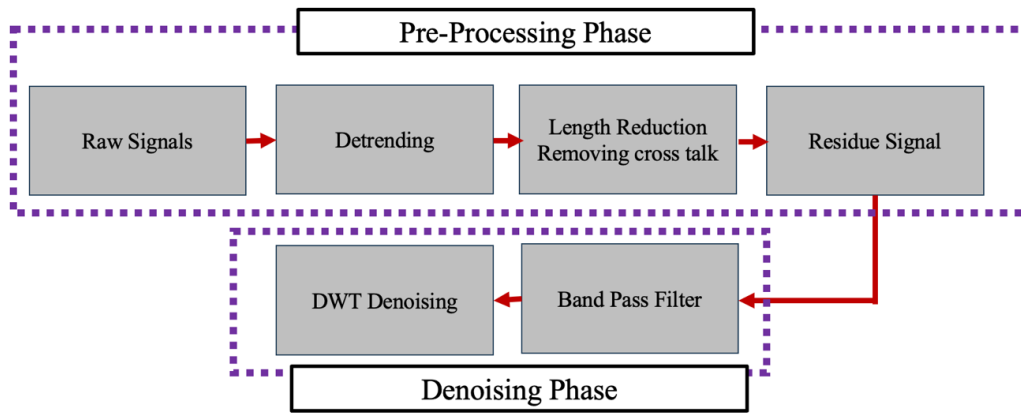


Figure 3.17. Signal pre-processing and denoising flowchart.

In the GW signal acquisition process, cross-talk effects occur in the received signal due to the excitation signal, particularly when transducers are attached to the same structure without adequate isolation, allowing vibrations from the excitation transducer to directly transfer to the receiving transducers and introduce undesired signals. To mitigate this interference, the time duration of the cross-talk signal is calculated, and the signal processing window is defined to begin after this period. The excitation signal consists of two cycles at selected frequencies of 100, 120, 140, 160 and 180 kHz. The duration of each excitation signal is determined as:

$$T_{exc} = \frac{N_{cycle}}{f_{exc}} \quad (3-3)$$

where  $N_{cycle} = 2$  is the number of excitation cycles,  $f_{exc}$  is the excitation frequency in Hz. The number of data points corresponding to the cross-talk duration is computed as Eq. (4-4) which is then rounded to the nearest integer:

$$N_{exc} = round(T_{exc} \times Fs_{receive}) \quad (3-4)$$

To avoid cross-talk interference, the starting index for the signal processing window is updated as:

$$N_{begin} = N_{initial} + N_{exc} \quad (3-5)$$

where  $N_{initial}$  represents the initial signal segment which has 2500 data sample points. In **Figure 3.18**, cross-talk removal process is presented.

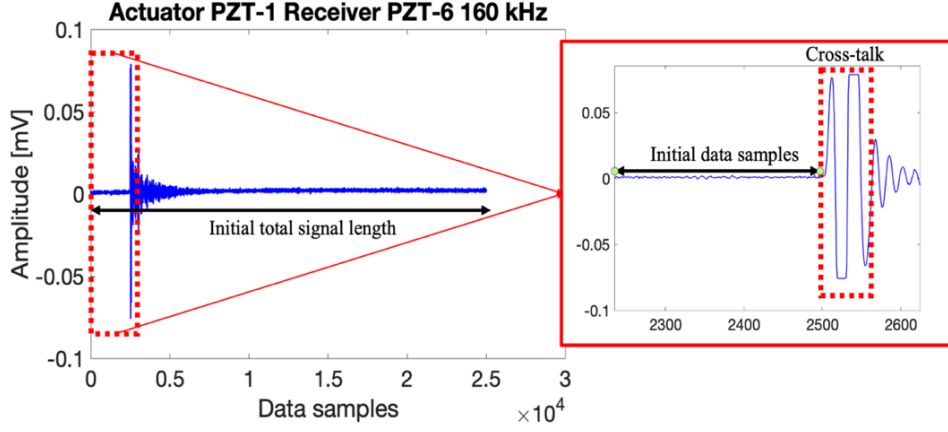


Figure 3.18. Raw GW signal cross-talk removal.

The denoising procedure contains bandpass filtering and discrete wavelet denoising through DWT. In **Figure 3.19**, denoising steps applied on pre-processed signal is shown. The bandpass filter range is determined by the excitation signal's lower and upper range in the frequency spectrum in **Figure 3.15**. A Butterworth band-pass filter is applied to extract a signal within a specific frequency range [52]. The band-pass filter is implemented by sequentially applying a high-pass filter followed by a low-pass filter using the function `butter` in MATLAB. To define the normalized cutoff frequencies, the lower and upper cutoff frequencies are given as:

$$\omega_{low} = \frac{F_{low}}{F_{Nyquist}}, \quad \omega_{high} = \frac{F_{high}}{F_{Nyquist}}, \quad F_{Nyquist} = \frac{F_{sampling_{receive}}}{2} \quad (3-6)$$

where  $F_{low}$  and  $F_{high}$  represent the lower and upper cutoff frequencies, respectively. The filtered signal is obtained using zero-phase filtering to prevent phase distortion, using the forward-backward filtering method, `filtfilt` function in MATLAB, with the order  $n = 4$ .

$$S_{filtered\_low} = \text{filtfilt}(b_{low}, a_{low}, S) \quad (3-7)$$

$$S_{filtered} = \text{filtfilt}(b_{high}, a_{high}, S_{filtered\_low}) \quad (3-8)$$

where  $S$  is the original signal, and  $S_{filtered}$  is the final band-pass filtered signal. After band-pass filtering, wavelet denoising is applied using multi-level wavelet decomposition. DWT is a denoising technique that enables the decomposition of GW signals into their frequency components. DWT decomposes the original time-domain signal by computing its correlation with a mother wavelet, namely Haar, Daubechies, Symlets, Biorthogonal, Morlet, and Coiflets wavelets are selected, in this work, and the best signal-to-noise ratio for different wavelets are used in the later processing phase. The DWT decomposition at level  $L$  is represented as:

$$x[n] = \sum_{l=1}^L d_l[n] + a_L[n] \quad (3-9)$$

where  $d_l[n]$  are the detail coefficients at level  $l$ ,  $a_L[n]$  are the approximation coefficients at level  $L$ . For each wavelet function  $\psi_j$ , denoising is applied using a thresholding function:

$$\hat{x}_j[n] = \text{func\_denoise\_dwt}(y[n], \psi_j, L) \quad (3-10)$$

where  $\hat{x}_j[n]$  is the denoised signal obtained using wavelet function  $\psi_j$ ,  $L$  is the decomposition level,  $\psi_j$  represents different candidate wavelet basis functions. The noise component of the signal is estimated as:

$$e_j[n] = y[n] - \hat{x}_j[n] \quad (3-11)$$

where  $e_j[n]$  represents the noise residual for wavelet function  $\psi_j$ . To evaluate the performance of different wavelet-based denoising methods, the Signal-to-Noise Ratio (SNR) is computed for each wavelet function:

$$\text{SNR}_j = 10 \log_{10} \left( \frac{\sum_n \hat{x}_j^2[n]}{\sum_n e_j^2[n]} \right), \quad j^* = \arg \max_j \text{SNR}_j \quad (3-12)$$

where  $\hat{x}_j[n]$  is the denoised signal for wavelet function  $\psi_j$ ,  $e_j[n]$  is the residual noise. A set of wavelet functions, listed above, is evaluated, and the optimal wavelet function is selected based on the maximum SNR value. The best denoised signal is then:

$$\hat{x}_{\text{best}}[n] = \hat{x}_{j^*}[n] \quad (3-13)$$

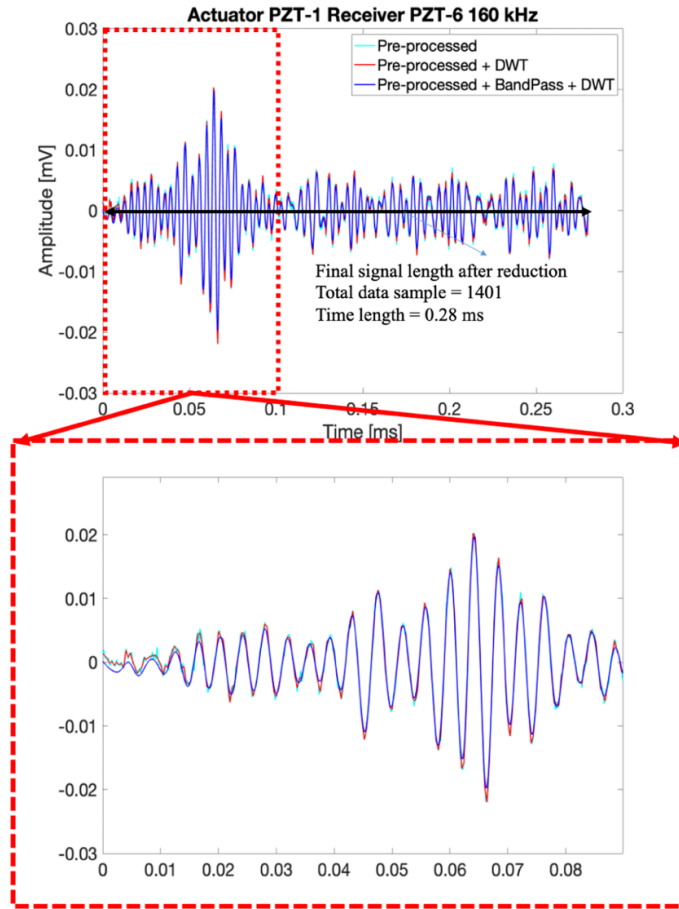


Figure 3.19. GW signal denoising steps.

The GW signals are acquired in the pitch-catch mode, which describes each PZT acting as an actuator and receiver step by step. While the top array PZTs are in actuator mode, only the bottom array acts as a receiver and vice versa. As a result,  $N_{\text{receiver}}$  is three for each actuator mode PZT while the total number of  $N_{\text{actuator}}$  is six, and 18 paths are accounted in total while the actual total collected path is 30 in the dataset. **Figure 3.20** illustrates the labels for each actuator-sensor pair considered in the pre/post-processing and DI extraction step. Total path number can be calculated considering pitch-catch configuration given as:

$$N_{\text{path}} = N_{\text{actuator}} \times N_{\text{receiver}} \quad (3-14)$$

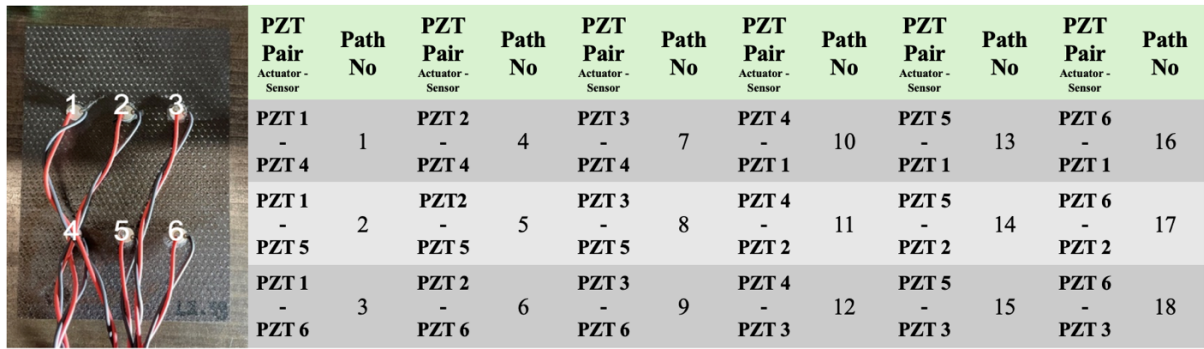


Figure 3.20. Surface-attached PZT network and actuator-sensor path labels.

In Figure 3.21, GW signals received from healthy state samples are shown for one path. Even though the samples were prepared to be identical, it can be assumed that there might be imperfections that may possibly affect the wave propagation characteristics. In fact, the first arrived wave portion demonstrates the repeatability of the signals for each sample and indicates that before impact damage was induced in the tested sample, the GW propagation was identical, except the variation in amplitude and before reflected signals arrive.

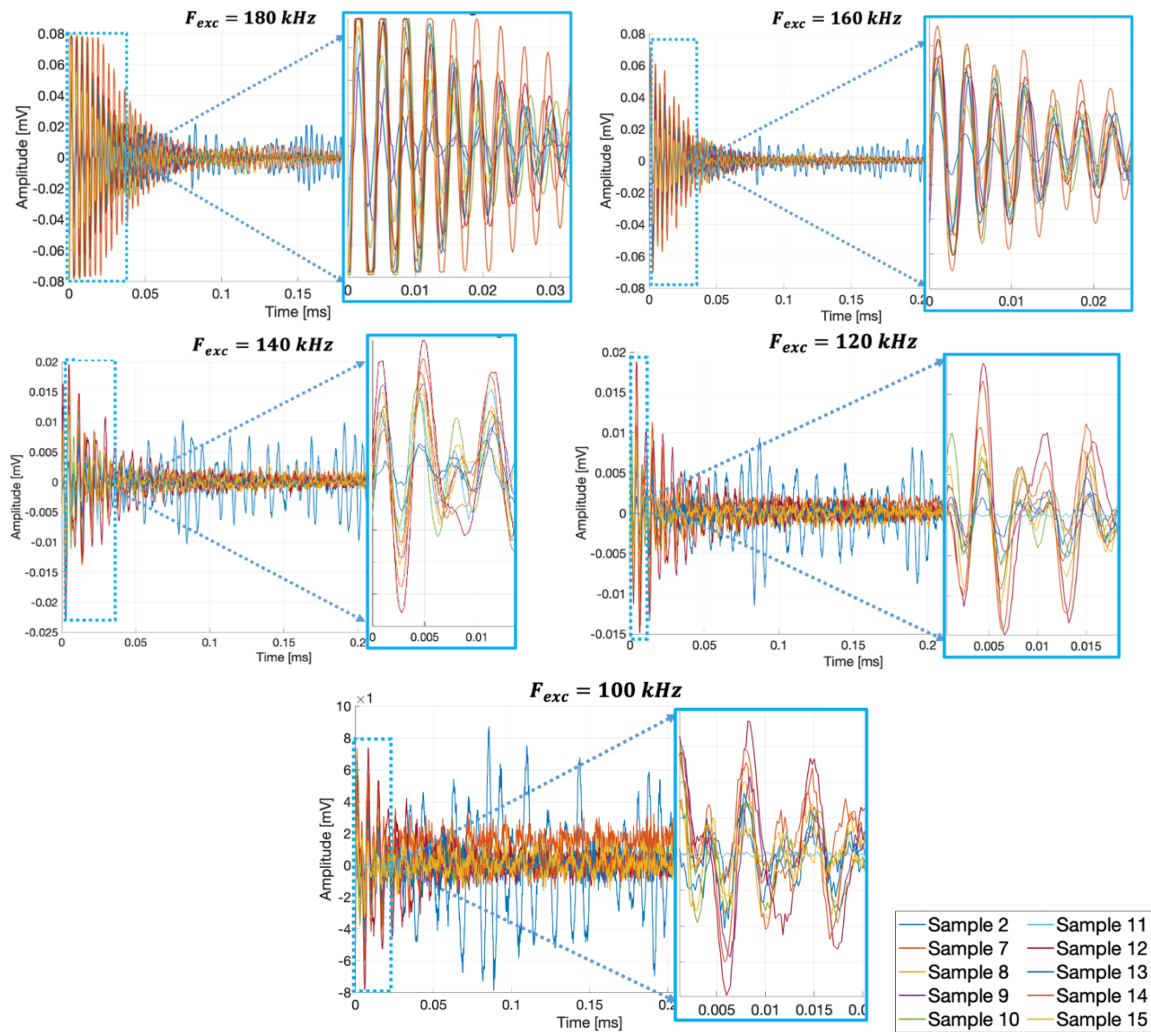


Figure 3.21. Received GW signals from healthy state path no 5.

## **4 Progressive Delamination Characterization via GWs & EMIs**

## 4.1 Introduction

This chapter is designed to present the study of impact-induced damage propagation in woven composite structures subjected to C-C fatigue loading, utilizing GW and EMI to characterize and monitor delamination progression. This study seeks to improve the understanding of delamination severity through the perspective of GW and EMI based SHM. The effectiveness of GW and EMI techniques investigated by analyzing DIs obtained via signal processing. Furthermore, as DIs sensitive to structural degradation contribute to accurate RUL prognosis, the prognostic performance is further analyzed under prognostic metrics section.

## 4.2 Methodology

### 4.2.1 EMI-Damage Indicator

The deviation between the two spectra of EMI occurs in terms of magnitude and shift in resonance peak. Eqs (5-1) - (5-3) demonstrates the DIs that are used to quantify the variation between the admittance values at different fatigue loading cycle; DI 1 indicates the RMS of Cycle 0 and later cycles; DI 2 windowed RMS considers the limited segment from peak to closest minima where first resonance occurs; DI 3 calculates the resonant shifts through the cycles. **Figure 4.1** shows the admittance signal measured by six PZTs at two fatigue states for Sample 2: initial state and final state alongside measured delamination level.

$$EMI - DI 1_{N_{path}}(n) = \sqrt{\frac{\sum_{j=1}^{N_s} [Signal_n(j)] - \sum_{j=1}^N [Signal_{n=1}(j)]^2}{\sum_{j=1}^N [Signal_{n=1}(j)]^2}}, n = 1, \dots, N_{cycle\ steps} \quad (4-1)$$

$$EMI - DI 2_{N_{path}}(n) = \sqrt{\frac{\sum_{j=1}^{N_{swindow}} [Signal_n(j) - Signal_{n=1}(j)]^2}{\sum_{j=1}^{N_{swindow}} Signal_{n=1}^2(j)}}, n = 1, \dots, N_{cycle\ steps} \quad (4-2)$$

$$EMI - DI 3_{N_{path}}(n) = \frac{peak(Signal_{n=1}(window)) - peak(Signal_n(window))}{peak(Signal_{n=1}(window))}, n = 1, \dots, N_{cycle\ steps} \quad (4-3)$$

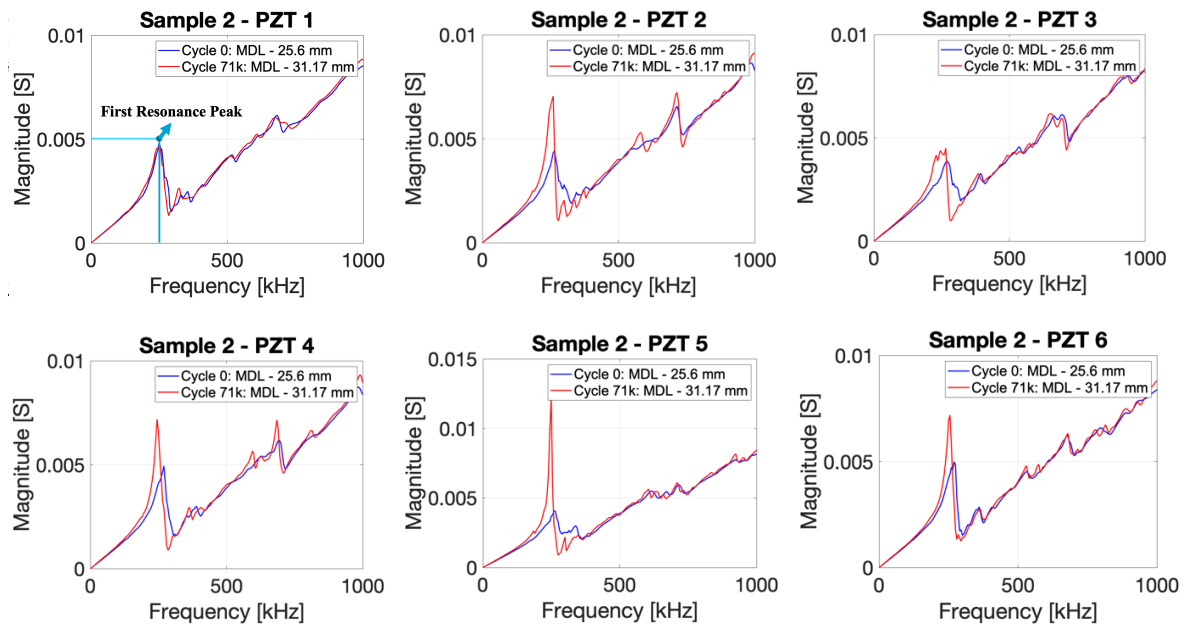


Figure 4.1. Initial and final state comparison for 6 PZTs of Sample 2.

### 4.2.2 Guided Wave Damage Indicators

GW-DIs are obtained through signal processing techniques to identify portions of the GW signal that are particularly sensitive to delamination. GW-DIs are extracted in both the time-domain through HT to obtain signal envelope from the analytical presentation of the signal and in the time-frequency domain via the CWT method [114]. A mode-independent approach is conducted in this work with the motivation to derive the information that can be obtained from the rest of the GW signal, potentially from mixed and higher GW modes. In that sense, after the pre-processing step, signal processing and DI extraction process is conducted with following procedures:

- HT is used to obtain signal envelopes from residual GW signal that allows for the calculation of the signal energy in desired time interval given in Eqs (4-4) - (4-6). A time-window is assigned with different length for each excitation signal resulting in a longer time window for a lower frequency of 100 kHz and a shorter one for 180 kHz. These intervals are 0-5 $\mu$ s; 0-4.5 $\mu$ s; 0-4 $\mu$ s; 0-3.5 $\mu$ s; 0-3.0 $\mu$ s. **Figure 4.2** shows the original and processed GW signals with envelope presentations.

$$H(t) = \frac{1}{\pi} \int_{-\infty}^{+\infty} \frac{x(\tau)}{t-\tau} d\tau \quad (4-4)$$

$$z(t) = x(t) + iH(t) \quad (4-5)$$

$$DI 1_{f_{exc}, N_{path}}(n) = \frac{[\sum_t^{T_{window}} HT(t)]_n}{[\sum_t^{T_{window}} HT(t)]_{n=1}} \quad n = 1, \dots, N_{cycle\ steps} \quad (4-6)$$

- CWT has been applied to represent the signal in the time-frequency domain, which allows to measure energy in segments of the signal which has been achieved via windowed average power calculation (WAP) where the related equations are given in Equations (4-7) - (4-11). In CWT analyses, wavelets, which are localized functions or waveforms, are employed to analyze different signal segments at various scales [115]. The wavelet function is denoted as  $\Psi$ , and the continuous CWT coefficients as CWT (a, b). When a signal segment matches the form or pattern of the wavelet, the resulting wavelet coefficients reach their maximum value. The Morlet function has been utilized as the wavelet in this CWT analysis [116]. The Morlet function consists of a sinusoidal wave enveloped by a Gaussian and closely resembles the form of a tone burst signal. Due to this resemblance in waveform shape, the Morlet wavelet is more effective at matching the characteristics of the tone burst signal compared to other types of wavelets, which consequently may result in improved signal decomposition and analysis, allowing for the essential features of the signal to be captured with minimal distortion [117].

$$CWT(a, b) = \int \psi\left(\frac{t-b}{a}\right) x(t) dt \quad (4-7)$$

$$x(t) = |CWT(a, b)| \quad (4-8)$$

$$AP(t) = \frac{\left(\sqrt{\sum_{j=1}^n x(t)_j^2}\right)^2}{M} = \frac{\sum_{j=1}^n x(t)_j^2}{M} \quad (4-9)$$

$$DI 2_{f_{exc}, N_{path}}(n) = WAP(t) = \frac{[\sum_t^{T_{window}} AP(t)]_n}{[\sum_t^{T_{window}} AP(t)]_{n=1}} \quad n = 1, \dots, N_{cycle\ steps} \quad (4-10)$$

$$DI 3_{f_{exc}, N_{path}}(n) = \frac{[\sum_t^{total} AP(t)]_n}{[\sum_t^{total} AP(t)]_{n=1}} \quad n = 1, \dots, N_{cycle\ steps} \quad (4-11)$$

$\Psi(t)$  is the wavelet function, and CWT (a, b) are the continuous CWT coefficients. In **Figure 4.2**, the time-domain representation of Sample 2 is shown at a healthy state and **Figure 4.3** impacted state at all given excitation frequencies. In order to detect the delamination-sensitive indicators, DI 2 and DI 3 are extracted from WAP, which is derived from the time-frequency domain estimated by CWT. The time window is selected based on highest amplitude component the final residue signal, aiming to demonstrate the higher deviation in the damage-sensitive wave package. After determining the time scale, the total energy change is estimated in this interval to obtain DI 2, named windowed averaged power (WAP). DI 3 calculates the total power change in the same spectrum, named (AP), that accounts for all spectrums. This spectrum can be seen in **Figure 4.4** that presents three different cycle step for Sample 2 with from three different paths.

- The coherence of the signal all through the growing cycles is evaluated with the cross-correlation between the signals in the time domain with the following equations:

$$(f \star g)[n] = \sum_{m=-\infty}^{\infty} f[m] \cdot g[m + n] \quad (4-12)$$

$$DI 4_{f_{exc}, N_{PZT}} = \max(\text{corr} [x(t - \delta)_n, x(t)_{n=1}]^{-1}), \quad n = 1, \dots, N_{cycle\ steps} \quad (4-13)$$

the term *corr* denotes the correlation coefficient function, and  $-\delta$  indicates the shift of the current signal.

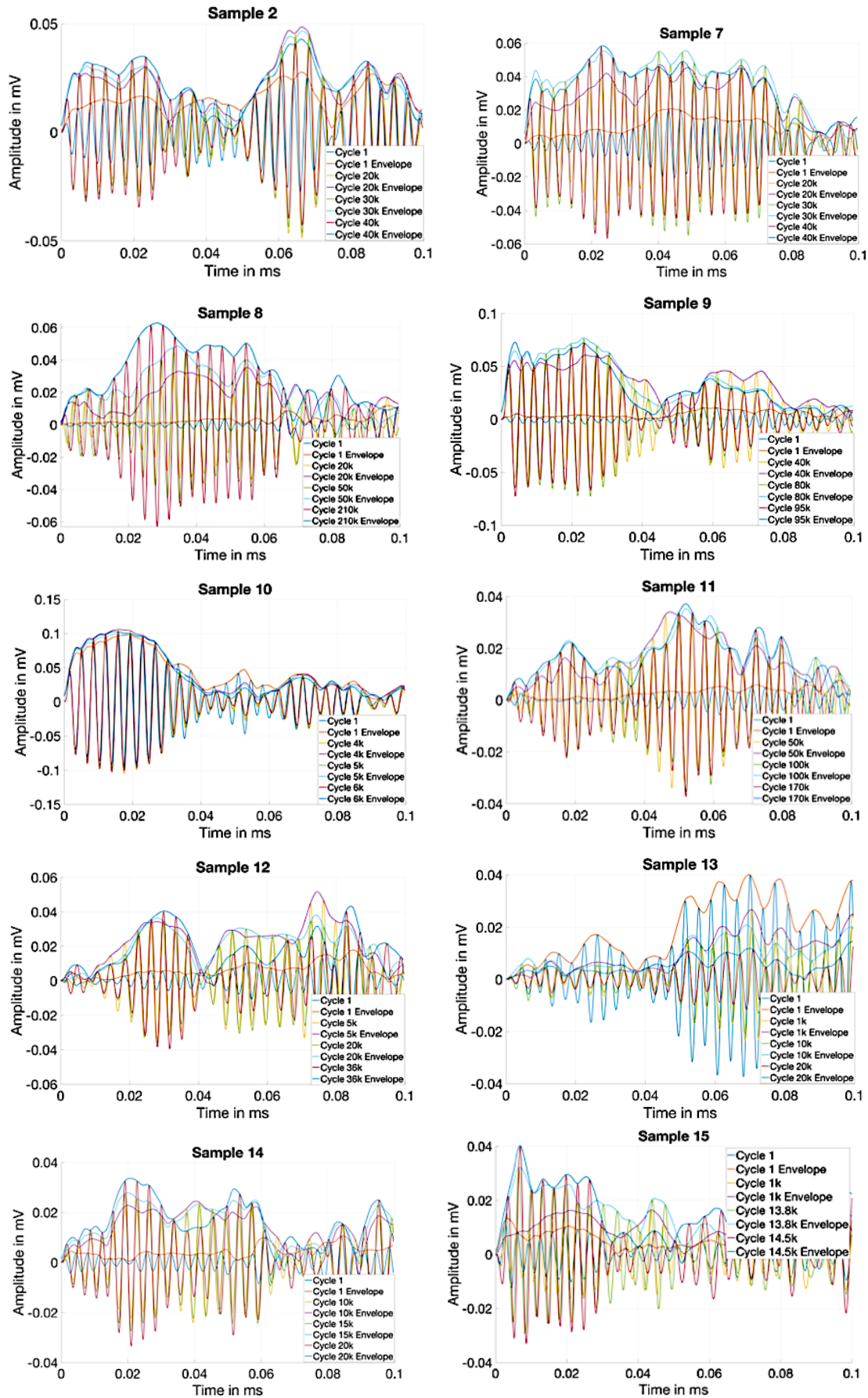


Figure 4.2. Envelope representation of GW signals from the path no 3, 180 kHz center frequency excitation signal.

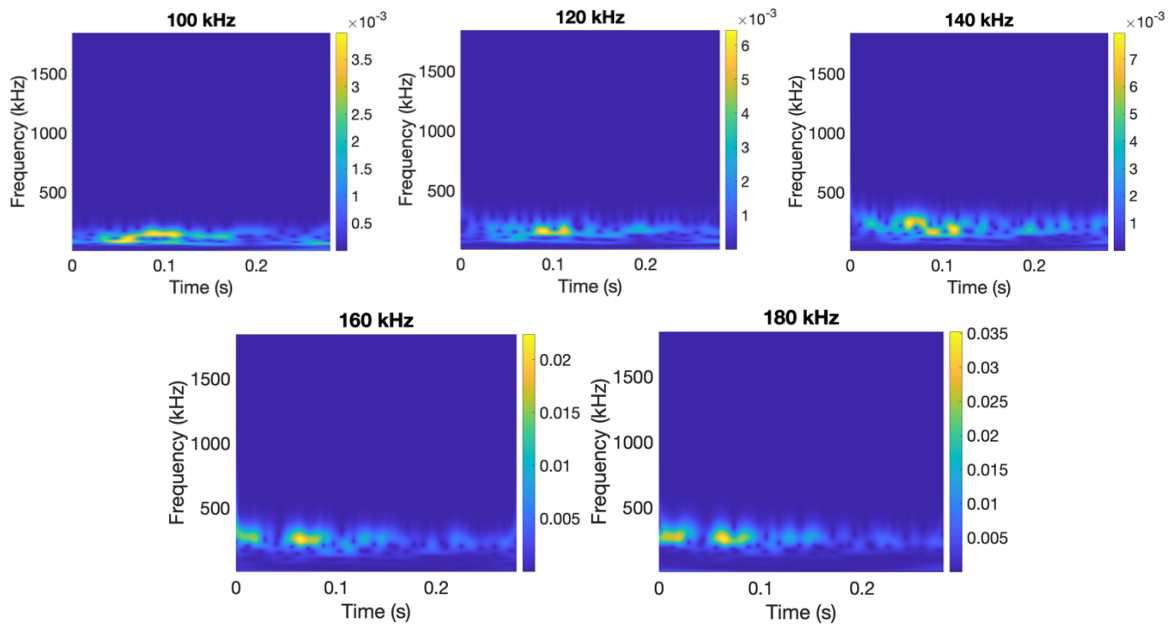


Figure 4.3. GW signals CWT representation at each excitation frequency from the path no 3 in final delamination state of Sample 2.

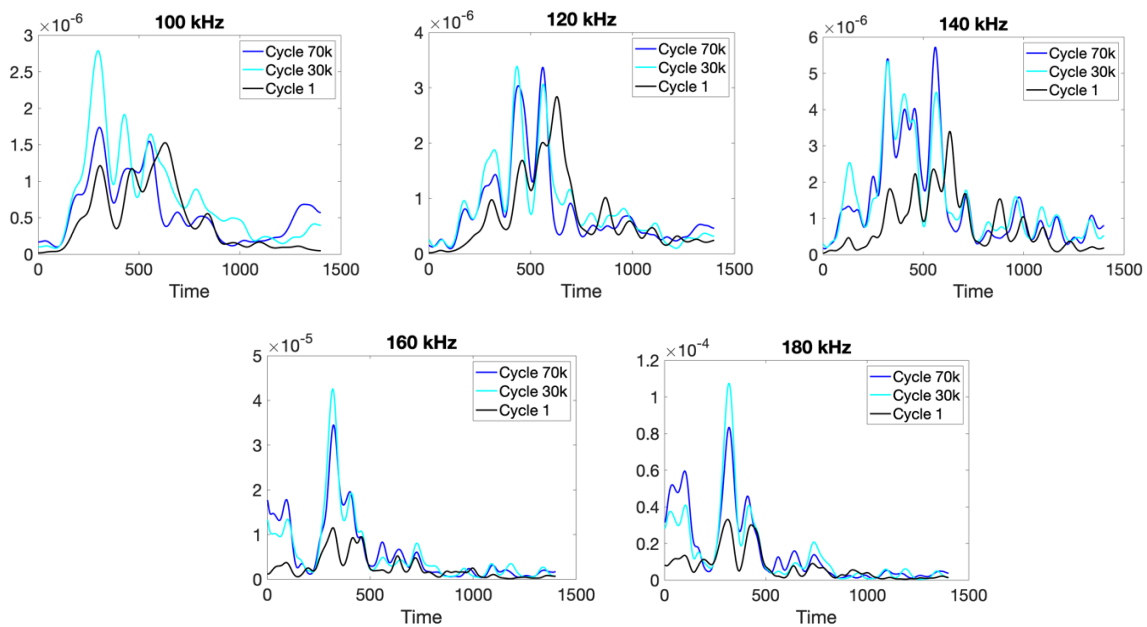


Figure 4.4. Signal average power (AP) calculated from the path no 3 of Sample 2.

### 4.2.3 Global DIs

After the DIs are obtained through the processes of extracting DI-1, DI-2, DI-3, and DI-4 for GW and DI-1, DI-2, and DI-3 for EMI signals, additional steps are undertaken to derive DIs that globally represent the damage state for each sensor in the network. **Figure 4.5** displays the main elements of the methodology for achieving global DIs. For GWs, a total of 18 paths is considered, as the system operates in a pitch-catch mode, while 6 PZT sensors provide data for EMI signals. Data from all PZT sensors in the network are combined with equal weighting to generate a single global DI for each cycle-step, while ensuring that the contribution of more sensitive paths is preserved. In Equation 4-14 and 4-15, sensor-based fusion step is given for  $x$  represents DI value at 1-cycle/time step. Once the DIs are calculated, a normalization process is applied.

$$EMI DI_{DI_{no}}(n) = \frac{\sum_{N_{path}=1}^{N_{total path}} (x_{N_{path}})}{N_{total path}}; DI_{no} = 1, 2, 3; n = 1, \dots N_{cycle steps} \quad (4-14)$$

$$GW DI_{DI_{no}, f_{exc}} = \frac{\sum_{N_{path}=1}^{N_{total path}} (x) N_{path}}{N_{total path}};$$

$$DI_{no} = 1, 2, 3, 4; f_{exc} = \{100, 120, 140, 160, 180 \text{ kHz}\}; n = 1, \dots N_{cycle steps} \quad (4-15)$$

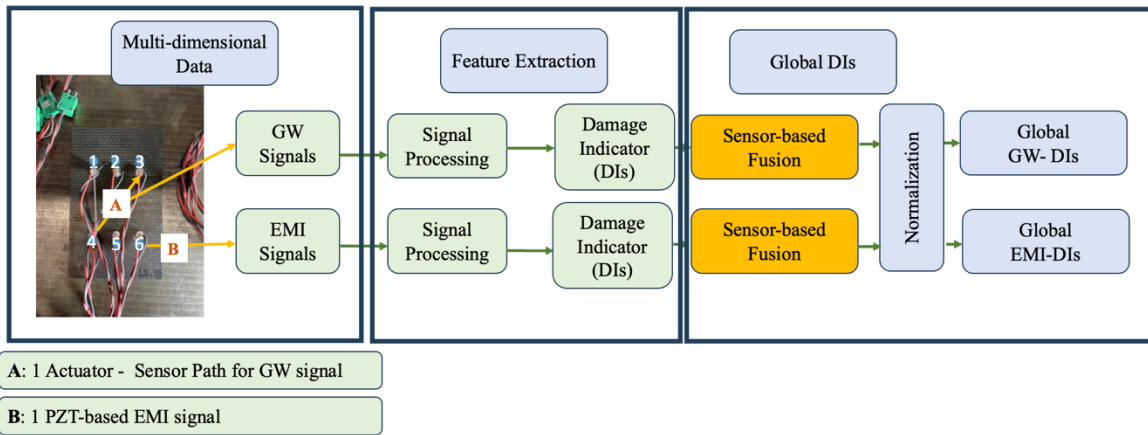


Figure 4.5. Methodological framework for global GW-DIs and EMI-DIs.

## 4.3 EMI & GW DIs for Progressive Delamination Monitoring

EMI-DIs are presented in **Figure 4.6**, and their accuracy to capture delamination growth behavior is shown. In the figures, each normalized-DI is represented with its corresponding normalized-MDL. It should be noted that no interpolated data between cycle steps has been used in the analysis of DIs and MDL. However, in cases of sensor malfunction, missing data has been replaced with the average of the nearest neighboring cycle steps to ensure continuity and maintain consistency in the dataset. It can be seen from the results that proposed DIs are not indicating the same behavior, yet in cases of Sample 7, 9, 10, 13 and 15 there is a continuous degradation. Sample 11 and Sample 8 show a constant state of delamination even some fluctuations exist it seems like a steady state behavior confirms their MDL. Samples 8 and 11 MDL have a limited representation after the normalization, as the earlier stages are shown at zero level. Note that no quantifiable change occurred during this period, yet impact damage exists as all the samples in the dataset. In addition to that, the load increased incrementally for Sample 11 after the 120k cycle. As so, Sample 8 and Sample 11 are unique cases, as there was no captured variation via c-scan until a specific cycle for these two samples; EMI-DIs also show an accumulation, and no increasing trend is shown in their DIs.

Samples 12 and 13 reflect the given calculated degradation trend. However, it should be remembered that their delamination quantification was not possible, so a linear trend has been considered for those samples' degradation. EMI-DIs are acting with a limited performance for Sample 14, especially in the later cycles. Eventually, the three samples, Sample 12, 13, and 14, have limited data acquisition steps that provide less to process than other samples in the dataset. Sample 15 also presents a good consistency in the sense of DI 1 and DI 2 while the DI 3 display opposite trend in its last cycle. One remarkable result belongs to Sample 7; all three DIs show a trend with a high coherence with its MDL. The damage growth case for Sample 7 was initially accelerated and may exhibit dominated delamination growth, which was captured by EMI measurements. On the other hand, despite that the environmental conditions may have some effects unless they are measured and mitigated, tested samples have shown promising capability to capture the delamination growth trend with EMI-DIs. One of the limited results is Sample 2 that its DIs deviate significantly specially for DI 1 and DI 2 and DI 3 indicates a very different trend than MDL. Here, the explanation for this behavior may indicate the slow growth trend of Sample 2 was not able to be captured well by EMI, even for DI 3, that implies a more severe growth, and it has a miss representation considering that the damage degradation will always follow a growing trend as no healing or repair is considered in this work.

GW-DIs are presented for their five excitation frequencies with the normalized MDL values **Figure 4.7** for Sample 2. One aspect that can be observed is that DI behaviors are in correlation under the same frequency group, and their attribute changes as the excitation frequency that induces the GW signals increases can be seen in **Figure 4.7**. It can be seen in the results that the GW-DIs of Sample 2 are more sensitive to delamination as their trend converges to MDL for 160 kHz and 180 kHz. One other common aspect in all the results is the initial growth indication at the first cycles and in the lower frequency results its presence is more dominant. On the other hand, in higher frequencies, this situation is less effective and nearly disappears for some DIs. In more detail, in **Figure 4.7**, the sensitivity to early fatigue effects is getting less dominant for Sample 2 as the GW signals are induced with higher excitation signal start to become more sensitive to changes originated to the delamination based on proposed feature-extraction methodology.

GW-DIs are shown with the normalized MDL values for each sample in **Figure 4.8**, presenting the results for all samples from one-selected frequency. As each frequency contains 4-DIs, it makes 20-DIs to investigate at the end. Therefore, most accurate results are selected and presented. Based on the results, Sample 8 and Sample 11 present a steady-state behavior that confirms with their EMI-DIs. Sample 8 failed in the first 7,000 cycles after the 210k cycles once the load was increased with 5kN, which did not allow for c-scan measurement before its failure. Therefore, that may prove that the increase in the severity that is observed in GW-DIs for Sample 8 may indicate the variation in the delamination even though it is not visible in MDL. One another point is that, regarding Sample 2 and Sample 9, they undergo a period where the delamination growth rate is smaller compared to its growth in later cycles. Therefore, the influence in GW signals due to the other damages may be more apparent in cases like Sample 2 and 9 since delamination growth was less dominant in early fatigue life. On the other hand, Sample 10 experiences higher loads in its early fatigue life, and its delamination is growing faster with a more significant growth rate. Despite Sample 7 did not experience higher load levels, the delamination was presenting a fast growth for this sample as well. In the case of Sample 7 and 10, the contribution of other damage types, such as matrix cracks, may be less effective on GW signals since delamination was the dominant mode from the beginning. In the case of Sample 9, the MDL quantifies the growth in the last layer precisely in later cycles and GW-DIs and EMI-DIs imply slower degradation comparatively to its earlier cycles.

It is important to note that MDL is only a measure of maximum length, and the way it quantifies the delamination's severity may be limited. However, despite this fact, given results are in good agreement with the measured trend of delamination growth in general. EMI-DIs and GW-DIs are in correlation with each other for the sample numbers 7, 8, 9, 10, 11 and 15 and results tend to indicate more accelerated damage growth in most of the cases for both EMI and GW based DIs compared to MDL. On the other hand,

GW-DIs seems more sensitive compared to EMI-DIs when the quantified variation in delamination is smaller, such as in the case of Sample 2. In addition, EMI-DIs does not introduce an accelerated sudden growth in the early fatigue cycles unsimilar to GW-DIs, demonstrate this effect significantly in the lower frequency results.

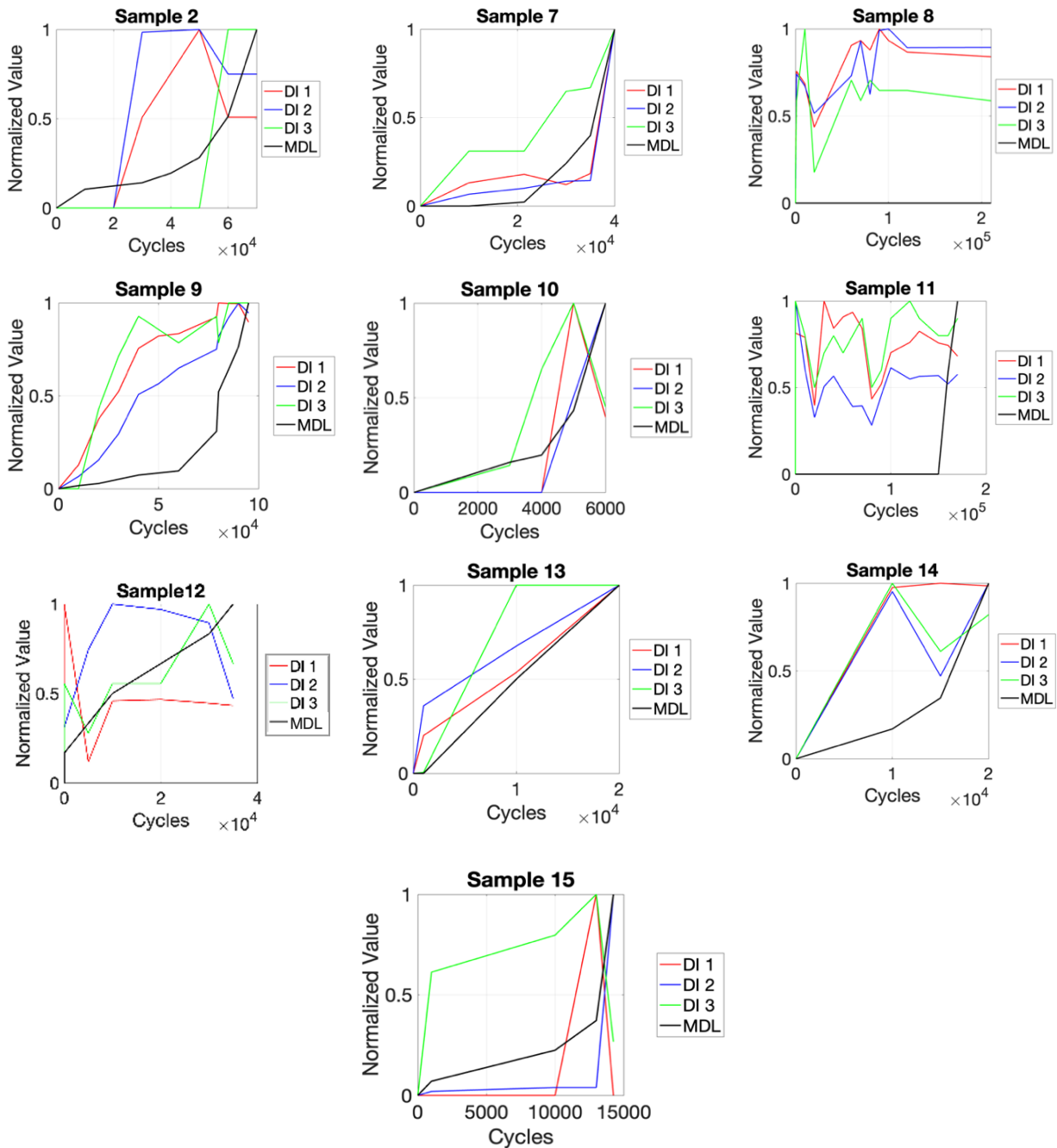
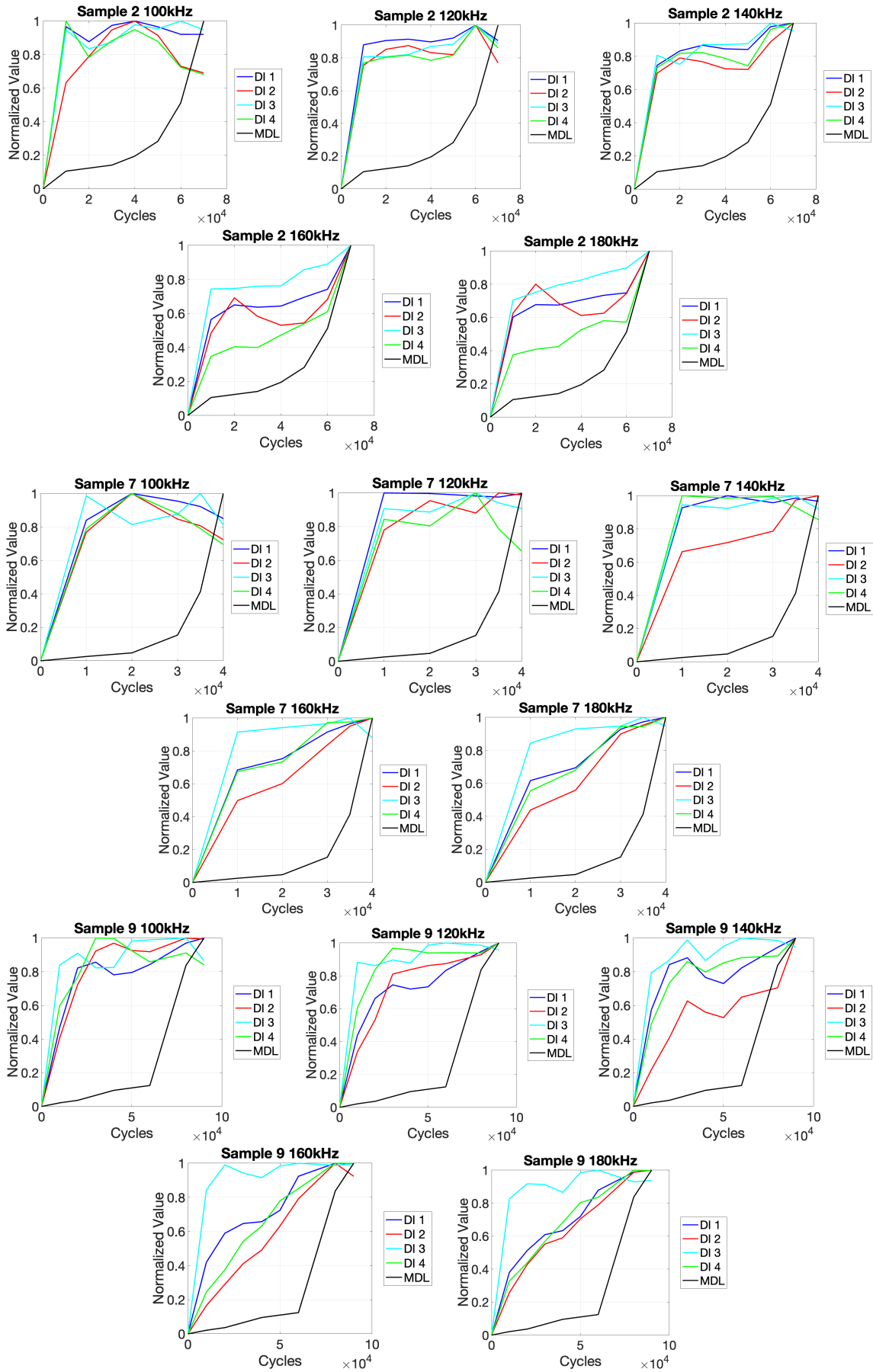
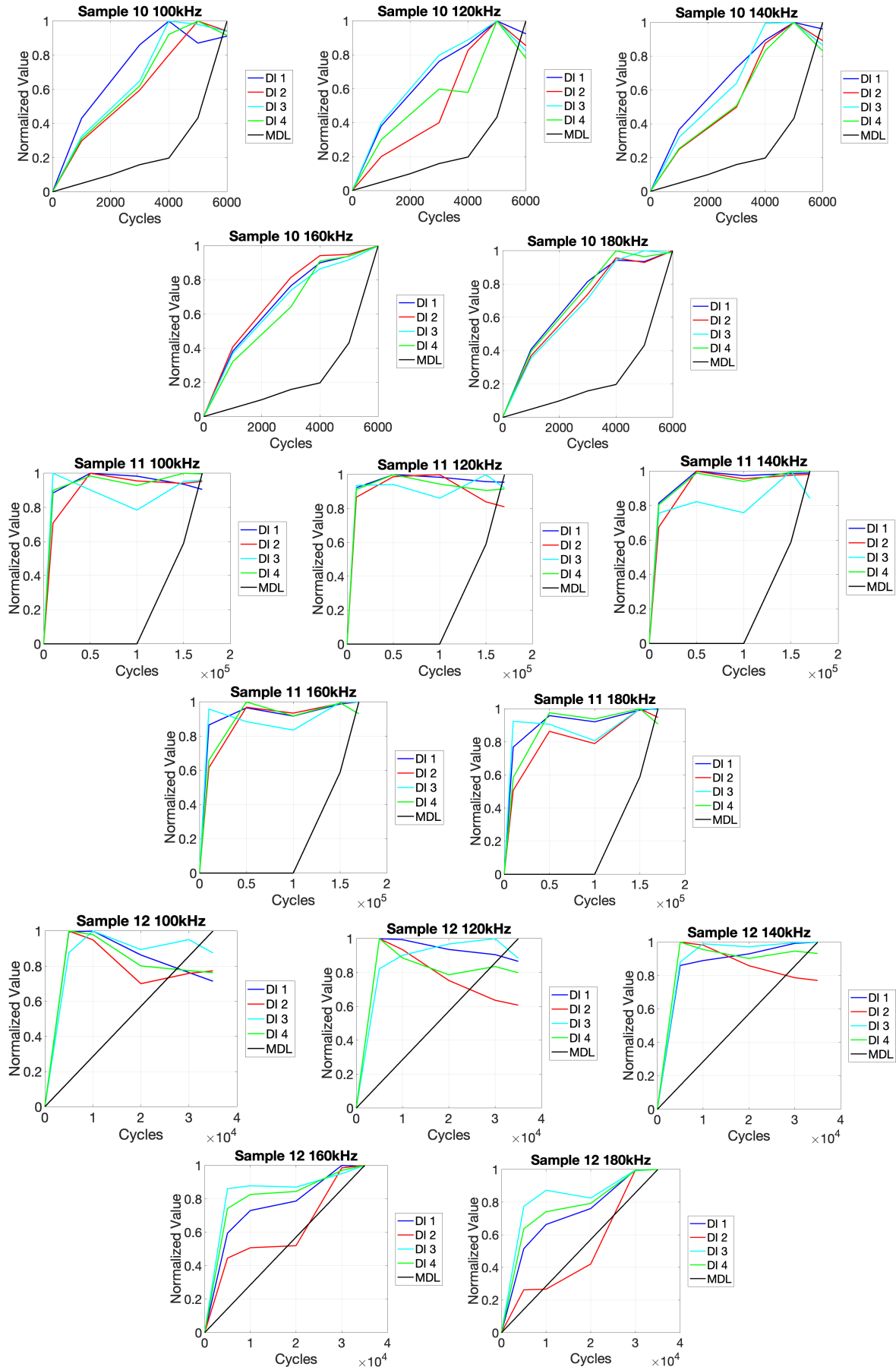


Figure 4.6. EMI-DIs and delamination growth for all samples in set.





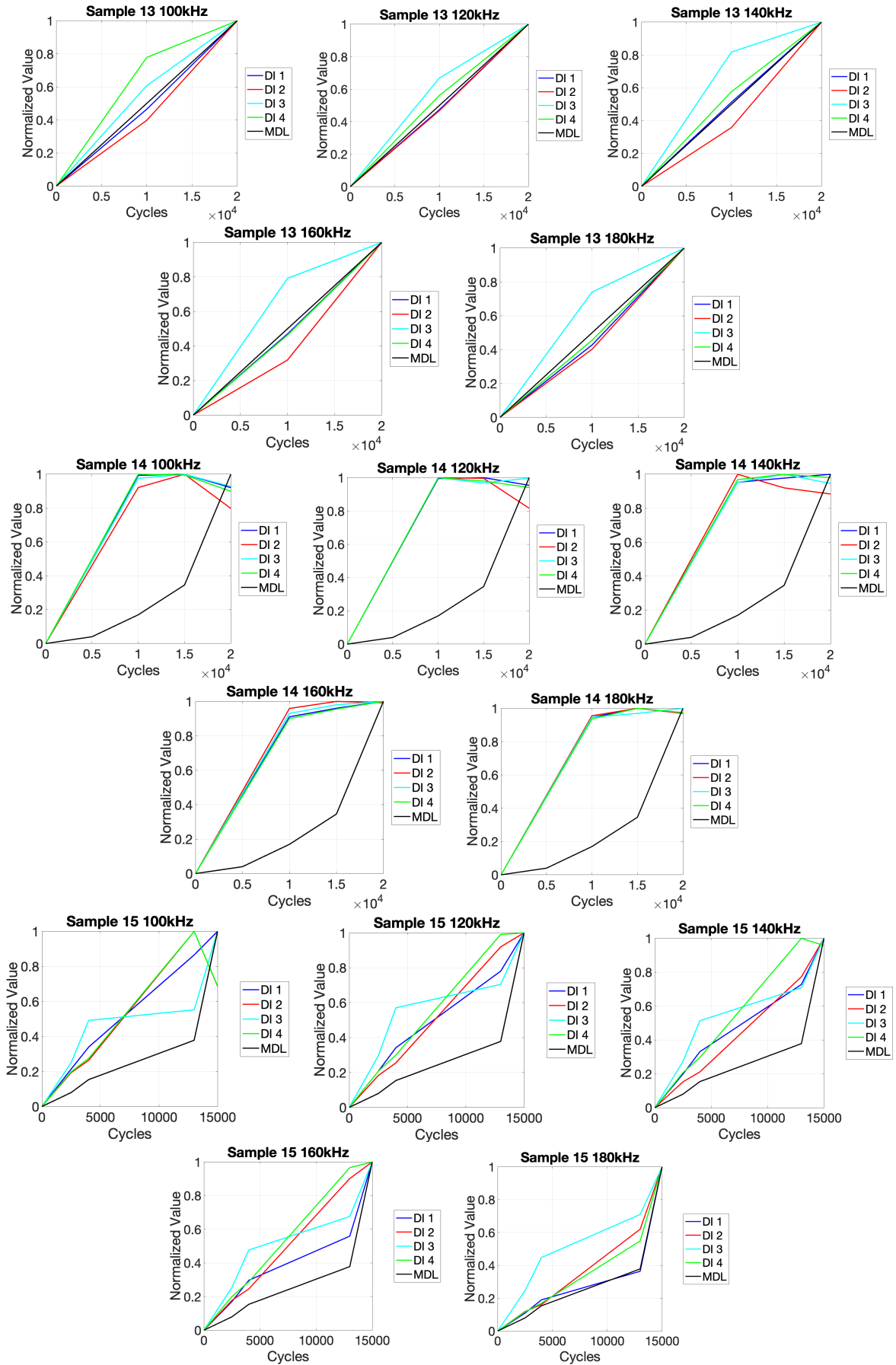


Figure 4.7. GW-DIs for each excitation frequencies of all samples.

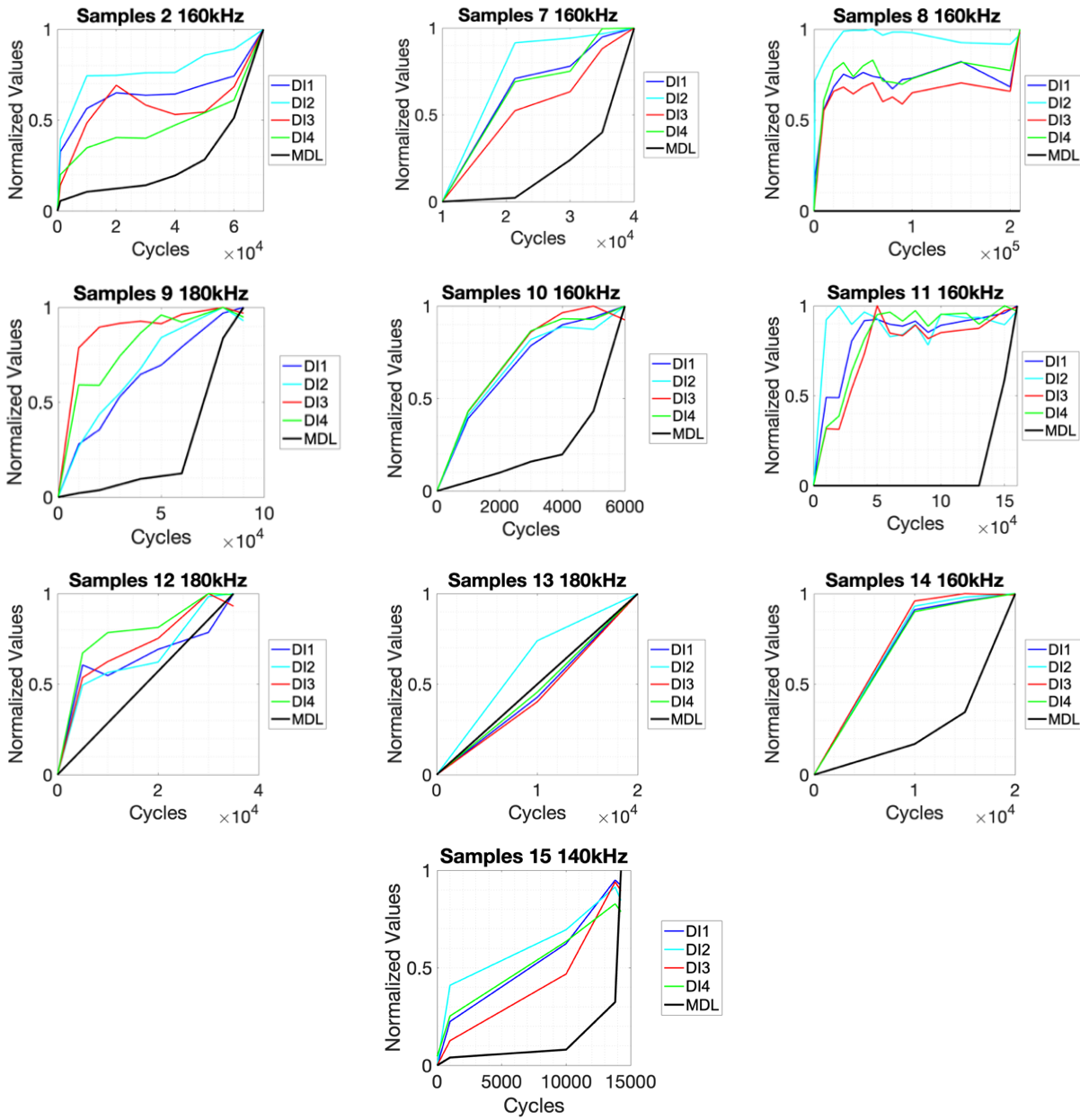


Figure 4.8. GW- DIs and delamination growth for all samples with highest score  $f_{exc}$ .

#### 4.4 Prognostic Metrics

From a prognostic perspective, any DI is expected to exhibit behavior reflecting continuous structural degradation over time, given that no maintenance activities or self-healing processes take place. Thus, as damage accumulates within the structure, the associated DIs derived from GW and EMI methods should show a progressive increase. This behavior is critical for accurate RUL predictions, providing a measurable and interpretable signal of the structure's ongoing deterioration. A monotonicity (Mo) metric is often employed to quantify this expected trend [118], [119]. Additionally, the correlation metric can assess the similarity between DIs and observed damage degradation trends. This criterion can measure the degree to which the DIs reflect the underlying damage mechanisms as they evolve by measuring the DI correlation with measured delamination length. High correlation signifies that a DI tracks damage degradation and may enable better predictive modeling and facilitate more reliable RUL estimation. Ratings for the two metrics, Mo and Corr, range from 0 to 1, with a score of 1 denoting ideal DI performance. Considering these criteria, the following formulations for the Mo and Corr metrics are used:

$$\text{Mo} = \frac{1}{M} \sum_{j=1}^M \left| \sum_{k=1}^{N_j-1} \frac{\text{sgn}(x_j(k+1) - x_j(k))}{N_j-1} \right| \quad (4-16)$$

$$\text{Corr} = \left| \frac{\text{cov}(x_j, D_j)}{\sigma_{x_j} \sigma_{D_j}} \right|; \quad j = 1, 2, \dots, M \quad (4-17)$$

$$\text{Fitness} = a \cdot \text{Mo}_{DI} + b \cdot \text{Corr}_{DI} \quad (4-18)$$

The fitness metric for DIs ranges from 0 to 2, assuming that the control constants a, and b are each equal to 1. The subscript DI refers to “damage indicator” and damage indicator from a particular excitation frequency that GW-DIs belong.

In **Figure 4.9**, the Mo performance of EMI- DIs and GW-DIs is presented for each sample. In **Figure 4.9** a and b, a similar trend is observed for GW-DIs and EMI-DIs, where both monotonic and correlation metrics do not show a consistent increase or decrease across different DIs and samples. However, GW-DIs generate higher performance metrics in overall for each GW-DI, whereas the metrics of EMI-DIs exhibit larger variability, making them less stable in achieving higher scores. In **Figure 4.10** the performance of DIs vary for each sample and EMI-DI 1 presents slightly higher values for most of the samples. The average values of each PZT for EMI-DIs indicate that PZT 6 was more sensitive to degradation in terms of its fitness value specifically for DI 2. In **Figure 4.11**, like EMI-DIs, the fitness of GW-DIs is not constantly increasing or decreasing from one DI to another while average values show that as the frequency increases the fitness values raise slightly as well. However, as the per-sample results imply that this does not hold in each case, all DIs from all frequencies are assigned as one independent feature in all the learning models in the utilization of GWs.

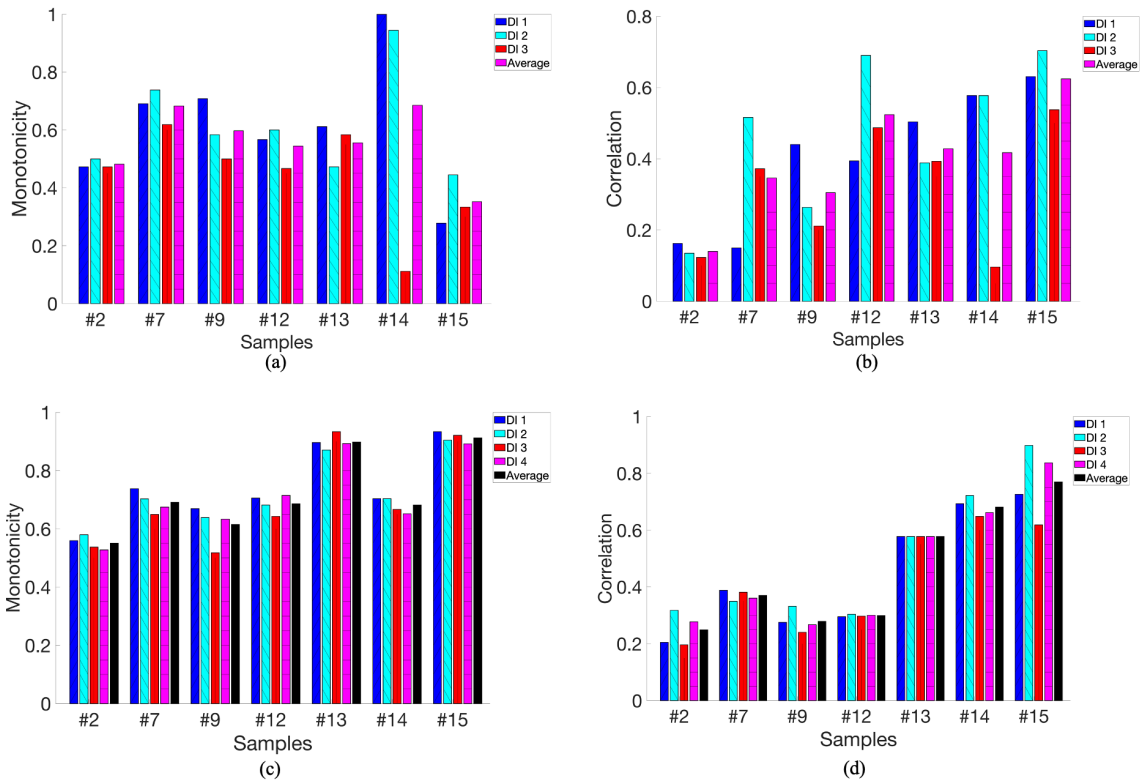


Figure 4.9. Monotonicity metric for (a) EMI-DIs and (c) GW-DIs; Correlation metric for (b) EMI-DIs and (d) GW-DIs.

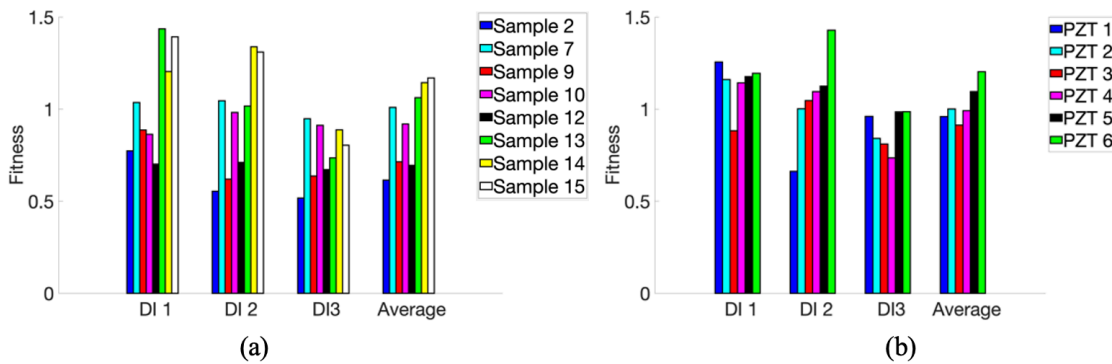


Figure 4.10. Fitness for a) EMI-DIs per sample, b) EMI-DIs averaging all samples for each PZT.

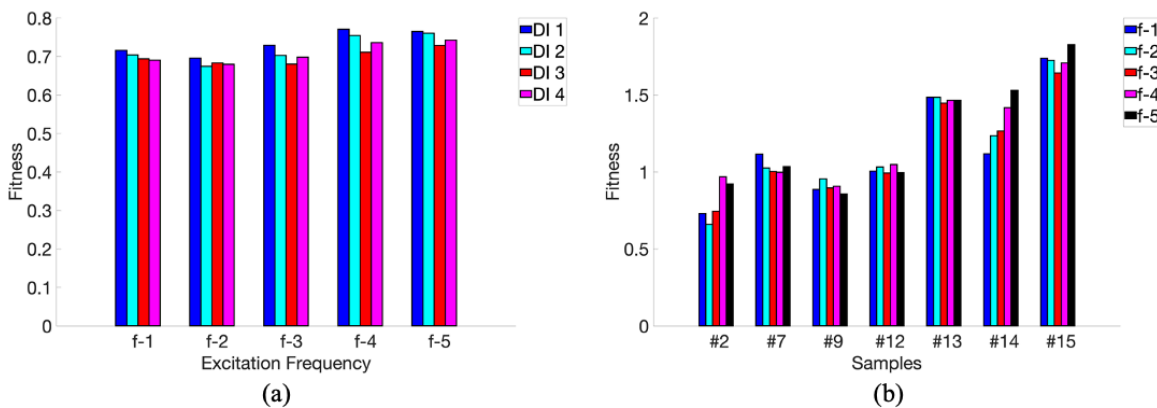


Figure 4.11. Fitness for (a) GW-DIs averaged over all samples and (b) GW-DIs averaged over each DIs.

## 4.5 Conclusion

This chapter provides a comprehensive investigation into impact-induced damage propagation in woven composite structures subjected to compressive fatigue loading, with a focus on characterizing and monitoring delamination progression using GW and EMI techniques. The study enhances the understanding of delamination severity by leveraging GW and EMI-based SHM approaches, while also evaluating the effectiveness of these techniques through detailed analysis of DIs obtained via signal processing. Furthermore, the prognostic capabilities of these DIs, which are sensitive to structural degradation, are critically assessed through established prognostic metrics, offering valuable insights into their reliability for accurate RUL prediction.

Considering the proposed framework, two main challenges have been aimed to be answered; in the case of advanced signal processing techniques, it requires effort to extract damage-related information because of the nature of the delamination that propagates through the composite's layer in a complex way. Even though any mode separation through frequency selection and phase velocity analysis is conducted in this study, the sensitivity of proposed GW-DIs to delamination progress is observed in estimated DIs with their discussed limitations. It is shown that EMI and GW-based DIs are correlated in terms of their sensitivity to measured delamination growth, as both methods indicate monotonic degradation phenomena for delamination when it is growing or when it is accumulating. Unique characteristics of both techniques improve the reliability of the results, as the integrated methodology allows for detailed understanding by capturing the variations in DIs for different loading cases, such as presented fast growth and slow growth delamination effects.

Besides, the number of excitation frequencies, the number of paths, and the number of DIs creates an abundance of information, but comparing their performance with the damage state is problematic in the way that they are fused, and that delamination state is quantified. As stated earlier, MDL considers the growth rate to be measured by the maximum length of the delamination. Thus, the correlation between the DIs and MDL is looked at in terms of their trend correlation, as the aim of the search is to investigate the sensitivity of the GWs and EMIs-based DIs to variations in the delamination trend. However, a better description or labelling of the damage severity may enable a better comparison and accuracy analyses. Secondly, as there are some specific cases that EMI-DIs or GW-DIs outperform the other, a global representation of DIs may require more sophisticated fusion techniques that enable more accurate monitoring for the severity of delamination. Therefore, this chapter lays the foundation for subsequent prognostic methodologies by establishing the integration of GW and EMI techniques into the prognostic framework. The insights gained from analyzing the effectiveness of these techniques in monitoring damage progression and evaluating the prognostic performance of the associated DIs will serve as a critical reference for developing and refining advanced prognostic models in the chapters that follow.

## **5 RUL Prognosis via Integration of Active Sensing SHM Methods: EMI & GW**

## 5.1 Introduction

This chapter introduces a comprehensive approach to RUL prognosis by leveraging DIs derived from both GW and EMI signals. Given the variability in performance metrics observed across different DIs and excitation frequencies, it is challenging to pinpoint a single best DI or frequency for GW and EMI. To address this limitation, the study proposes a prognostic model that incorporates and learns from all available DIs, aiming for a more effective RUL estimation. Recognizing that EMI-DIs and GW-DIs may not consistently reflect the same degradation scenarios due to their inherent differences, a DNN model is employed to integrate GW-DIs and EMI-DIs together with a weighted averaged ensemble model (WAE). EMI- and GW-based global DIs are incorporated into the prognostic framework aiming to enhance the accuracy and reliability of RUL predictions as the proposed GW-EMI models aim to operate the most effective predictions from each DI. An evaluation of the DIs revealed that GW-DIs achieved better accuracy on average across all cycles compared to EMI-DIs. Both fusion models demonstrated strong accuracy for individual samples, with Fusion Model 1 (RUL-fus-1) showing a 12% improvement and Fusion Model 2 (RUL-fus-2) showing a 24% improvement across all cycles on average. Notably, Fusion Model 2 exhibited the lowest error in the final cycles, with a 48% improvement in accuracy compared to the least successful model, demonstrating its potential for more precise prognosis through the integration of GW-DIs and EMI-DIs.

## 5.2 Methodology

A MLP structure is designed as DNN model to achieve RUL regression task, as they are well-suited for tasks with high-dimensional inputs and nonlinear relationships. To explore the performance of EMI-DIs and GW-DIs, models are trained for each Global-DI, which results in two different hyperparameter tunings for each MLP model. Two fusion methodologies are proposed for further improvement to achieve a more robust prognostic. The WAE considers two RUL predictions obtained each prognostic model trained via GW-DIs and EMI-DIs. The second fusion methodology concatenates the outputs of each prognostic model and then inputs them into the fusion model, which is designed as another DNN architecture with independent hyperparameter tuning and learning steps. The schematic of the proposed RUL prognostic is represented in **Figure 5-1**.

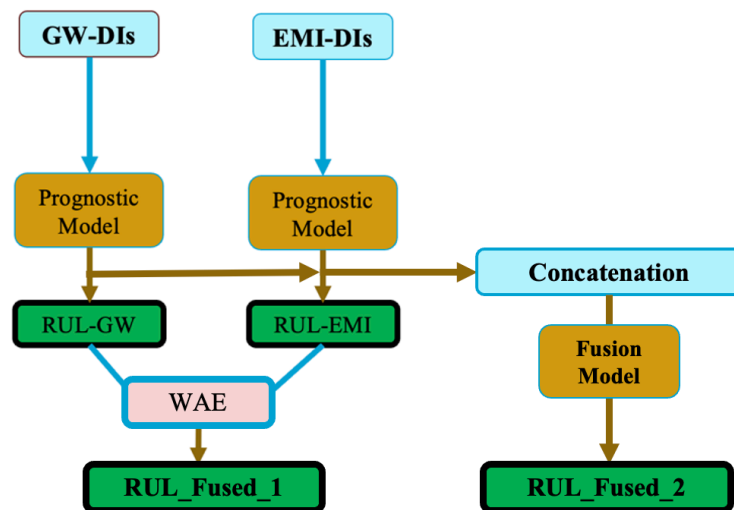


Figure 5.1. Schematic of proposed RUL prognostic.

### 5.2.1 Input Organization

The prognostic dataset for this study was created with samples 2, 7, 9, 12, 13, 14, and 15 by excluding samples 8 and 11 as their degradation has not been captured in terms of delamination propagation. Sample 10 is excluded because of its EoL, which negatively affect the prognostic criteria that consider the distribution of samples' end-of-life merit. **Figure 5.2** shows the input set preparation process. GW-DIs and EMI-DIs are passed from sensor fusion step to obtain global DIs. As the prognostic model aggregates data from all samples to create a generalized framework, a standardization process is applied to both GW-DIs and EMI-DIs. This step enhances the learning capability of the DNN models by ensuring consistency across the dataset, while preserving the influence of each sample's unique degradation information. Using interpolation, the intervals between cycle steps were equalized for both EMI and GW more details can be found in Table 3.1.

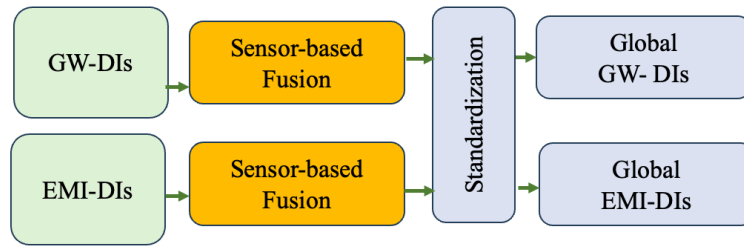


Figure 5.2. Input set preparation steps.

### 5.2.2 Model Architecture and Training-Testing

To explore the performance of EMI-DIs and GW-DIs, models are trained for each DI, which results in two different hyperparameter tunings for each learning model. Two fusion methodologies are proposed for further improvement to achieve a more robust prognostic. The weighted average ensemble (WAE) considers two final RUL predictions from each prognostic model trained and tested via GW-DIs and EMI-DIs. The second fusion methodology concatenates the outputs of each RUL prognostic model and then inputs them into the fusion model, which is designed as DNN architecture with independent hyperparameter tuning and learning steps.

Without explicit time dependence in its structure, the model is trained using input data formatted time-series. During the training phase, each iteration involves mapping an individual input value within the dataset to its corresponding RUL target. Training is conducted by sequentially feeding the model with the DI history of each sample within the training set. For testing, the model predicts RUL for each time step based on unseen data, effectively estimating RUL iteratively across the time horizon. **Figure 5.3** presents the complete framework for RUL prognostic with the proposed learning model. Two architectures are trained for EMI-DIs and GW-DIs inputs named M-EMI and M-GW. Input sets have  $t_{cyclesteps} \times N_{features}$ , M-EMI has an input dimension of  $56 \times 3$ , and M-GW has a dimension of  $56 \times 20$  that has been split for testing and validation purposes. Each dataset has six samples for training, and 1 sample is left for testing purposes. In that sense, Leave-one-out-cross-validation (LOOCV) is adopted into the framework that allows for evaluating the model's performance using data not previously introduced during training, thereby assessing the model's effectiveness in handling unseen data.

As a result, each sample was held out as a testing sample and was not included in the training phase. Finally, RUL predictions of seven samples are obtained. To account for potential missing data steps and maintain consistency, interpolation is applied to keep intervals constant. The inputs are standardized using z-score normalization (standardization) applied on each DI set separately and then fed into the M-EMI model through a 3-neuron input layer. In contrast, the M-GW model utilizes a 20-neuron input layer. Hyperparameters are optimized experimentally by monitoring the training loss, which is measured as the MSE value, using validation data. The validation data is randomly selected from the training set, with 20%

of the training data set aside for validation. The solution space for the given architecture is considered to be sufficiently converged, meaning that minor adjustments in the number of neurons do not significantly impact the model's accuracy. This suggests that the architecture is robust to small network configuration changes, indicating that the model's performance has reached an optimal or near-optimal state within the specified design parameters. The model utilizes a batch size of 2, meaning that the parameters are updated based on the loss function after processing each pair of consecutive time steps. Final hyperparameters are given in **Table 5.1**. Dropout regularization layers are applied after the first and second layers. To generate confidence bounds for the predictions, the model was re-initialized and re-trained ten times with random initial weights and biases, resulting in varied predictions each time. This approach demonstrated the stability of the proposed model by showing that predictions consistently fell within a specific range, confirming the model's robustness across different random initializations.

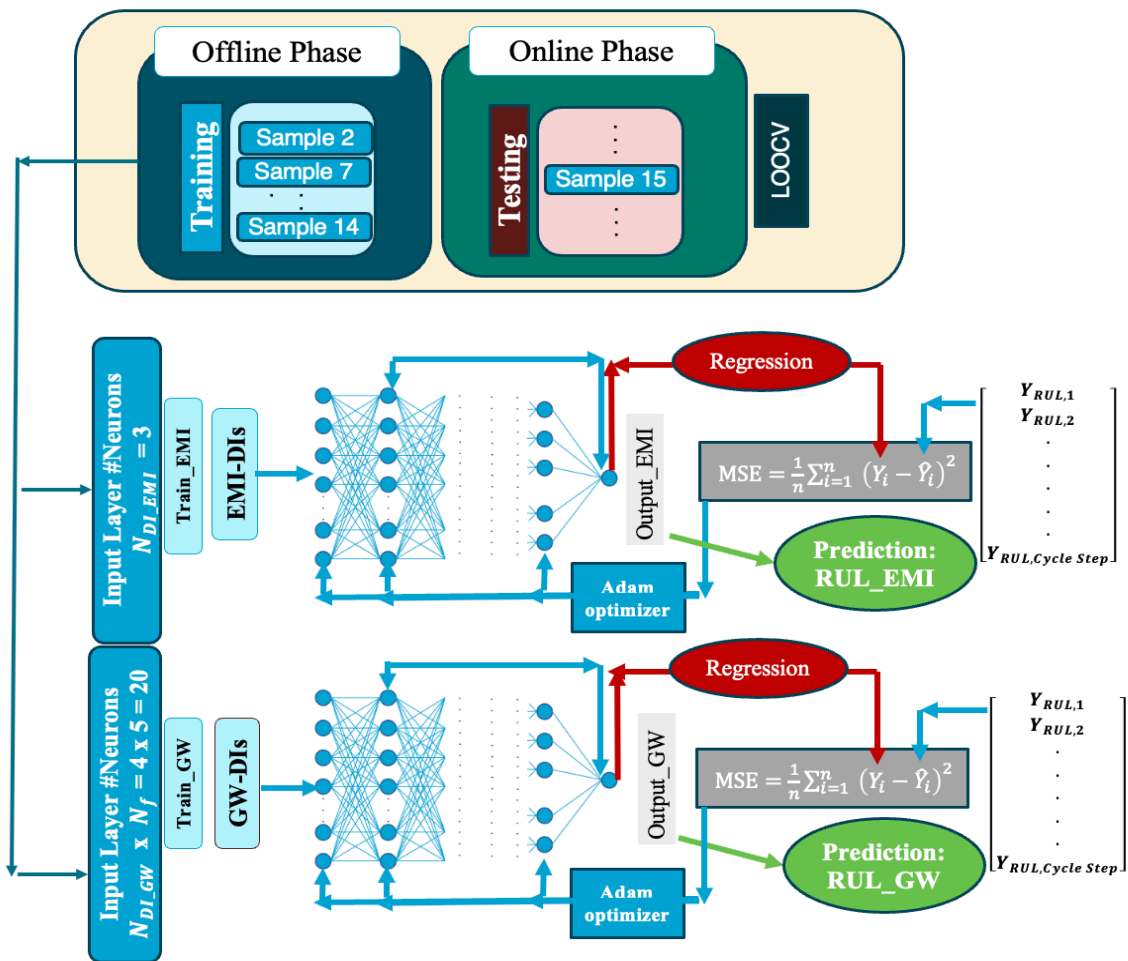


Figure 5.3. DNN scheme for RUL prognostic framework.

Table 5-1. Hyperparameters of proposed models M-EMI and M-GW.

Model	Number of Neurons										Initial Learning Rate	Batch Size
	Layer 1		Layer 2		Layer 3		Layer 4					
<i>M-EMI</i>	32	Dropout 0.2	ReLU	16	Dropout 0.2	ReLU	8	ReLU	1	Linear	0.01	2
<i>M-GW</i>	64			32			8		1		0.01	2

### 5.2.3 Fusion Methodology

As can be seen in **Figure 5.4**, two fusion approaches are proposed: WAE and DNN-fusion. WAE, shown as Fusion 1, is defined as follows:

$$f_{WAE} = \sum_{k=1}^K \bar{\omega}_k f_k; \bar{\omega}_k = \frac{\omega_k}{\sum_{k=1}^K \omega_k} \quad (5-1)$$

$$\omega_k^{MSE} = \frac{1}{MSE(Y_{RUL}, RUL^{k(E)})} = \frac{1}{\frac{1}{N_j} \sum_{i=1}^{N_j} (Y_j(t_i) - RUL_j^{k(E)}(t_i))^2} \quad (5-2)$$

$$\omega_k^{RMSE} = \frac{1}{RMSE(Y_{RUL}, RUL^{k(E)})} = \frac{1}{\sqrt{\left[ \frac{1}{N_j} \sum_{i=1}^{N_j} (Y_j(t_i) - RUL_j^{k(E)}(t_i))^2 \right]}} \quad (5-3)$$

where  $f_k$  represents the  $k^{\text{th}}$  individual model and  $\bar{\omega}_k$  is its normalized weight.  $\omega_k$  denotes the weight for the  $k^{\text{th}}$  individual base model. MSE, RMSE are calculated as error metrics to determine the weights. Simple averaging ensemble (SAE) is implemented by setting all  $\omega_k$  to one. The final output is selected based WAE output that has the minimum error with respect to target RUL value, denoted as “ $Y_{RUL}$ ”. RUL-fused-2 is obtained in the methodology shown in **Figure 5.4** as Fusion 2. A DNN model is constructed that is fed by the outputs of GW-based and EMI-based prognostic models as input, and it is trained to follow targets  $Y_{RUL}$ . Its hyperparameters are given in **Table 5.2**.

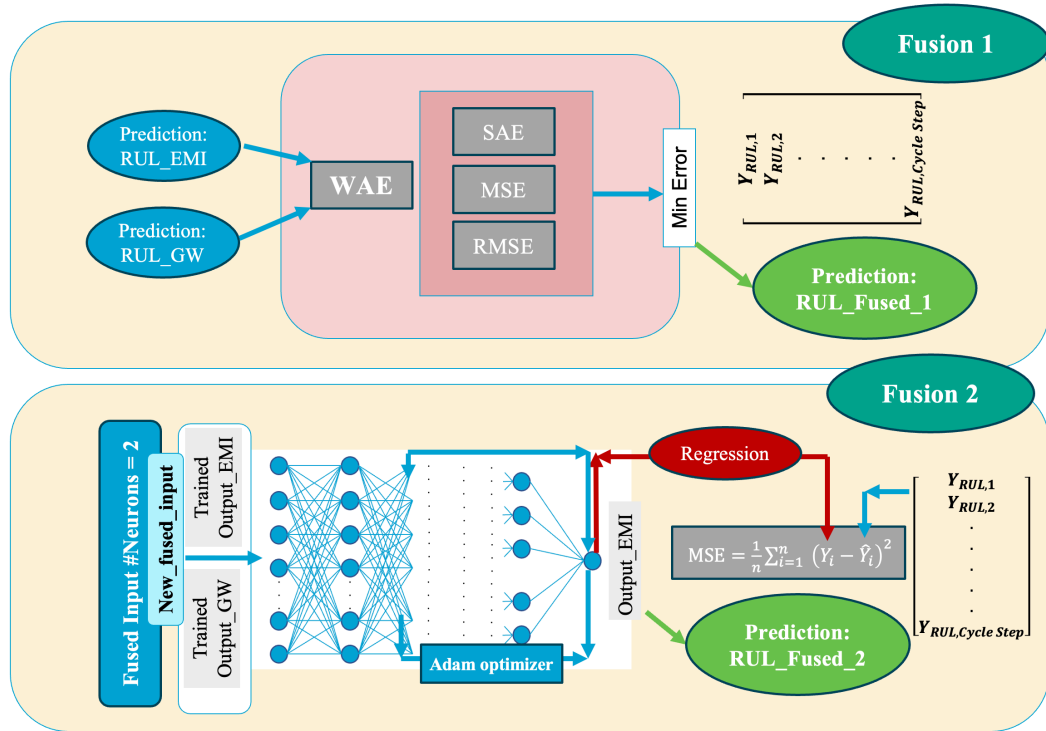


Figure 5.4. Proposed fusion methodologies to integrate RUL predictions obtained from both EMI-based and GW-based prognostic models. Fusion 1 represents the weighted average ensemble (WAE), and Fusion 2 has a deep learning basis.

Table 5-2. Hyperparameters of the model “M-fuse”.

Model	Number of Neurons										Initial Learning Rate	Batch Size
	Layer 1	Dropout 0.2	ReLU	Layer 2	Dropout 0.2	ReLU	Layer 3	ReLU	Layer 4	Linear		
<i>M-Fuse</i>	32	Dropout 0.2	ReLU	16	Dropout 0.2	ReLU	8	ReLU	1	Linear	0.01	1

### 5.3 Results

RUL prediction results are obtained as RUL-GW, RUL-EMI, RUL-fused-1; WAE-based Fusion 1, and RUL-fused-2; DNN-based Fusion 2. Errors of predictions are given by the metric of MAPE, while  $n$  is 10 indicates the number of total re-initializations.

RUL results are presented in **Figure 5.5** for seven tested samples that compare the accuracy of each input type. Among all tested samples, samples 7, 12 and 14 have the highest accuracy. The results show that the RUL accuracy differs for each input type in terms of accuracy. In **Figure 5.6**, error values are given showing the error occurred in RUL prediction for each cycle. It can be seen in the RUL prediction results that the model has a good performance in terms of its convergence throughout the cycle steps. For sample 12, RUL-EMI dominates the other three inputs with a higher accuracy through all cycles, yet the error occurred in the last cycle step shadows the overall performance. It should be noted that sample 12 has the highest impact energy, so the initial delamination was more severe compared to the rest of the samples which could be captured via EMI accurately. Except sample 12, lower accuracy for RUL\_EMI holds for rest of the samples, while converging with lower error in later cycles in all cases.

RUL-fused-1 and RUL-fused-2 demonstrate a consistent and stable performance for all tested samples. Sample 9 is a case in which delamination was propagated significantly faster in one layer than in others. It is seen in its prediction that all input types perform closely, and it demonstrates an early prediction with a

convergence in its final cycle. In **Figure 5.7**, the average error values for each sample are presented and EMI\_RUL has the maximum error in most of the cases. The results show that in **Figure 5.8**, while the RUL-GW operates with lower error than RUL-EMI, RUL-fused-1 and RUL-fused-2 have higher accuracy on average through the cycles in addition to the better convergence of RUL-fused-2 in the final cycle step.

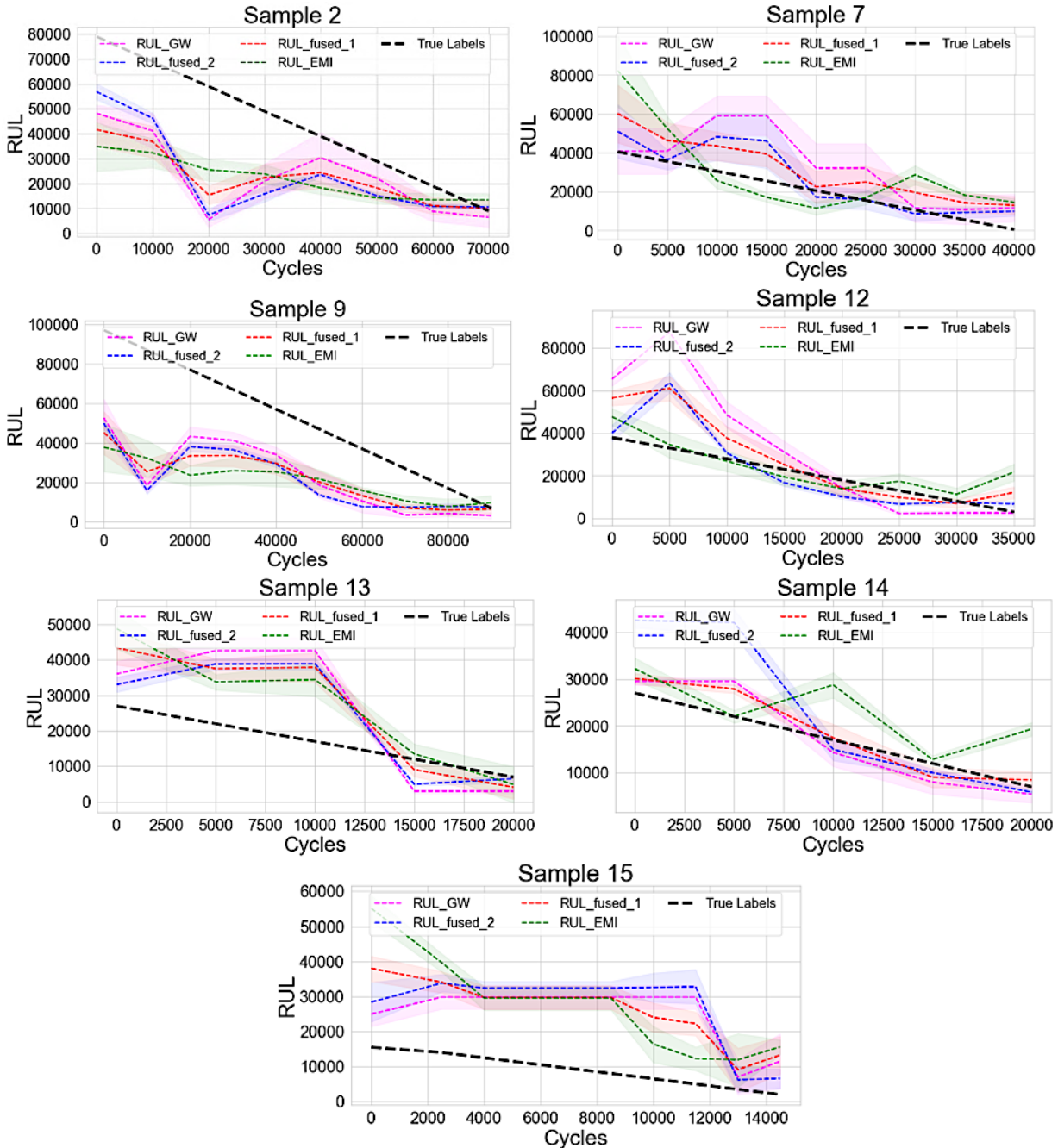


Figure 5.5. RUL prediction results.

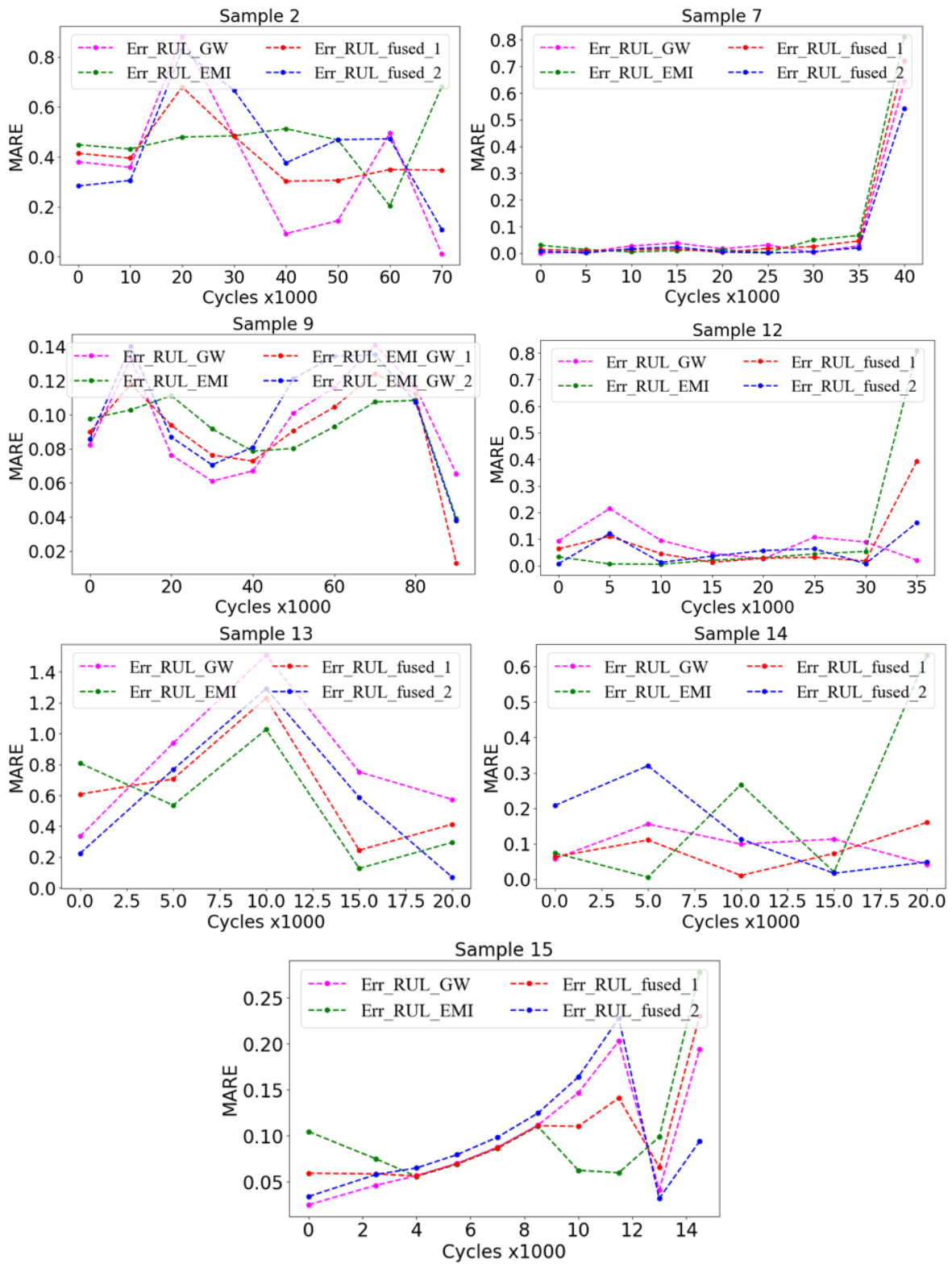


Figure 5.6. RUL prediction accuracy scores for each sample.

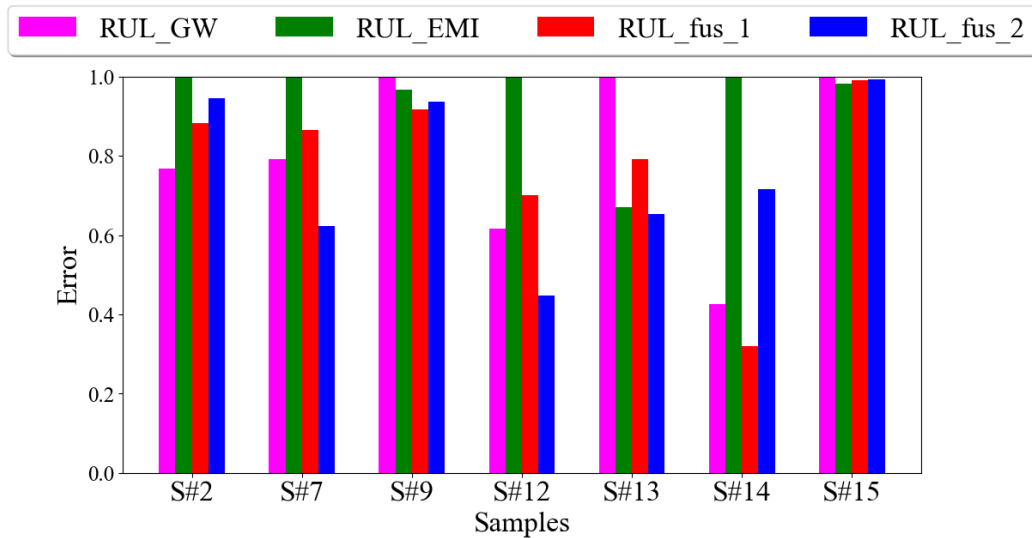


Figure 5.7. Average normalized error for each sample.

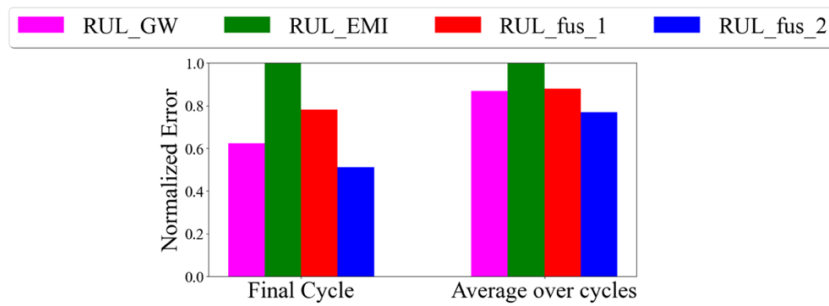


Figure 5.8. Average normalized error for each RUL model.

To better understand the results of the obtained RUL prediction, some critical parameters need to be given attention. Considering the load scenarios discussed earlier in this study, fast and slow growth trends in the delamination may affect the performance of GW and EMI results and the RUL prognostic. In the case of sample 2, it is seen in the c-scan measurements that delamination presented a slow growth behavior in the earlier cycles, and it was poorly captured in EMI-DIs. It is also seen in its RUL predictions that RUL-EMI has the lowest accuracy while RUL-GW presents significantly higher performance. That can be correlated with the fact that GW is sensitive waveforms to the slight variations in the damage and the structure. Another point regarding to the performance of RUL-GW can be explained with the damage mechanisms occur during the fatigue life of the structure and cannot be quantified through c-scan measurements. Since the GW signal conveys information from all structures and considering other damage mechanisms involved in structural degradation, GW-DIs may be more capable of predicting the RUL than EMI-DIs. However, as the delamination propagates and approaches the sensor locations, EMI performance is expected to improve, and this improvement manifests itself in RUL predictions as well.

RUL-fused-1 and RUL\_fused\_2 indicates the robustness of the proposed fusion methodology with lower errors while RUL-fused-1 mitigates the less accurate predictions of EMI and GW inputs, RUL\_fused\_2 achieves higher scores in terms of its final cycle convergence and through the fatigue life of the samples. The improvement of RUL\_fused\_2 is calculated considering less effective prediction of EMI and a 48% improvement in final cycle and %24 in overall cycles is achieved.

Additionally, there are some limitations regarding the proposed framework. Firstly, the DNN model is trained via DIs obtained through signal processing. This poses a significant challenge considering the complex relation between the damage and GW signals and the limited range coverage of EMI measurements. Any noise or variations in the signal acquisition and processing may manifest itself in

obtained DIs and can be the source of error in the predictions. Furthermore, prognostic framework has limited degradation scenarios regarding loads and impact. Besides, proposed DNN models can be adapted to capture DIs separately from each path instead of globally represented DIs by converting it to a more complex model in terms of its architecture. Finally, although the proposed prognostic methodology utilizes a DNN, there is potential to further develop and explore various regression models to more effectively leverage their respective advantages.

## 5.4 Conclusion

This chapter focus on a novel framework that integrates GW and EMI signals for RUL prognostic of woven CFRP samples that are subject to compressive fatigue loading with impact-induced delamination. Unique characteristics of both techniques improve the reliability of the results, as the integrated methodology allows for detailed understanding by capturing the variations in DIs for different loading cases, such as fast growth and slow growth delamination effects. A DNN model with MLP architecture and WAE method is developed to fuse EMI-DIs and GW-DIs. Finally, it demonstrated that while RUL obtained via GW-DIs performs with better accuracy than EMI-DIs in average, the proposed DNN-based fusion model presents less variation throughout the fatigue cycles and holds a higher accuracy in an average of the samples compared to sole EMI or GW-based prognostic.

As the limitations are mentioned, to mitigate the potential effects that may occur in the DI extraction step, two steps can be taken: firstly, the paths can be assigned as independent features into the DNN model, enhancing its ability to capture a broader representation for the degradation of the structure. Secondly, incorporating the total signal of GW or the measurement of EMI into the DNN model may provide more comprehensive information for improved RUL estimation. Consequently, future efforts will focus on advancing the RUL methodology by integrating these insights in the next chapter of this thesis.

## **6 Prognosis of RUL with Delamination Growth via GW-SHM**

## 6.1 Introduction

A GW-SHM-based prognostic approach that targets RUL and delamination size in a data-driven framework is investigated in this study. The goal of this approach is to enhance the interpretability of the learned representations by treating RUL and delamination size as separate outputs in the model. To achieve this, a DNN model is implemented for regression tasks, with its architecture and hyperparameters carefully adjusted based on the input and target data. The approach aims to analyze the impact of various GW signal paths on RUL and delamination size predictions across different samples and as second objective a more generalizable model that can integrate DIs from multiple sources is developed. This integrated methodology provides a comprehensive view of damage mechanisms, contributing to a more accurate and reliable prognosis.

## 6.2 Methodology

GW-DIs were extracted for each of the ten samples in the main dataset. Considering their prognosability in terms of their EoL span, the dataset for the proposed methodology includes samples 2, 7, 9, 12, 13, 14, and 15, resulting in a total of seven samples. The selection of DIs and frequencies was refined based on their prognostic performance metrics and their physical significance. For this work, frequencies of 140 kHz, 160 kHz, and 180 kHz were chosen, as they demonstrated relatively higher average prognostic performance. DI-1, DI-2, and DI-3 were selected for this methodology due to their foundation in energy variation. This extensive feature set provides a comprehensive dataset for capturing the damage progression and supporting the prognostic analysis. It is essential to note that the number of total cycle intervals that GWs are collected varies for each sample due to the differences in their end-of-life spans, which range from 6600 to 97000 cycles. To create data steps with constant intervals for each sample, missing values are filled by interpolation after the DI extraction step. The input set is used to train MLP models for regression with two distinct objectives. The first is to examine the path dependency of the obtained GW-DIs on RUL predictions, while the second aims to develop a generalized framework for RUL prognostics based on GW-DIs. A more detailed explanation of the input set organization and model architecture is provided in the following sub-sections..

### 6.2.1 Input Organization

Two different approaches have been investigated for the prognosis of delamination growth and RUL in this work, thus the datasets are organized in two ways. For the first dataset type, data has been prepared for training considering the model's input size equals the number of DIs,  $N_{DI}$ , and the number of frequencies,  $N_f$ . Paths are divided into two groups for training and testing purposes. For each sample, a total of 18 paths have been separated in terms of the actuator-sensor path, resulting in 15 paths for training data and three paths for testing considering LOOCV that allows for the evaluation of the model's performance using data that was not previously introduced during training, thereby assessing their effectiveness in handling unseen data. More detail, paths from five actuators to each three sensors are assigned to the training set, while one actuator to three sensor paths are reserved for the testing set. This arrangement facilitates a comprehensive evaluation of the performance of DIs based on specific testing paths. Outputs are quantified delamination length and RUL with a threshold that is indicated individually for ten samples, except Sample 12 and Sample 13, as they do not have an accurate damage quantification; therefore, their output is only defined as  $y_{RUL}$ .

For the second approach of this work, the dataset has been re-organized for Framework 2 so that the training set contains DIs from each sample, and the number of neurons in the input layer was allocated considering the number of paths in addition to  $N_f$  and  $N_{DI}$ . This approach results in a total neuron number of  $9 \times 18 = 162$  in the input layer. While the data organization remains the same, RUL and delamination length prediction models used different sample sets; for the RUL prediction, Sample 2, Sample 7, Sample 9,

Sample 12, Sample 13, Sample 14, and Sample 15 are merged considering the prognosability, which means the distribution of sample's end-of-life merit. Conversely, for the delamination length prediction, Sample 2, Sample 7, Sample 9, Sample 10, Sample 14, and Sample 15 pooled as Sample 12 and 13 have no complete damage state labels.

The final steps in the data organization procedure for Frameworks 1 and 2 involve normalization and standardization, which are crucial for enabling the model to learn effectively, leading to better generalization and improved performance when making predictions on new data. Normalization involves scaling the data to a range between 0 and 1, ensuring consistency and preventing any feature dominating the model's learning process. This is particularly useful when dealing with features of varying magnitudes, ensuring each feature contributes proportionally to the model's training. For framework 1, the input data in the sample domain considers each path independently for a 0 to 1 normalization. Standardization involves transforming the data to have a mean of 0 and a standard deviation of 1. This process ensures that the features are centered around zero and have a consistent scale, making it easier for the model to converge during training. Framework 2 uses the standardized dataset, considering each specific path of each sample separately to ensure that varying magnitudes are retained to maintain the uniqueness of each data point in the input set. Any data leakage is prevented as the training and testing data are standardized in their own domain.

### 6.2.2 Model Architecture

The DNN model has five layers for regression tasks, with the last layer having one output for each learning phase, RUL and damage length. The complete learning scheme is illustrated in **Figure 6.1**.

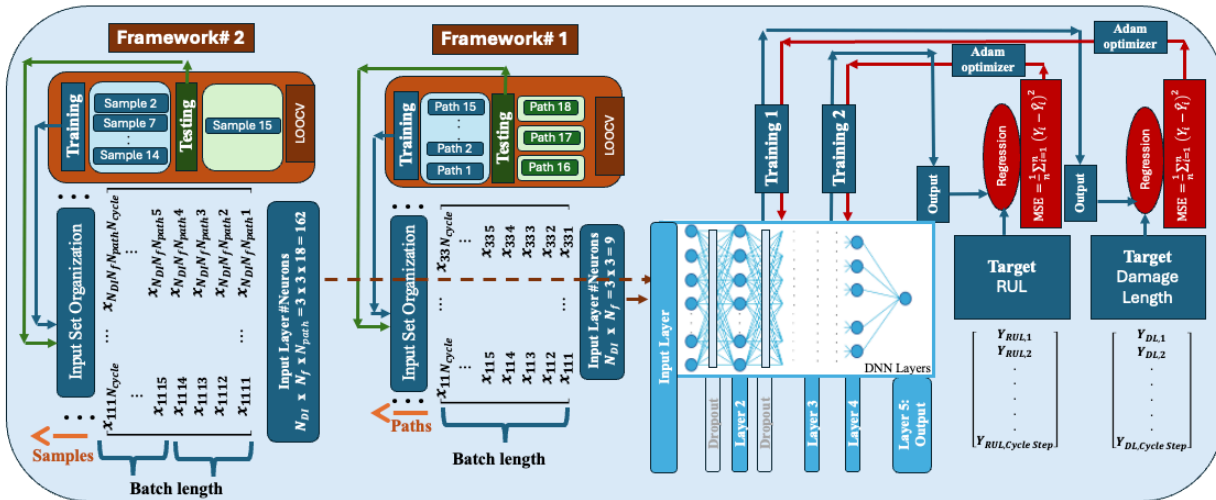


Figure 6.1. Dataset types and learning models.

In the case of Framework 1, the DNN model is re-trained for both RUL and damage length targets each time the training-testing sets are shuffled, and this process is repeated such that each path in the dataset is used once as the test set. In this framework, training and testing are achieved in the one-sample domain. The path sensitivity is investigated as each actuator-sensor path is involved/excluded one after another, and the same procedure is repeated for each sample in the dataset in LOOCV manner. In the second framework, multiple samples are collected in training, and one sample not included in the training is used in the testing phase following the LOOCV as well.

Hyperparameters are optimized experimentally by surveying the training loss in terms of the MSE value, and they are chosen once the model becomes stable and has the highest accuracy. **Table 6.1** gives the hyperparameter values that are tuned for each framework. For Type 1, batch size  $L_{batch}^s$  denotes the max value of  $N_{cycle}$  of each sample and takes the values of 8, 9, 10, 5, 8, 6, 5, 10 in the training phase considering

the Sample 2, Sample 7, Sample 9, Sample 10, Sample 12, Sample 13, Sample 14, Sample 15. The model characteristics were applied in the same way for the RUL target and delamination length. In Type 2, the model has two sub-types; type 2 is trained according to the target of delamination length, and Type 3 is tuned for RUL prediction. For both types, batch sizes remain constant, and the activation function is adapted as tanh for the first two layers' outputs, while type 3 has ReLU as its activation function. Dropout regularization layers are used after layer one and layer 2 with a value of 0.2. Finally, to generate confidence bounds for the predictions, the model was re-initiated and re-trained ten times with different initial weights, yielding varied predictions each time. This approach demonstrated the stability of the proposed model by illustrating how predictions consistently fell within a specific range, confirming the robustness of the model across initializations.

Table 6-1. Hyperparameters of learning model Type 1 in Framework #1.

Type	$N_{neurons}$							Initial Learning Rate	Batch Size
	Layer 1 ReLU	Dropout 0.2	Layer 2 ReLU	Dropout 0.2	Layer 3 ReLU	Layer 4 ReLU	Layer 5 Linear		
1	240	Dropout 0.2	120	Dropout 0.2	60	30	1	0.0001	$L_{batch}^s$

Table 6-2. Hyperparameters of learning model Type 2 in Framework #2.

Type	$N_{neurons}$							Initial Learning Rate	Batch Size
	Layer 1 ReLU	Dropout 0.2	Layer 2 ReLU	Dropout 0.2	Layer 3 ReLU	Layer 4 ReLU	Layer 5 Linear		
2	240	Dropout 0.2	120	Dropout 0.2	60	30	1	0.001	4

Table 6-3. Hyperparameters of learning model Type 3 in Framework #3.

Type	$N_{neurons}$							Initial Learning Rate	Batch Size
	Layer 1 tanh	Dropout 0.2	Layer 2 tanh	Dropout 0.2	Layer 3 ReLU	Layer 4 ReLU	Layer 5 Linear		
3	240	Dropout 0.2	120	Dropout 0.2	60	30	1	0.001	4

## 6.3 Results

### 6.3.1 Path-Sensitivity Analysis

This section presents and discusses prediction results according to Framework 1. As the model is re-trained separately for each output set of delamination length and RUL, the performance of each path from each sample is investigated in a comparative way for the samples shared between damage size and RUL prediction training stack. Errors of predictions are given by the metric of MAPE, given in equation 6-1,

while  $\bar{Y}_d^{i,m}$  denotes the true label for delamination length,  $\bar{Y}_R^{i,m}$  is the true label for RUL.  $\bar{Y}_d^{i,p}$  refers the predicted delamination length at  $i$ th cycle and  $\bar{Y}_R^{i,p}$  is for the predicted value of RUL. In sub-figure a of **Figure 6.2**, errors based on MARE, given equations 6-1 and 6-2, is presented for each path for delamination length prediction. Sub-figure b presents the average error of each path per cycle. Sub-figure c indicates error values for RUL prediction based on each testing path and Sub-figure d, the path average error per cycle is given. According to the obtained error values, it is evident that paths with higher accuracy vary for each sample. Furthermore, less effective paths in predicting delamination length may not necessarily yield poor outcomes for RUL prediction. However, a correlation can be captured in the case of Sample 7, Sample 14, and Sample 15, where the lowest MARE for delamination length prediction exhibits high accuracy in RUL prediction. In the case of Sample 7, path 8 has a high prediction error for delamination length prediction, and it holds the same behavior for RUL prediction as well. As the predictions are GW-DIs based, this correlation can be considered as the sensitivity of these DIs to delamination.

Another aspect requiring attention in the error values given in **Figure 6.2** is that the errors for RUL prediction appear to be generally higher than delamination length prediction. This can be attributed to the nature of the RUL target values, which typically have a higher range, often in the order of 10000 cycles. In contrast, delamination length targets exhibit smaller intervals; for instance, Sample 2 indicates a prediction range of 25 to 33.6 mm. Consequently, if the model incorrectly predicts the final cycle, for example, estimating 30000 instead of 1000, the resulting error is significantly amplified, overshadowing the accuracy of predictions made for earlier cycles, which is apparent in **Figure 6.2** in cycle-based results, in sub-figure b and d.

$$MAPE_{path-d} = \frac{1}{N_{cycle}} \sum_{i=1}^{N_{cycle}} \left| \frac{\bar{Y}_d^{i,m} - \bar{Y}_d^{i,p}}{\bar{Y}_d^{i,m}} \right|, \quad MAPE_{cycle-d} = \frac{1}{N_{path}} \sum_{i=1}^{N_{path}} \left| \frac{\bar{Y}_d^{i,m} - \bar{Y}_d^{i,p}}{\bar{Y}_d^{i,m}} \right| \quad (6-1)$$

$$MAPE_{path-R} = \frac{1}{N_{cycle}} \sum_{i=1}^{N_{cycle}} \left| \frac{\bar{Y}_R^{i,m} - \bar{Y}_R^{i,p}}{\bar{Y}_R^{i,m}} \right|, \quad MAPE_{cycle-R} = \frac{1}{N_{path}} \sum_{i=1}^{N_{path}} \left| \frac{\bar{Y}_R^{i,m} - \bar{Y}_R^{i,p}}{\bar{Y}_R^{i,m}} \right| \quad (6-2)$$

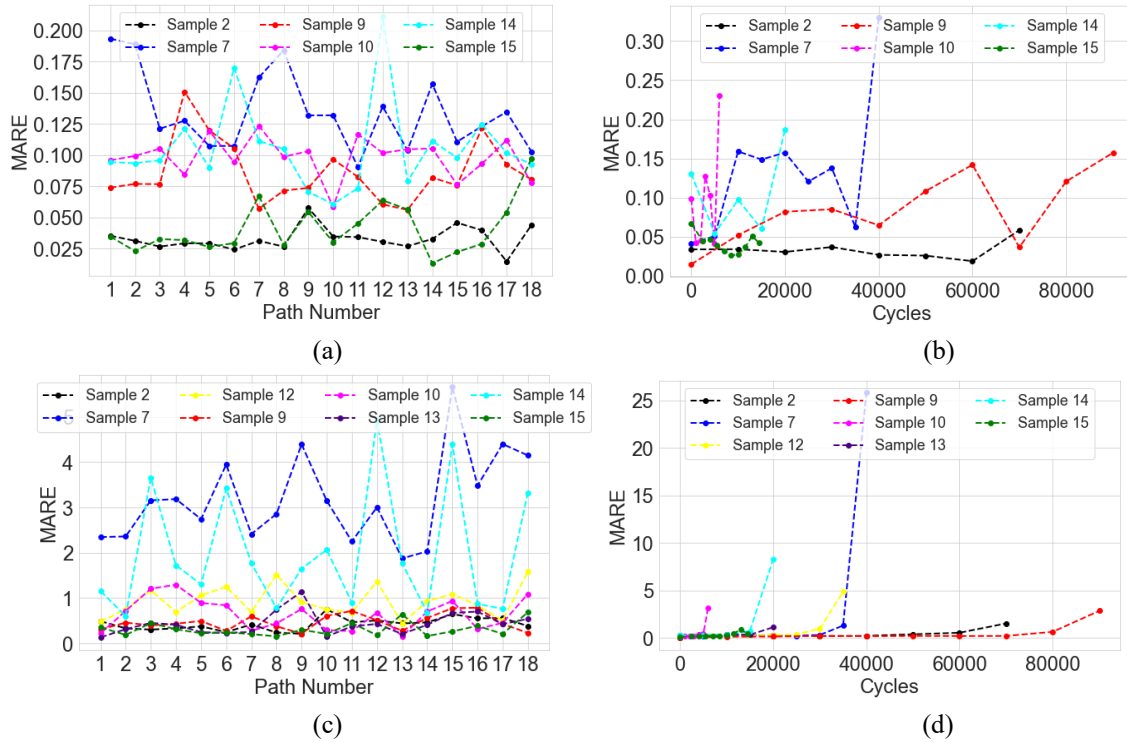


Figure 6.2. Error values for (a) delamination length prediction of each path (b) delamination length prediction of each cycle and for c) RUL prediction of each path d) RUL prediction of each cycle.

According to **Figure 6.2**, cycle-based error representation, both figures reveal that model predictions exhibit lower accuracy for the latest cycle step across all RUL and delamination length prediction samples, except for Sample 15, where the lowest accuracy occurs one step before the final cycle step. Conversely, predictions for damage length still exhibit some error, although not as pronounced as for the final cycle step; the error is likely distributed across each cycle step. In contrast, RUL predictions show a more drastic variation in accuracy, with significant decreases observed for the final cycle step compared to earlier cycles. To investigate the results better, DIs' sensitivity to delamination accumulation should be considered. In contrast to the others, in terms of the delamination in the threshold level, the less sensitive paths might have less confidence and accuracy, which may bring higher errors in the results for the final step prediction. This lower accuracy at the threshold level for specific paths might result from high scattering and reflection in the signal induced by larger delamination.

To compare the performance of testing paths on each trained model, the path with the highest accuracy for delamination length prediction is selected for each sample. Subsequently, the results of the same path for RUL and delamination length prediction are presented together in **Figure 6.3** and in **Figure 6.4**, on the other hand, the paths with the highest accuracy for RUL predictions are selected, and their performance is also demonstrated for delamination length predictions together. The figures indicate that paths performing well on delamination prediction yield RUL prediction almost as good as delamination length prediction. Samples 10 and 15 exhibit considerably good accuracy for both targets in terms of their convergence in the final cycle. In the context of delamination length prediction, the target presents a significant increase in the later cycles. Although the model can generally capture this trend in most samples, it tends to underestimate the maximum delamination length, and this underestimation becomes the primary source of average error.

Besides, it should be highlighted that, even if the accuracy is lower in final cycles, the coherence between the delamination and RUL predictions is visible. In the case of Sample 2, as the model predicts that delamination is growing, the RUL prediction at the same cycle step is decreasing, indicating severe damage accumulation. This pattern is observed in almost all samples, demonstrating the reliability and consistency

of the model and the input DI data. However, it may not accurately reflect the actual conditions in every case.

Moreover, when comparing **Figure 6.3** and **Figure 6.4**, it becomes evident that while paths yielding the best predictions for delamination length still maintain acceptable accuracy for RUL prediction, the opposite is not valid for all the samples. Paths resulting in the highest accuracy for RUL prediction do not exhibit the same level of performance for delamination length predictions for all samples. For example, Sample 9, apart from the lower accuracy, the confidence bounds are also larger, indicating lower confidence in the predictions for delamination length for the path that produces the most accurate RUL prediction.

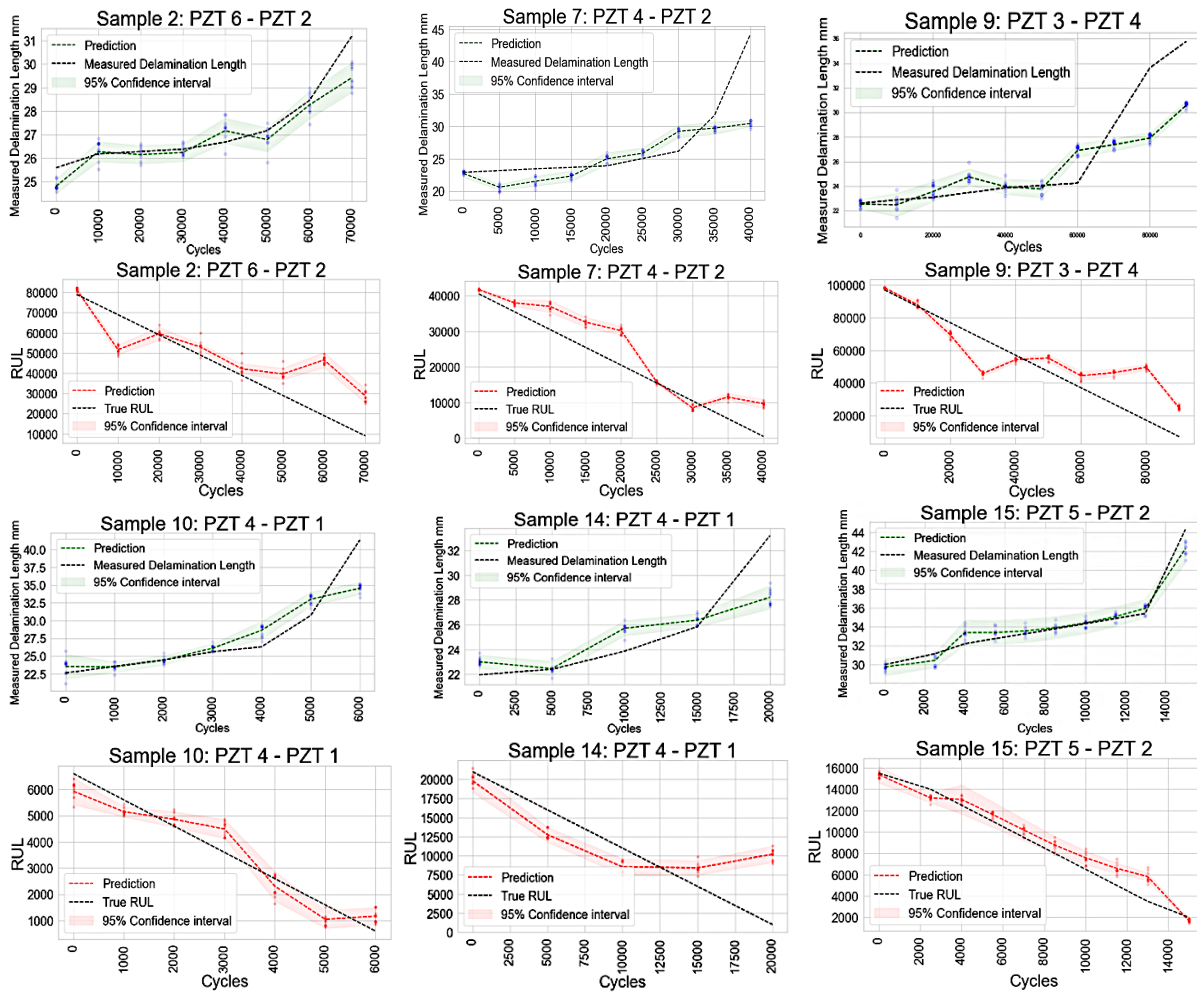


Figure 6.3. Comparison of the best results of delamination length prediction with the RUL predictions of the same path.

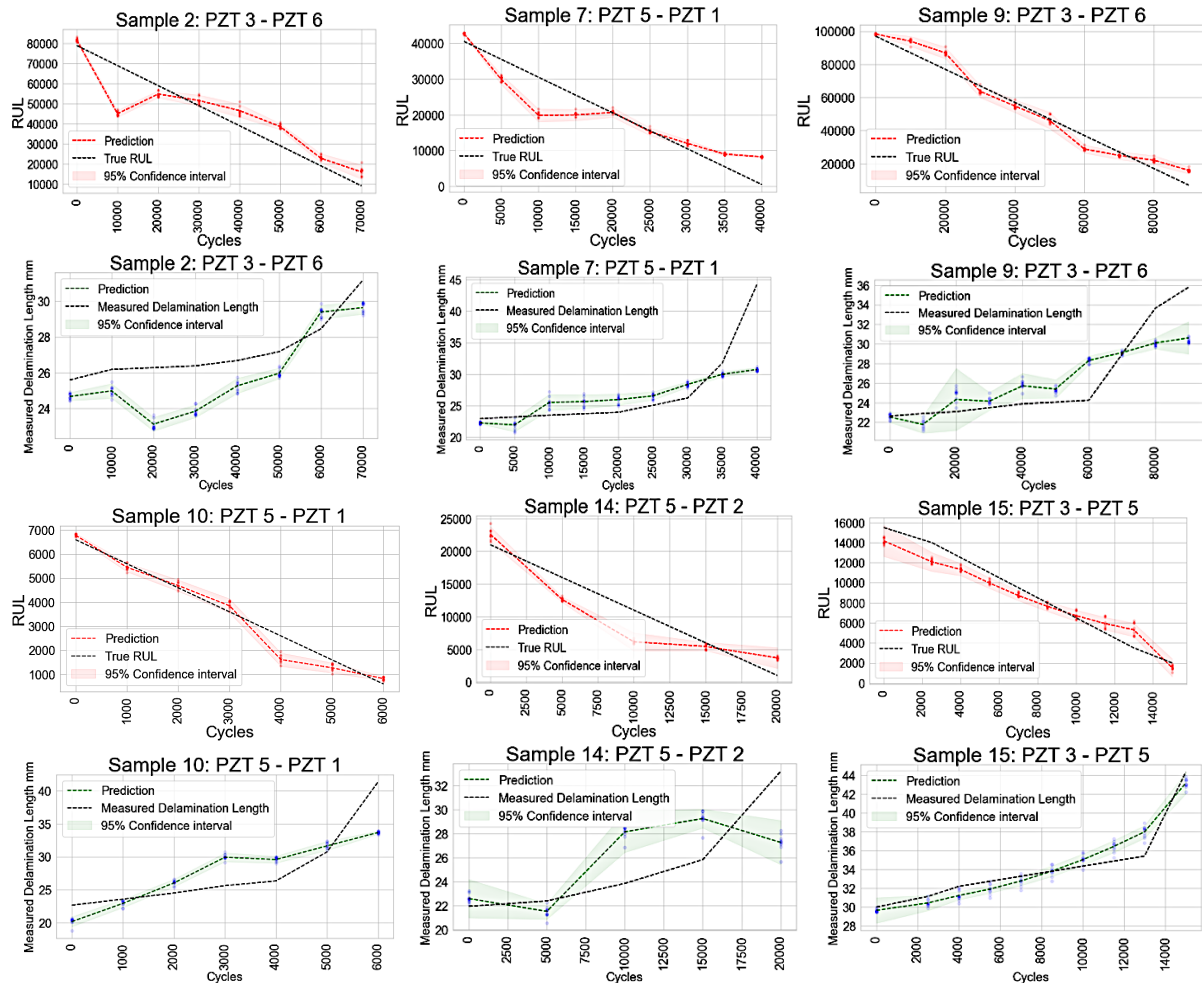


Figure 6.4. Comparison of the best results of RUL prediction with the delamination length predictions of the same path.

### 6.3.2 Ensembled-Dataset-based Prediction

In this section, the second framework proposed in this work is presented. In Framework 2, the training set is determined in combination with multiple samples and paths tested in Framework 1 and assigned as features aiming that the model will capture the information most relevant to the targeted output. This model has two sub-types to obtain the most accurate and stable model for each target. Subtype A targets the delamination length values as output, and subtype B is trained using the RUL target. Chosen samples to be merged for LOOCV folds are created differently for both sub-types. The delamination length prediction model is trained based on Sample 2, Sample 7, Sample 9, Sample 10, Sample 14, and Sample 15. The RUL model is constructed based on Sample 2, Sample 7, Sample 9, Sample 12, Sample 13, Sample 14, and Sample 15, considering their closer prognosability. **Figure 6.5** presents prediction results based on the delamination length prediction. Among the results, the best convergence is observed for Sample 7, while poor coherence is evident for Sample 2 and Sample 10. Sample 9 gradually performs better after the 50000th cycle. Despite the poor convergence in earlier cycles, the model could converge in the last cycle differently than the results in Framework 1. In **Figure 6.6**, the analysis suggests that the model exhibits a promising ability to approximate the monotonic behavior of RUL with relatively more robust performance observed in the predictions for Sample 7, Sample 12, and Sample 15. However, the relatively better accuracy of Sample 7 is not maintained after the 30000th cycle. Except for Sample 14 and Sample 7, RUL predictions are converging toward the final step. Sample 9 demonstrates an early prediction throughout the fatigue life of the sample. Sample 14 accurately predicts the RUL before the mid-life of the sample while still overestimating the final remaining time.

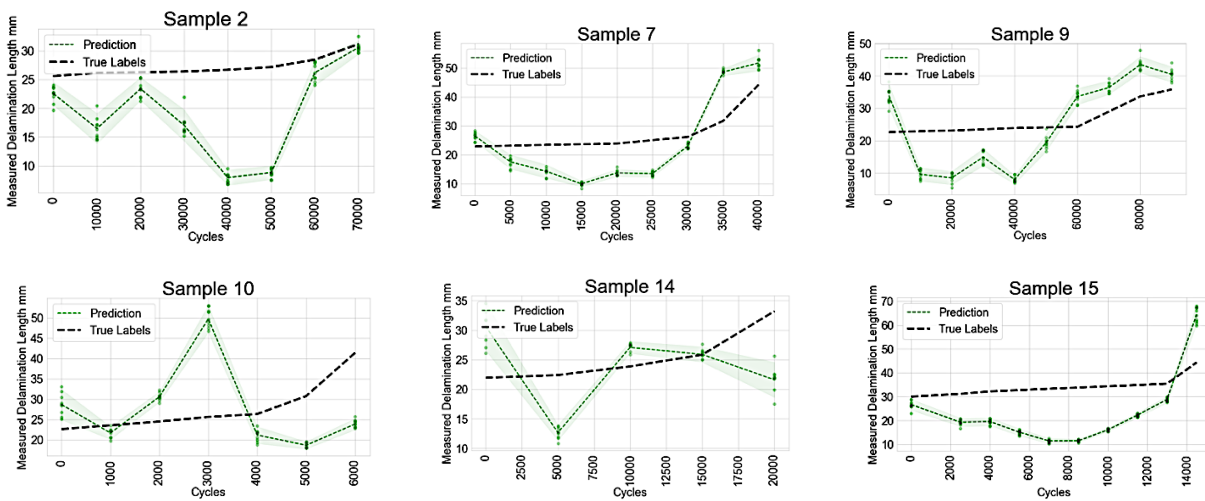


Figure 6.5. Test results of delamination length predictions.

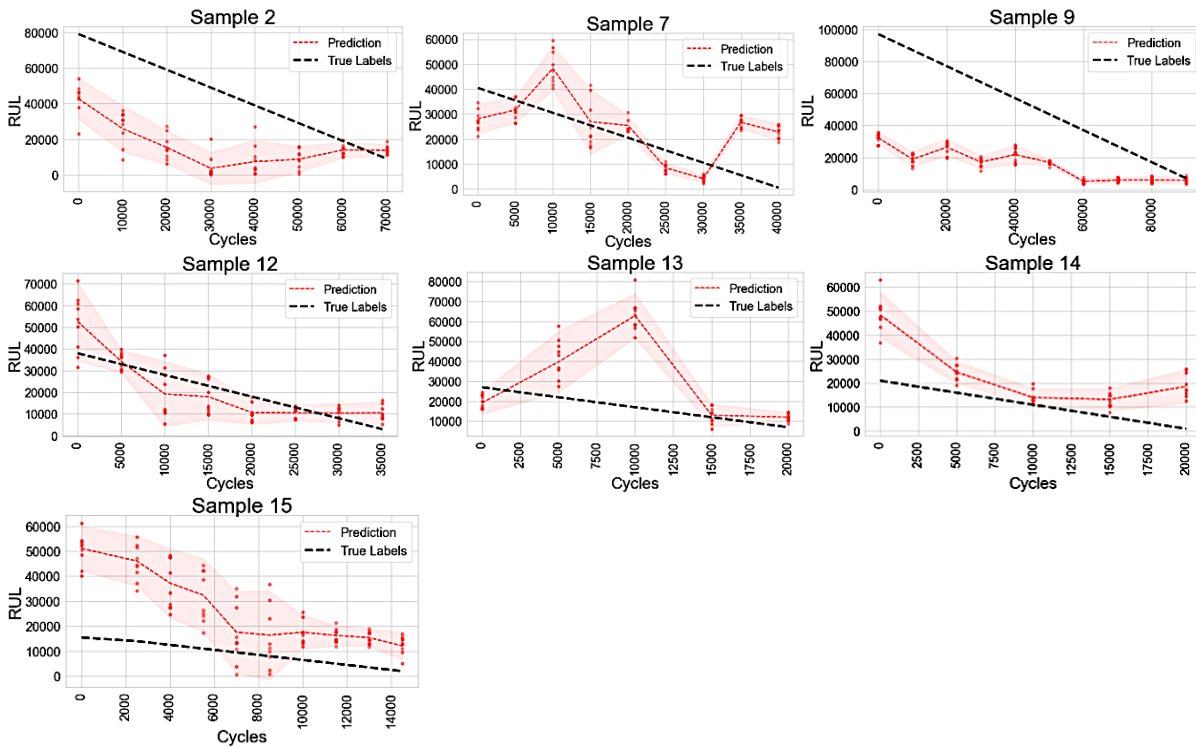


Figure 6.6. Test results of RUL predictions.

### 6.4 Discussion

Prediction results based on one-sample-domain has been presented by investigating the contribution of each path on both RUL and delamination length prediction. As mentioned in the previous section, for some samples while the predictions both perform well for delamination prediction and RUL prediction, some may exhibit differently from each other. To understand the underlying reasons for this discrepancy, it is important to discuss possible factors that may contribute to these results.

Firstly, the focus can be given to DIs and the information they excel. DI extraction step was carried out specifically to isolate the delamination related portion of GW signal which enables to investigate the contribution of delamination growth to end-of-life of the samples. This is a challenging task to achieve and for some DIs delamination information might be limited or information from other damage types might co-

exist. Hence, it would be logical to observe that paths more sensitive to delamination growth result in higher accuracy in predicting maximum delamination length and still perform well on RUL prediction. This is because delamination was the dominant damage mode in the samples, and the final failure consistently occurred when delamination reached its maximum size, serving as the end-of-life event. On the other hand, paths demonstrating higher accuracy in RUL prediction are likely to encapsulate information from the entire structure, potentially encompassing other types of damage that contribute to the assessment of delamination propagation and/or these paths may operate independently from delamination but still play a role in determining the overall health state of the sample.

As mentioned earlier, the primary source of error in many predictions lies in the final prediction step. For instance, in the case of Sample 7, the model's overall performance is poor; however, it exhibits moderate accuracy until the 35000th cycle. The issue arises from the faster growth of delamination length, which is measured at its maximum length, a trend that the model failed to capture from the data. Conversely, this discrepancy is not observed in Sample 2 and Sample 9, indicating a potential difference in the input DIs and their ability to accurately reflect damage evaluation for each sample.

With the framework 2, damage propagation and RUL prognostics have been conducted in Framework 2, which ensembles samples from the dataset to create a more generalized prediction model. For this purpose, samples with appropriate target characteristics are selected for Model 2 and Model 3. Model 2 requires a complete label set for maximum measured delamination length, while Model 3 aims for closer prognosability for the samples. As a result, six samples are assigned for Model 2 samples with number 2, 7, 9, 10, 14, and 15, and Model 3 is trained and tested with Samples 2, 7, 9, 12, 14, and 15.

While the samples perform well in Model 2 and effectively capture the increasing trend in severity, they also perform well in Model 3 by reflecting it in RUL prediction with a better performance in validation set and limited capability on testing set. It is observed that for the ensemble model of RUL, that is Model 3, distribution of the targets play an important role to make an efficient prediction. In the case of Sample 14 and Sample 15, their first cycle predictions are very high compared to the samples in the dataset, which are the samples have a smaller end-of-life time. Once they are excluded from the training, the capability of model to predict lower value in the initial RUL step becoming with less accuracy.

In addition to model-based constraints, the DIs in the input data that play a significant role in the performance of the ensemble-based model can be the origin of less effective testing results. The possible noise and errors in acquired GW signals can transfer it to DI extraction, may limit the model's learning capability. This effect might be mitigated in some ways, such as, training the model with the full signal in supervised manner to eliminate DI extraction-based errors. However, adopting such an approach would necessitate the use of more complex and deep learning architectures, which could potentially decrease the explainability of the model. Another approach could involve increasing the number of samples in the dataset to encompass a wider range of damage and end-of-life scenarios. This would enhance the generalization capability of the model. On the other hand, creating such a dataset is highly challenging and resource-intensive, requiring significant experimental effort to generate. Consequently, despite the constraints and the limited number of samples in the dataset, the results show promise in providing efficient and interpretable data-driven RUL and progressive damage prognostics.

## 6.5 Conclusion

This study presents a novel GW-SHM-based integrated prognostic approach designed to predict both RUL and delamination size within a data-driven framework. Considering the proposed methodology, two main challenges have been aimed to be answered. To reveal the delamination state together with EoL of structure the prediction of delamination growth until a threshold level is included in a RUL prognostic framework to improve the reliability and effectiveness of the RUL prognosis. By adapting GW-DIs within a DNN-based regression model, a robust prognostic methodology is achieved, which enhances the explainability of RUL

predictions, providing insights into the progression of delamination. Secondly, two frameworks are adapted to investigate various aspects of prognostics, one in an individual sample domain to reveal path dependency in RUL and delamination length prognosis and the second in an ensemble dataset domain proposing a more generic model for RUL and delamination growth prediction.

In the domain of one sample-based analysis, results reveal that the actuator-sensor paths that demonstrate optimal performance in RUL prediction do not consistently coincide with those more sensitive to delamination. However, based on the results, the paths that indicate the highest accuracy for delamination growth prediction also tend to perform well for RUL prognostic. This may indicate for these samples that the corresponding GW-DIs might be more representative of the overall structural health state and perform better in the RUL prediction of the sample. Although the study notes variations in the sensitivity of different actuator-sensor paths to damage, it demonstrates the positive correlation between paths and their predictive capability in RUL and delamination state.

As the second approach, the dataset is created with samples subjected to varied stress levels during their fatigue life, and the models account for multiple scenarios that have been achieved separately for RUL and delamination growth prognostic. Model performance for delamination and RUL predictions exhibit promising capability in capturing both targets through given GW-DIs. Furthermore, developing an ensemble dataset-based DNN model demonstrates the methodology's robustness and adaptability across different stress scenarios and structural conditions.



## **7 Prognosis of Delamination Induced Failure Blending Deep Learning with Signal Processing**

## 7.1 Introduction

The integration of DL techniques in the field of SHM has paved the way for more advanced and precise prognostic models. DL models are well-suited for GW analysis because they excel at automatically identifying complex patterns and features within high-dimensional, noisy data, making them highly effective for detecting subtle damage signatures and structural anomalies that may be difficult to discern through conventional analytical methods. CNNs offer substantial advantages in pattern recognition within complex signal data, making them well-suited for identifying characteristic features indicative of structural damage. However, despite their strengths, purely data-driven approaches may fall short in terms of physical interpretability to their outcomes, limiting their ability to generalize across diverse operational scenarios. By incorporating GW-DIs into the framework, the model's predictive accuracy is aimed to be improved together with the interpretability of the prognostic results. Integrating domain-specific knowledge into the learning process bridges the gap between data-driven insights and physical phenomena, thereby may enhance the model's prognostic capabilities together with its interpretability. Therefore, in this research, a novel multilevel data-driven prognostic framework is introduced. The framework employs a base learner level and a two-level fusion methodology, combining both direct and feature-based prognostics for enhanced predictive accuracy.

## 7.2 Methodology

At the core of this approach, one-dimensional CNN (1D-CNNs) serve as base learners for the GW signals, while multilayer perceptron (MLP) is used for processing DIs, both targeting RUL prediction. In the base learner level, the framework leverages GW-DIs obtained through signal processing, while the GW signals, represented by their envelope and CWT are used to train the CNN model for RUL prognostics. Each excitation frequency of the GW signals is processed through the base learners and subsequently passed through the fusion levels. This multi-step fusion process allows the system to integrate information from multiple excitation frequencies and diverse features through a two-level fusion approach. The fusion strategy comprises a WAE, MLP and LSTM networks, all trained as regression models, with their performance evaluated and presented in this study. By synthesizing these complementary methods, the proposed framework offers a robust and adaptable solution for improving the accuracy and reliability of RUL predictions.

### 7.2.1 Input Organization

In the prognostic methodology, samples numbered 2, 7, 9, 12, 13, 14, and 15 from the dataset are included. The input set is constructed from GW signals processed using CWT and HT in two distinct ways. First, CWT analysis presents the signals in both time and frequency domains, with a one-dimensional projection obtained via average power calculation. Second, envelope signals are obtained through HT. **Figure 7.1** illustrates the signal processing and DI extraction steps adapted in this study and Eqs. (7-1) – (7-2) presents the DI calculation steps. Signals from each path are treated as independent features in both the CNN and MLP models. The model is trained using input data structured as time-series, but without incorporating explicit time-dependence within its base-learner architecture. The model is trained by feeding the DI history of each sample within the training set. The input datasets are formatted as  $N_{cycle\ steps} \times N_{features}$  for MLP model and  $N_{cycle\ steps} \times L_{signal\ length} \times N_{features}$  for 1D-CNN model both split into testing and validation sets. The MLP dataset has 39x18 and the dataset used to train for 1D-CNN has 39x1401x18 for CNN CWT and 39x250x18 for CNN Env. Training dataset contains six samples, with one sample reserved for testing, following a Leave-One-Out Cross-Validation (LOOCV) approach. This framework evaluates the model's performance on unseen data, ensuring the model's generalization capability. For testing, the model predicts RUL at each time step using unseen data, iteratively estimating RUL across the time horizon. Each specimen is held out as a testing sample during its respective validation iteration. In this study, no

interpolation is applied and only experimentally obtained data is implemented into the framework. Input data are standardized using z-score normalization, applied separately to each DI set; sensor-actuator path under each specific excitation frequency. Hyperparameter optimization is performed experimentally by monitoring the training loss, measured as the MSE on validation data. Validation data is randomly selected from the training set, with 20% of the training data set aside for validation purposes and for monitoring the training loss. The solution space for the architectures demonstrates sufficient convergence, as minor variations in the number of neurons result in a stable validation loss.

$$DI - Env = \frac{[\sum_t^{T_{window}} H(t)]_n}{[\sum_t^{T_{window}} H(t)]_{n=1}} \quad n = 1, \dots, N_{cycle\ steps} \quad (7-1)$$

$$DI - CWT = WAP(t) = \frac{[\sum_t^{T_{window}} AP(t)]_n}{[\sum_t^{T_{window}} AP(t)]_{n=1}} \quad n = 1, \dots, N_{cycle\ steps} \quad (7-2)$$

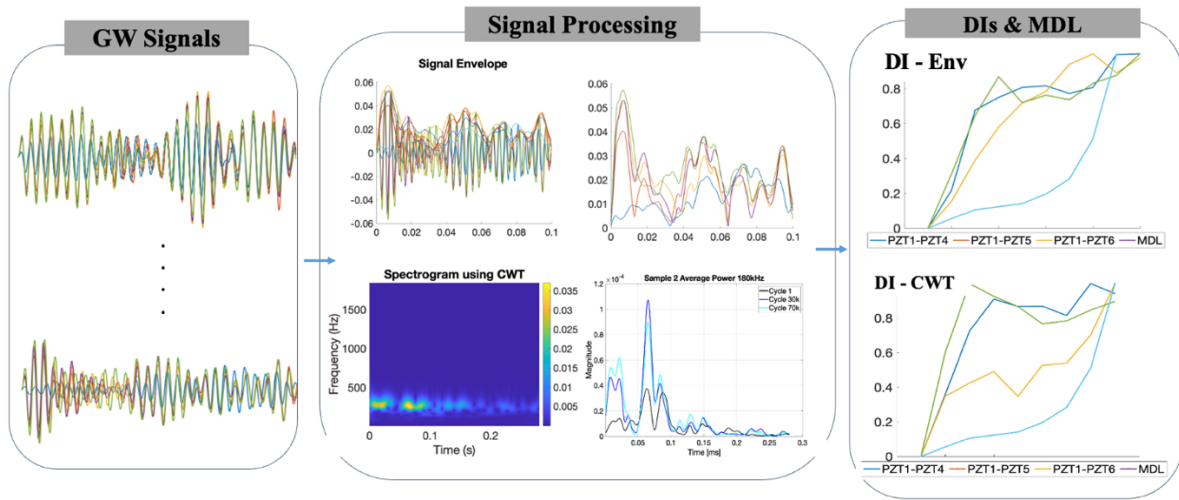


Figure 7.1. Input organization based on GW signals in time and time-frequency domain and with GW-DIs.

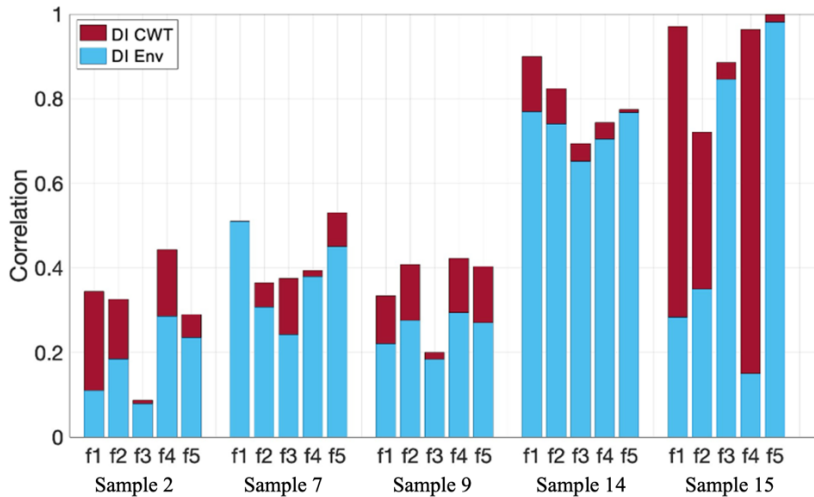


Figure 7.2. Path-averaged correlation values for DI-Env and DI-CWT vs measured delamination length.

In **Figure 7.2**, presents the quantified correlation between the DIs and the MDL across different frequency components, where f1 represents 100 kHz, followed by 120 kHz, 140 kHz, 160 kHz, and 180 kHz up to f5. The results indicate that DI CWT generally achieves higher correlation values across most frequency components and specimens, particularly in Sample 14 and Sample 15. DI Env, while contributing to overall

correlation, shows more pronounced variability across frequencies. Both DI Env and DI CWT exhibit with lower contributions in Sample 1 and Sample 3. As previously mentioned, the correlation metrics are excluded for Sample 12 and Sample 13 due to the noise present in the c-scan images of those samples, which prevented the accurate quantification of delamination length and compromised the reliability of the correlation analysis.

### 7.2.2 Model Architecture

The proposed prognostic model comprises four types of base learners, utilizing both 1-D CNN and MLP architectures, with the complete framework illustrated in **Figure 7.3**.

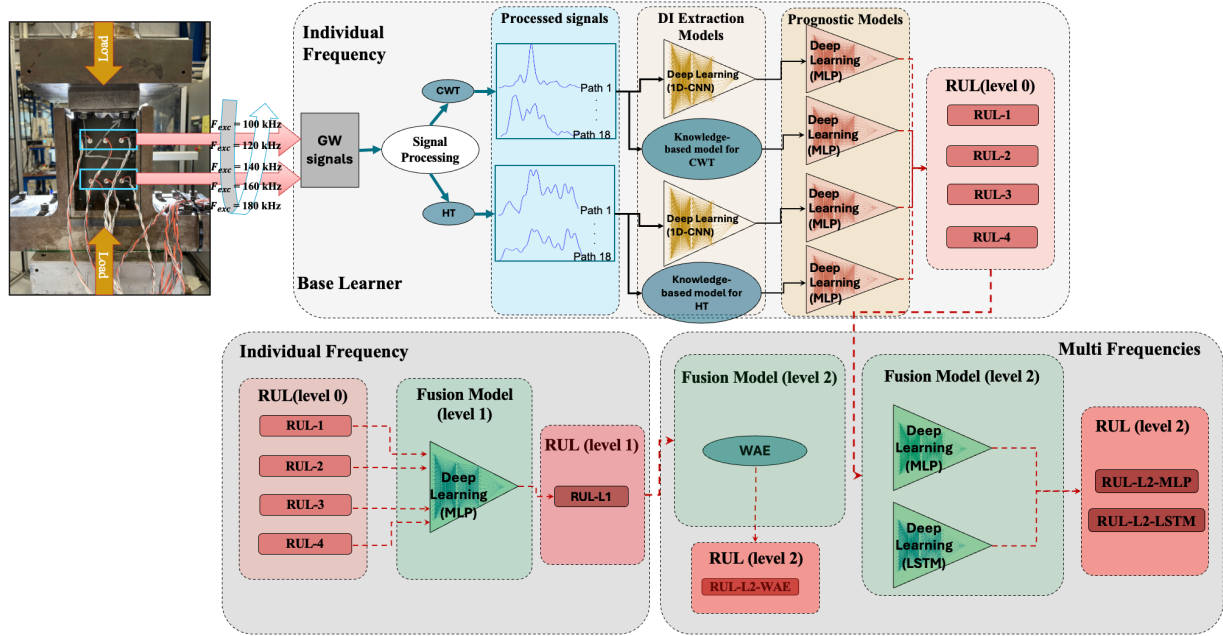


Figure 7.3. Overall proposed framework including base learners and fusion steps at different levels.

### Base Learners

CNN-Base learner is tuned differently in terms of kernel size for HT and CWT processed GW signals, ensuring tailored performance across varying input conditions. Base learners operate separately for each  $f_{exc}$ , and one RUL prediction is generated for each input type: DI CWT, DI Env, CNN CWT, and CNN Env for each  $f_{exc}$ . **Figure 7.4** illustrates the 1D-CNN model with layers and learning flow. CNN models' hyperparameters are optimized according to the specific characteristics of the input signals obtained from CWT and HT outputs, and **Table 7.1** provides detailed parameter settings for CNN base learner for each two-input type. **Figure 7.4** presents the MLP learning process trained via GW-DIs; DI-CWT and DI-HT, given in Equation 8-1 and 8-2. MLP base learner model parameters are given in **Table 7.2**.

The base learners are evaluated using LOOCV, and the prediction results are denoted as follows:

$$RUL_{f_{exc}} - 1; \text{ CNN base learner for CWT input; } RUL_{f_{exc}} - 2; \text{ MLP base learner for DI-CWT input}$$

$$RUL_{f_{exc}} - 3; \text{ MLP base learner for DI-Env input; } RUL_{f_{exc}} - 4; \text{ CNN base learner for Env input.}$$

Table 7-1. CNN-Base learner architectural parameters.

	Conv1D ReLU		Max- Pooling 1D	Flatten	FCL-1 ReLU	Dropout 0.2	FCL-2 ReLU	FCL-3 ReLU	FCL-4 Linear
CNN Filters	Kernel Size- CWT	Kernel Size- HT	Pool Size		$N_{neurons}$		$N_{neurons}$	$N_{neurons}$	$N_{neurons}$
	128	140	25	3	128		64	16	1

Table 7-2. MLP-Base learner architectural parameters.

FCL-1 ReLU	Dropout 0.2	FCL-2 ReLU	FCL-3 ReLU	FCL-4 Linear
$N_{neurons}$		$N_{neurons}$		
32		16	8	1

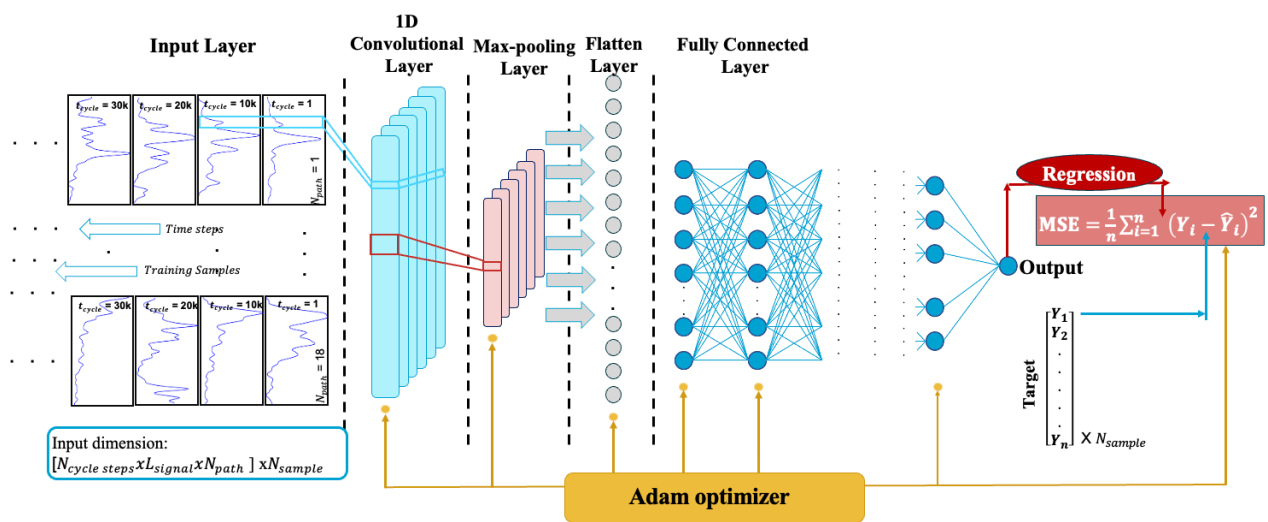


Figure 7.4. 1D CNN base learner.

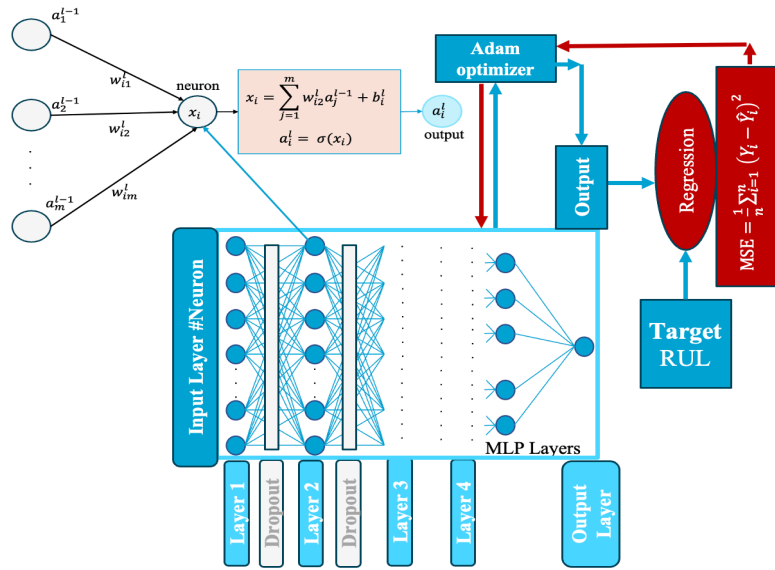


Figure 7.5. MLP architecture for base and fusion learner.

**Fusion Learners**

In the initial level, the base learners are applied to each excitation frequency signal set, generating a total number of 20 RUL predictions for a single test specimen. Following this, the framework incorporates two-level fusion to integrate the information from each frequency set input. In Level-1, the outputs for DI-CWT, DI-Env, CNN-CWT, and CNN-Env from the base learners are concatenated and fed into an MLP model after re-standardization, producing one RUL prediction for each  $f_{exc}$  and tuned parameters for this model are given in **Table 7-5**. Level-2 employs a WAE to combine the outputs from Level-1. MLP and LSTM is utilized to process the complete output set produced by the base learners for each input type and excitation frequency. In this stage, both the MLP and LSTM models take 20 outputs as input, with the LSTM model configured with a 3D input shape, using a time step of 1 and a sample size kept dynamic during LOOCV and it is shown in **Figure 7.6**.

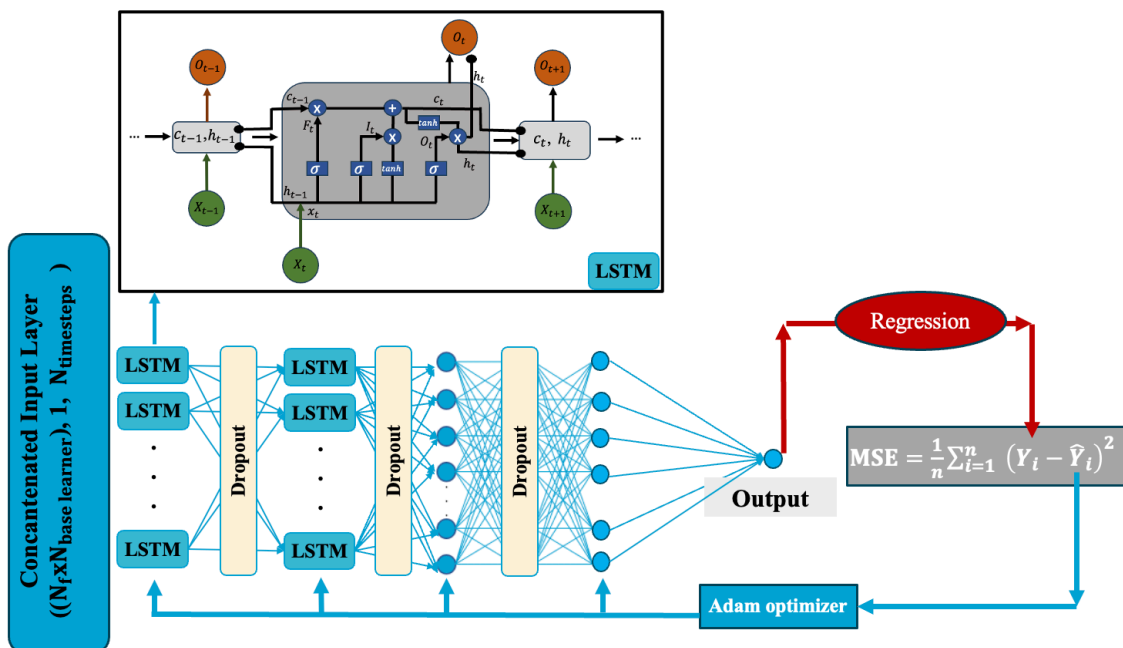


Figure 7.6. LSTM fusion model.

Table 7-3. MLP-L1-Fusion model architectural parameters.

FCL-1 ReLU	Dropout 0.2	FCL-2 ReLU	FCL-3 ReLU	FCL-4 Linear
$N_{neurons}$		$N_{neurons}$		
32		16	8	1

Table 7-4. MLP-L3-Fusion model architectural parameters.

FCL-1 ReLU	Dropout 0.2	FCL-2 ReLU	FCL-3 ReLU	FCL-4 Linear
$N_{neurons}$		$N_{neurons}$		
32		16	8	1

Table 7-5. LSTM-L3-Fusion model architectural parameters.

LSTM-L1 ReLU	Dropout 0.2	LSTM-L1 ReLU	Dropout 0.2	FCL-1 ReLU	Dropout 0.2	FCL-2 ReLU	FCL-3 Linear
$N_{LSTM\ unit}$		$N_{LSTM\ unit}$		$N_{neurons}$		$N_{neurons}$	
32		16		16		8	1

### 7.3 Results

**Figure 7.7** display the predicted RUL for all specimens based on LOOCV sets using different models and input types, including DI-CWT, DI-Env, CNN-CWT, and CNN-Env, results in RUL-1, RUL-2, RUL-3 and RUL-4 for each  $f_{exc}$ . **Table 7-6** presents average error values in terms of MAPE for each model and input types of each sample.

Although the correlations presented in **Figure 7.2** provide valuable insights into the relationship between the measured delamination length and the DIs, as discussed, a one-dimensional quantified delamination length may not be a sufficient criterion for accurately assessing delamination severity or understanding its contribution to RUL estimation. While the correlation metric validates the reliability of the DIs obtained for the degrading structure, it may not be adequate to fully explain their impact on the RUL prediction model. For example, both DIs exhibit high correlation values for Sample 15; however, as shown in **Figure 7.7**, the base CNN models demonstrate higher estimation accuracy compared to models using DI-based inputs. This may suggest that the CNN model is better equipped to capture degradation indicators, potentially accounting for varied damage types, e.g. matrix cracks, and providing a more accurate RUL prediction. On the other hand, for Sample 2 and Sample 7, the correlation is observed to be the lowest, as shown in **Figure 7.7**, where the base learner results indicate the lowest prediction accuracy during the earlier cycles yet converges in later cycles. Samples 2 and 9 exhibit slower degradation in their earlier cycles compared to the other specimens in the dataset. This observation may suggest that DIs may be less effective in capturing the early stages of delamination progression for these samples, while improved accuracy is observed in the base learner model during the later cycles for Sample 2 and Sample 9. Consequently, while growing delamination is a key factor in RUL prediction, establishing a direct correlation across all specimens may not be feasible due to variability in growth rate, interacting damage mechanisms and loading conditions. DI CWT presents higher score in terms of its correlation with

measured delamination length, the base learner prediction results indicate that DI Env has higher accuracy in RUL predictions despite its lower correlation score than DI CWT with c-scan based measured delamination length.

In **Figure 7.7**, Level-1 fusion demonstrates robustness in combining the strengths, minimizing large deviations seen in individual models, as observed in Sample 12, Sample 13, and Sample 14. Especially, in the result of Sample 14, Level-1 fusion presents higher performance reducing the error of each model giving a better convergence in the final cycle. As shown in **Table 7-6**, the CNN-CWT model achieves the highest average accuracy at the lower excitation frequency of 100 kHz. In contrast, at higher frequencies, models based on GW-DIs exhibit lower error values, with the DI-Env model performing particularly well at 160 kHz and 180 kHz. This may suggest that the captured GW mode in DI calculation at these higher frequencies exhibits a stronger interaction with existing structural damage that contributes more significantly to failure. While average error rates may suggest that a particular model performs optimally at a specific  $f_{exc}$ , the performance of each model varies across different specimens at each frequency level. Even though Level-1 fusion models show some strong results, their higher errors in various specimens and inputs indicate that they struggle to generalize across all conditions. RUL predictions across various levels and models are presented in **Figure 7.8**. While Level-1 models, particularly at specific frequencies, such as 160 kHz, show strong performance in specific cases, with Level-2 robust, generalized results are achieved by integrating GW signals from multiple excitation frequencies. Despite L1-160 kHz performing well across samples with an average error of 2.139, the L2-MLP model outperforms all with the lowest average error of 1.904. The L2-WAE model also performs strongly, with an average error of 2.384. **Table 7-7** indicates the averaged MAPE error for RUL predictions produced from each level.

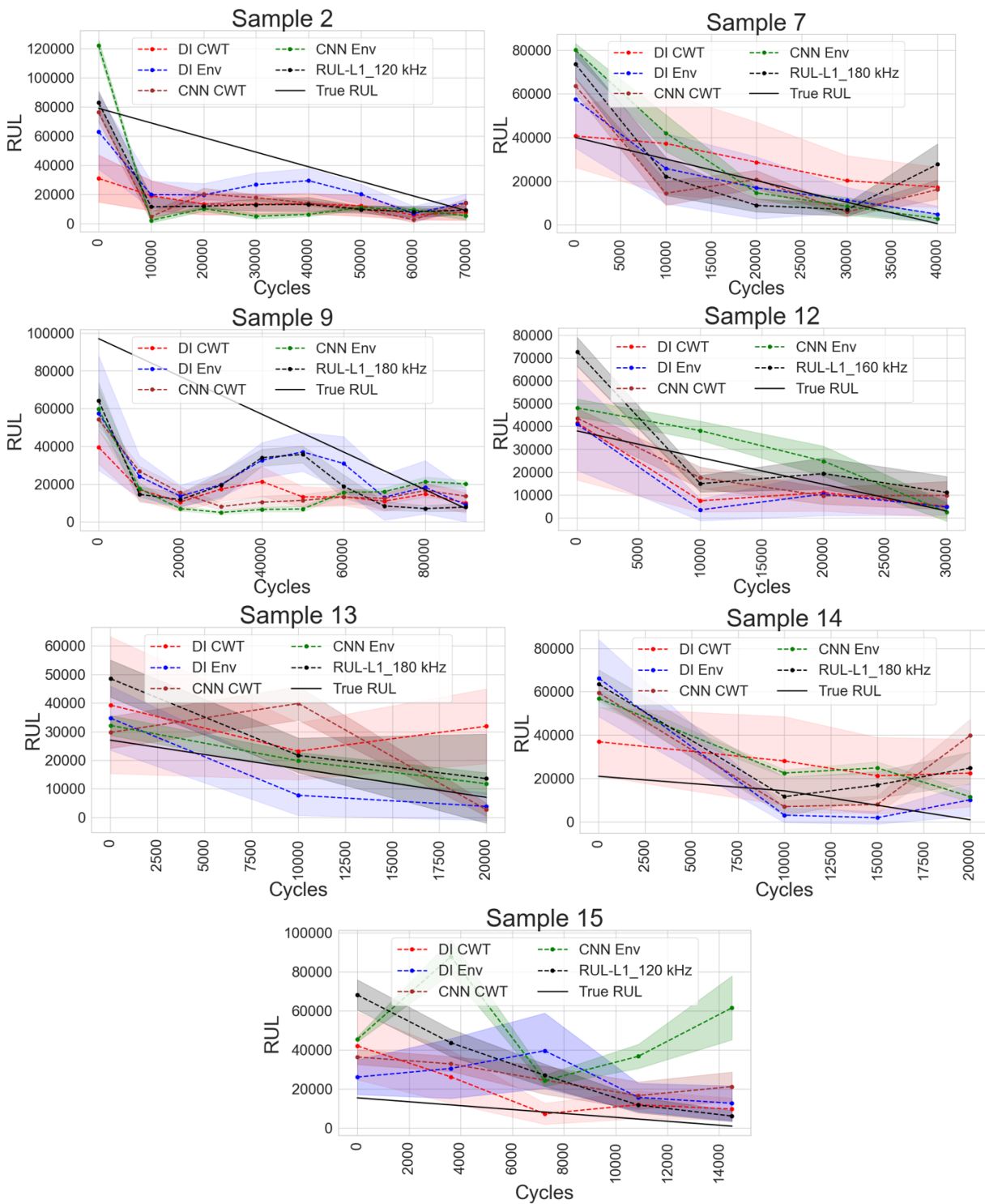


Figure 7.7. Base learner prediction results with Level-1 fusion for the excitation frequency of highest accuracy.

Table 7-6. Base Learner average error values.

		INPUT TYPES				
		CNN-CWT	CNN-Env	DI CWT	DI Env	
EXCITATION FREQUENCY	100 kHz	Sample 2	0.783	0.689	<b>0.671</b>	0.776
		Sample 7	10.567	15.068	<b>4.932</b>	13.035
		Sample 9	0.661	<b>0.641</b>	0.650	0.740
		Sample 12	1.258	1.504	<b>0.418</b>	3.054
		Sample 13	0.470	<b>0.185</b>	1.649	1.106
		Sample 14	4.689	9.587	<b>3.649</b>	7.862
		Sample 15	3.982	<b>1.715</b>	4.396	11.765
		Average	3.276	4.079	<b>2.354</b>	5.858
	120 kHz	Sample 2	0.612	<b>0.464</b>	0.579	0.732
		Sample 7	4.907	6.124	5.395	<b>3.071</b>
		Sample 9	0.660	<b>0.531</b>	0.667	0.861
		Sample 12	<b>0.376</b>	0.907	0.497	1.240
		Sample 13	0.343	<b>0.240</b>	1.298	2.031
		Sample 14	3.462	<b>3.404</b>	3.917	4.881
		Sample 15	2.214	3.286	5.159	4.308
		Average	2.246	2.191	2.361	<b>2.173</b>
	140 kHz	Sample 2	0.603	<b>0.507</b>	0.601	0.587
		Sample 7	<b>3.989</b>	7.902	12.189	10.916
		Sample 9	<b>0.598</b>	0.725	0.681	0.705
		Sample 12	1.968	<b>0.341</b>	1.066	4.291
Sample 13		1.603	<b>0.459</b>	1.331	1.372	
Sample 14		3.462	<b>3.404</b>	3.917	4.881	
Sample 15		2.007	6.778	4.486	3.441	
Average		<b>2.027</b>	2.895	3.211	3.835	
160 kHz	Sample 2	<b>0.576</b>	0.691	0.597	0.688	
	Sample 7	4.479	<b>2.232</b>	6.815	5.751	
	Sample 9	0.615	<b>0.433</b>	0.653	0.787	
	Sample 12	<b>0.469</b>	0.489	0.738	0.703	
	Sample 13	0.858	0.688	<b>0.654</b>	1.342	
	Sample 14	5.373	<b>1.196</b>	5.806	5.340	
	Sample 15	1.971	4.442	2.632	10.698	
	Average	2.132	<b>1.553</b>	2.412	4.674	
180 kHz	Sample 2	0.686	0.745	0.655	<b>0.644</b>	
	Sample 7	7.021	1.911	6.583	<b>1.308</b>	
	Sample 9	0.657	<b>0.611</b>	0.633	0.734	
	Sample 12	<b>0.776</b>	1.227	1.950	1.178	
	Sample 13	1.456	0.429	0.687	<b>0.345</b>	
	Sample 14	5.740	<b>3.356</b>	9.888	3.518	
	Sample 15	<b>2.675</b>	4.037	5.593	15.574	
	Average	2.787	<b>1.860</b>	3.677	3.979	

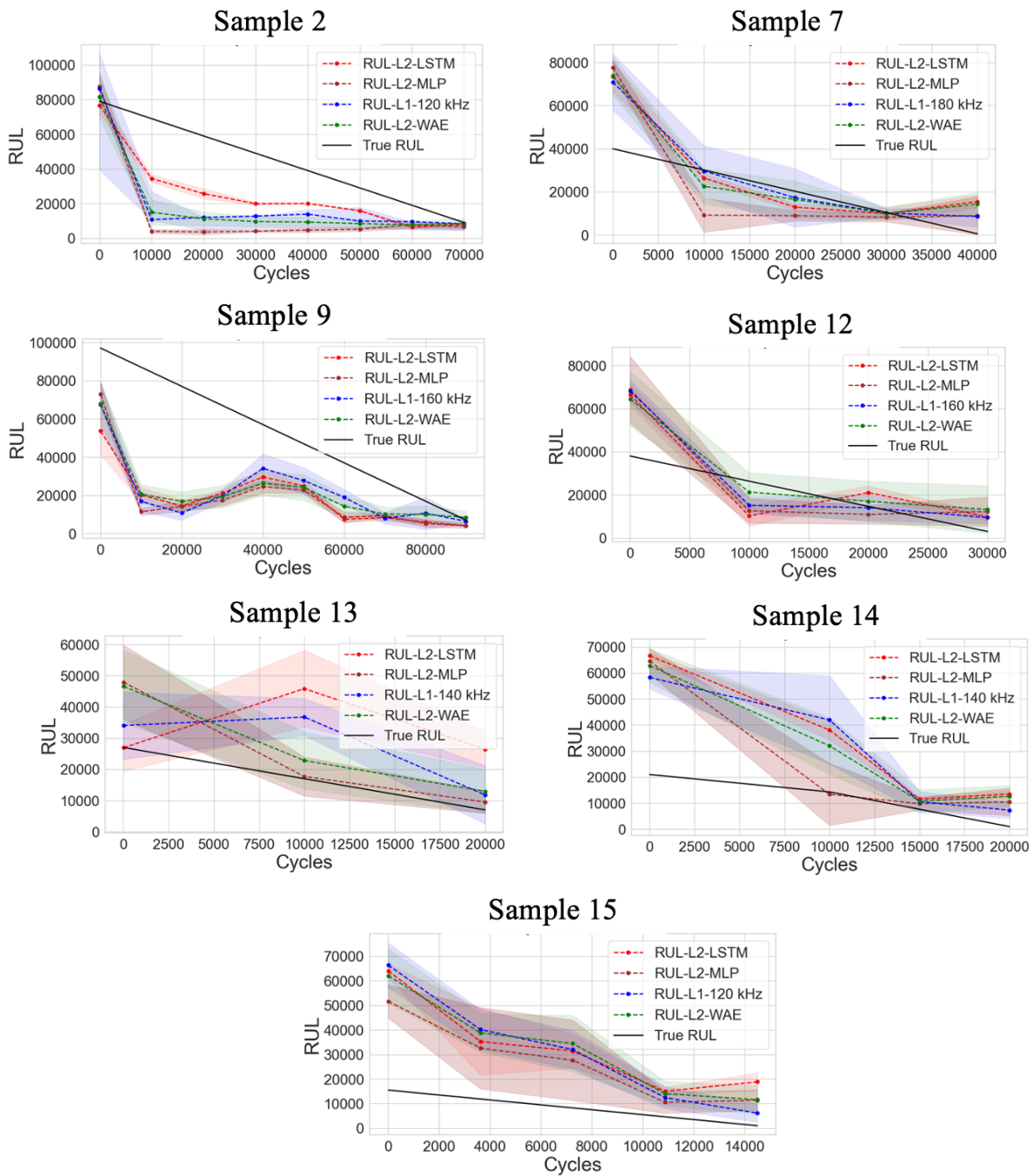


Figure 7.8. RUL prediction from different levels (L1 and L2) composed of different models.

Table 7-7. Averaged MAPE error values for RUL prediction from each fusion level.

FUSION LEVELS		Sample 2	Sample 7	Sample 9	Sample 12	Sample 13	Sample 14	Sample 15	Average
	L1-100kHz	0.622	11.282	0.584	1.279	0.720	6.816	5.987	3.899
L1-120kHz	0.557	6.122	0.582	1.186	1.150	4.298	3.017	2.416	
L1-140kHz	0.562	10.482	0.562	1.475	0.602	2.695	4.031	2.916	
L1-160kHz	0.564	4.237	0.510	1.089	0.767	4.156	4.327	2.236	
L1-180kHz	0.656	2.575	0.525	1.176	0.670	5.589	5.486	2.382	
<b>L2-WAE</b>	0.558	5.046	<b>0.552</b>	1.095	0.687	4.136	4.183	2.322	
<b>L2-MLP</b>	0.701	<b>3.977</b>	0.635	1.231	<b>0.368</b>	<b>3.410</b>	<b>3.544</b>	<b>1.981</b>	
<b>L2-LSTM</b>	<b>0.550</b>	4.066	0.595	<b>0.872</b>	1.952	4.947	5.104	2.584	

## 7.4 Discussion

The LSTM and MLP models show higher adaptability by leveraging more complex, multi-dimensional input information. L2-MLP in particular stands out, delivering the best average performance across all samples. Its ability to capture complex degradation trends suggests that MLP effectively generalizes better than LSTM, which shows higher error rates. The L2-MLP model emerges as the most effective approach, achieving the lowest average error across all samples. Its ability to integrate multi-frequency information and adapt to varying signal dynamics enables it to handle the inherent complexity in GW signals more effectively than single-frequency models. Similarly, the L2-WAE model demonstrates robust performance, achieving low errors across multiple samples due to its ability to balance contributions from all excitation frequencies, thus mitigating the limitations of single-frequency models. This model excels at stabilizing predictions by smoothing out fluctuations, providing reliable RUL estimates across a range of conditions.

Despite these strengths, proposed models exhibit some limitations that need to be addressed. L2-LSTM, while highly adaptable in capturing temporal dependencies, shows greater prediction uncertainty in certain samples, as evidenced by the wider confidence intervals observed in cases such as Sample 13. This higher uncertainty may stem from the model's sensitivity to minor fluctuations in the data, which can result in overfitting, particularly when the degradation trajectory includes abrupt changes or a limited number of time steps. LSTM's focus on temporal dependencies can lead to increased prediction error, while MLP, with its simpler structure, generalizes better in this scenario. Furthermore, while L2-WAE provides a more stable and balanced prediction by aggregating information from multiple excitation frequencies, it may struggle in scenarios where high error arises from averaged predictions, as it is an explicit model that may oversimplify complex degradation patterns by smoothing out important variations.

## 7.5 Conclusion

This study presents a novel multi-level data-driven framework for RUL prediction, utilizing 1D CNN and MLP as base learners. By leveraging delamination state correlations to interpret GW-DIs the framework integrates signal processing techniques with deep learning to produce accurate and interpretable RUL predictions.

The models developed for the first fusion level, Level-1, in particular frequencies perform well in certain instances, indicating that information obtained from specific frequencies of GWs may provide valuable insights into the degradation process. However, the performance of Level-1 models varies more widely across different samples. This inconsistency suggests that while single-frequency models may perform well in less complex conditions, they are insufficient for generalizing across more complex degradation processes that involve complex damage modes like delamination. In the second fusion level, L2-

---

MLP stands out as the top performer, demonstrating its capacity to generalize across various sample behaviors with the lowest overall error. Meanwhile, L2-WAE provides a reliable middle ground, balancing signal information from different frequencies to offer consistent and stable predictions. Ultimately, the need to aggregate information from multiple frequencies, employing both knowledge- and deep learning-based features, is beneficial for achieving the best and most generalized results in RUL prediction, making multi-frequency fusion approaches critical for real-world applications.



## **8 Conclusion & Future Research**

## 8.1 Discussion of Research Outcomes and Limitations

This research aims to develop advanced prognostic frameworks for accurately assessing delamination growth and predicting the RUL of composite structures under compressive fatigue conditions by systematically investigating the complementary capabilities of GW and EMI techniques, enhancing the accuracy and reliability of delamination characterization and RUL prediction. To address the complexity of delamination evolution and its unpredictable progression, this research focused on optimizing signal processing techniques for GW signals, integrated diagnostic and prognostic models, and incorporating AI-driven prognostic methodologies. By leveraging DL frameworks, statistical modeling, and advanced feature extraction techniques, this study aims to enhance the interpretability and robustness of RUL estimations.

This thesis addressed several critical challenges in monitoring impact-induced delamination progression and improving RUL prognostics in composite structures, particularly CFRP structures. The research framed its contributions to the research questions including:

- *How can advanced active-sensing techniques improve the assessment of damage severity in composite structures while addressing the challenges posed by material anisotropy and complex failure mechanisms?*

The experimental investigation of impact-induced delamination propagation under C-C fatigue loading conducted in this thesis provides valuable insights into the development of effective prognostic methodologies. By capturing a broad spectrum of delamination behaviors under both variable and constant loading conditions, this study contributes to a more comprehensive understanding of the degradation mechanisms in composite structures. The observed variability in EoL across tested samples is critical for constructing robust prognostic models, enabling a deeper exploration of how different loading scenarios influence damage evolution and failure patterns despite the fact that one layup taken into consideration for this experiment. The integration of GW-SHM and EMI-SHM has demonstrated that the combination of these techniques enhances delamination characterization, particularly under complex loading conditions.

Advanced signal processing techniques were employed to extract delamination-related features from both GW and EMI signals. Although these methods serve as complementary diagnostic tools, they exhibit distinct characteristics in monitoring delamination progression. EMI-SHM demonstrated high sensitivity to delamination, particularly in cases where damage evolved rapidly and initiated with greater severity. DIs derived from GW signals proved effective in tracking gradual or slower damage accumulation, often indicating a more severe damage state compared to EMI-based DIs. This can be attributed to the ability of GWs to interact with damage in a broader sense, capturing not only delamination but also other coexisting damage mechanisms. As a result, GW-DIs may inherently quantify the combined effects of multiple damage modes, rather than isolating delamination exclusively.

Additionally, the excitation frequency of GW signals is expected to induce different wave modes within the structure. The results indicate that lower excitation frequencies tend to produce lower prognostic metric scores and exhibit relatively less monotonic behavior compared to higher excitation frequencies. While this could be attributed to the increased sensitivity of higher-order wave modes excited at higher frequencies, the physical interaction between delamination and specific GW modes was not investigated in this study. Thus, further research is required to establish a deeper understanding of the underlying mechanisms governing the relationship between DIs and delamination.

Moreover, while labeled delamination states facilitated comparative analysis between GW and EMI signals, the labeling approach was constrained by the limitations of ultrasonic c-scan imaging. Specifically, c-scan measurements were unable to fully capture shadowed or overlapping delamination layers, and the contribution of other damage mechanisms, such as matrix cracking, could not be quantified due to the inherent constraints of the imaging technique. Consequently, the correlation metric used to establish the relationship between measured delamination length and DIs has inherent limitations in providing precise information. Nonetheless, ultrasonic c-scan measurements successfully identified distinct delamination growth regimes across different samples, thereby used as validation the dual-method approach as a more holistic means of assessing delamination severity and progression.

- *How can the severity of delamination be effectively integrated into data-driven RUL prognostic models for composite structures?*

Three prognostic frameworks were developed to investigate the RUL of composite structures by incorporating DIs derived from both GW and EMI techniques. The primary objective was to establish a comprehensive projection of delamination severity using GW-DIs and EMI-DIs and to understand their respective contributions to RUL estimation within a data-driven methodology. The first presented framework, given in Chapter 5, involves the development of a prognostic approach that integrates both GW-DIs and EMI-DIs. The results indicated that RUL predictions exhibited higher accuracy when using EMI-derived inputs in cases where the initial impact energy was higher and damage accumulation was relatively rapid. GW-derived inputs provided overall higher prognostic performance. RUL-fused-1 with WAE and RUL\_fused\_2 with MLP indicates the robustness of the proposed fusion methodology with lower errors while RUL-fused-1 mitigates the less accurate predictions of EMI and GW inputs, RUL\_fused\_2 achieves higher scores in terms of its final cycle convergence and through the fatigue life of the samples. The improvement of RUL\_fused\_2 is calculated considering less effective prediction of EMI and a 48% improvement in final cycle and %24 in overall cycles is achieved.

The second prognostic framework integrates both delamination growth prediction and RUL estimation within a sample-based domain. This approach aims to establish a novel prognostic framework by investigating the path sensitivity of GW signals to the prediction both RUL and delamination severity. The findings reveal that the DIs yielding the highest accuracy for RUL prognostics also perform effectively for delamination prediction; however, the reverse is not always true. This suggests that DIs extracted from GW signals encapsulate global damage characteristics, contributing to RUL estimation.

The final framework in Chapter 7 proposes a novel prognostic methodology, by leveraging delamination state correlations to interpret GW-DIs the framework integrates signal processing techniques with deep learning to produce accurate and interpretable RUL predictions. This enhanced methodology manifolds the learning steps according to the input types and analyze their contribution to RUL outcomes together with the inputs correlation with labelled delamination state. It is shown that DI-Env contributed more significantly to reducing errors in RUL predictions compared to DI-CWT, despite DI-CWT exhibiting a higher correlation metric score with measured delamination length. This discrepancy may suggest that suggested DI-Env is more effective in quantifying damage severity, thereby enhancing its capability to predict RUL more accurately. In contrast, while DI-CWT demonstrates a stronger correlation with measured delamination length, the limitations in one-dimensional quantification have been re-identified in terms of assessing the delamination severity.

- *What methodologies can be applied to improve the accuracy and generalization of RUL prognostics for impacted composite aerospace structures?*

Among the proposed prognostic frameworks, generalization and accuracy enhancement are addressed at multiple levels through distinct methodological approaches. In the context of GW and EMI integration, a fusion framework employing a DNN and a WAE is investigated to achieve optimal RUL prediction accuracy with lower error in Chapter 5. The results demonstrate that the fusion step effectively mitigates adverse effects arising from the distinct sensing characteristics of GW and EMI, thereby enhancing the accuracy and reliability of RUL predictions through deep learning-driven feature integration.

For GW and EMI signals, inherent variability due to sensor inconsistencies, environmental influences, may introduce significant challenges in the DI extraction process. These factors contribute to variations in damage severity assessment, necessitating an improved generalization strategy for GW-DIs and EMI-DIs to ensure consistent and reliable RUL prognostics. Sensor variations were accounted for through the sensor fusion step for both GW and EMI techniques, where all signal paths were assigned equal weighting, and global DIs were incorporated into the fusion process. However, this approach presents certain limitations, as specific GW and EMI signal paths exhibit higher sensitivity to damage accumulation. Consequently, the uniform weighting scheme may lead to lower accuracy by not assigning greater emphasis to more diagnostically sensitive paths. This could result in the loss of critical diagnostic information, potentially diminishing the effectiveness of the fused prognostic model in accurately capturing damage progression and RUL estimation.

In the context of GW-SHM, the frequency dependency of GWs introduces challenges in achieving robust and generalized damage severity analysis and RUL predictions. To address this, multiple excitation frequencies are incorporated as independent prognostic features into DNN based prognostic model and systematically analyzed within the DI–damage severity correlation framework in Chapter 6. This approach leverages multi-frequency information from GW signals to enhance predictive accuracy expecting DNNs to map DI to RUL output giving higher weights to most relevant input information ensuring a more comprehensive representation in RUL estimations.

While a multi-frequency and multi-DI approach is applied in DNN-based prognostic frameworks, the integration methodology varies across the proposed models. In the framework in Chapter 6, RUL prognostics are achieved by treating each DI and frequency set of GWs as independent features within a single DNN model. The framework in Chapter 7 incorporates multiple levels of features, including GW-DIs and complete GW signals, represented as signal envelopes via HT and signal average power via CWT. It is aimed for the framework in Chapter 7 specifically to focus on the generalization of the GW-based RUL prognostic approach. The results show that each input from different excitation frequencies achieved higher prognostic accuracy for different samples, with no single input type or base learner model consistently outperforming the others. This indicates that the proposed multi-level prognostic approach provides a robust methodology for achieving stable RUL predictions using GW inputs, effectively accounting for the variability in CFRP samples tested under different impact damage scenarios and C-C fatigue loading conditions.

Despite efforts to enhance the accuracy and robustness of the proposed methodologies for RUL prognostics of CFRP structures, certain aspects require further development. Notably, the experimental dataset developed to investigate delamination-induced failure in aerospace structures lacks diversity in layup designs and multiple damage scenarios. Expanding the dataset to include these factors would improve its alignment with real-world conditions and enhance the generalizability of the proposed frameworks. In this context, the interpretation and correlation of GW signals with specific damage states would necessitate

more comprehensive approaches, incorporating more complex and multi-level learning methodologies. Although the CAI-adopted fatigue experiment in this thesis provided a valuable dataset for analyzing delamination-induced failure, further development of the proposed frameworks is necessary to ensure their applicability to more complex aerospace structures. Moreover, while the RUL outputs have been analyzed based on the results of each learning methodology across all proposed frameworks, physical interpretability remains limited due to the lack of comprehensive understanding of GW propagation characteristics and impact-induced delamination phenomena in CFRP structures. In the next chapter, recommendations for future research will be provided, focusing on advancing the current knowledge base by addressing the achievements and limitations identified in this thesis.

## 8.2 Suggestions for Future Work

Building upon the findings and limitations identified in this research, the following recommendations are proposed to further advance the field of delamination monitoring and RUL prognostics in composite structures, particularly in aerospace applications:

- While GW-DIs and EMI-DIs have demonstrated potential in capturing delamination progression and assessing its severity, their interaction with delamination remains insufficiently explained from a physical perspective. Future research should explore alternative imaging techniques beyond c-scan, such as X-ray computed tomography or thermography, to enhance the accuracy of delamination state labeling. These advanced imaging methods could help reduce uncertainty in DI-damage correlations by providing a more detailed assessment of delamination while also considering the presence of other damage modes, leading to a more comprehensive understanding of the underlying failure mechanisms in composite structures.
- To enhance the interpretability and accuracy of AI-driven RUL prognostics, integrating physics-based knowledge into DL architectures is a crucial step forward. One of the primary challenges in GW-based SHM lies in capturing the complex interaction between GWs and evolving damage states, particularly in anisotropic composite structures. Therefore, beyond direct equation embedding, hybrid AI models that combine feature learning with physical constraints may offer effective strategy. Instead of relying solely on raw data-driven feature extraction, hybrid models can incorporate physically meaningful parameters such as wave mode conversion, group velocity variations, and material anisotropy effects. By integrating such physics-based features into DL frameworks, models can achieve better interpretability and generalization while reducing dependency on large datasets. This is particularly valuable in aerospace applications, where extensive labeled datasets may be difficult to obtain.
- Another critical factor in advancing AI-based SHM methodologies is the proper processing of input data to ensure model robustness and adaptability in real-world applications. Despite the fact that processed DIs encapsulate domain-specific knowledge, they may overlook critical information present in raw sensor data, which captures a broader spectrum of structural characteristics, including subtle variations in damage evolution. However, raw signals also contain inherent noise, which can obscure meaningful patterns and reduce model accuracy if not properly accounted for. Consequently, AI models deployed in real-world SHM systems must be resilient to sensor noise, environmental fluctuations, and dynamic changes in wave propagation characteristics arising from evolving engineering properties of the structure due to progressive damage accumulation. Effective denoising techniques and adaptive preprocessing strategies are essential to be integrated into AI frameworks to extract relevant damage-related features while mitigating the impact of noise on prognostic accuracy.

- Validation of proposed advanced models in full-scale, operational environments is essential to ensure that improved predictions translate into practical benefits across industries that rely on composite structures, such as aerospace. While laboratory experiments and controlled simulations provide valuable insights, real-world deployment introduces additional challenges, including environmental variability and operational loads.

### 8.3 Final Remarks

This study has advanced the integration of active sensing-based SHM techniques into robust, data-driven prognostic models for monitoring impact-induced damage severity in composite structures under compressive fatigue conditions. The proposed frameworks demonstrate that combining multi-modal SHM data correlated to the damage state of the structure with DL techniques can improve the accuracy and reliability of damage characterization and prognostics, contributing to the development of more effective CBM strategies. While the study presents significant advancements in RUL prognostic, challenges remain in fully capturing the complex interaction between GWs and EMI, delamination, and other damage modes, particularly those resulting from impact damage.

The methodologies and insights presented in this research establish a solid basis for future studies aimed at enhancing the reliability and safety of composite structures through advanced active sensing techniques. By integrating data-driven prognostics with GW-SHM and EMI-SHM, this study underscores the potential of multi-modal monitoring approaches in accurately assessing damage evolution and predicting structural degradation. These findings are particularly relevant for aerospace and other high-performance applications, where real-time condition assessment is critical for ensuring operational safety and efficiency. Advancing the proposed prognostic frameworks will further strengthen the viability of composite structures in critical engineering systems, particularly by improving their long-term performance under complex and variable loading conditions. The ability to effectively monitor and predict progressive damage, including impact-initiated delamination growth, will enable more proactive maintenance strategies and extend the service life of composite structures.

## References

- [1] Airbus, “FAST magazine.” [Online]. Available: <http://www.airbus.com/support/publications>
- [2] D. Piotrowski, “Implementation of SHM at Delta Air Lines”, (2020).
- [3] A. Wan, J. Xiong, and Y. Xu, “Fatigue life prediction of woven composite laminates with initial delamination” *Fatigue & Fracture of Engineering Materials & Structures*, vol. 43, no. 9, pp. 2130–2146, Sep. 2020, doi: 10.1111/ffe.13296.
- [4] K. I. Tserpes, P. Papanikos, G. Labeas, and S. Pantelakis, “Fatigue damage accumulation and residual strength assessment of CFRP laminates” *Composite Structures*, vol. 63, no. 2, pp. 219–230, 2004, doi: 10.1016/S0263-8223(03)00169-7.
- [5] J. Zhang, L. Zhao, M. Li, and Y. Chen, “Compressive fatigue behavior of low velocity impacted and quasi-static indented CFRP laminates” *Composite Structures*, vol. 133, pp. 1009–1015, Dec. 2015, doi: 10.1016/j.compstruct.2015.08.046.
- [6] S. Rivallant, C. Bouvet, E. Abi Abdallah, B. Broll, and J. J. Barrau, “Experimental analysis of CFRP laminates subjected to compression after impact: The role of impact-induced cracks in failure” *Composite Structures*, vol. 111, no. 1, pp. 147–157, 2014, doi: 10.1016/j.compstruct.2013.12.012.
- [7] M. Sadighi and R. Alderliesten, “Impact fatigue, multiple and repeated low-velocity impacts on FRP composites: A review” *Composite Structures*, vol. 296, p. 115962, Oct. 2022, doi: 10.1016/j.compstruct.2022.115962.
- [8] EASA, “General Acceptable Means of Compliance for Airworthiness of Products, Parts and Appliances (AMC-20)”, *European Union Aviation Safety Agency*, Cologne, Germany, 2023. [Online]. Available: <https://www.easa.europa.eu/en/document-library/acceptable-means-of-compliance/amc-20>
- [9] S. Long, X. Yao, and X. Zhang, “Delamination prediction in composite laminates under low-velocity impact” *Composite Structures*, vol. 132, pp. 290–298, Nov. 2015, doi: 10.1016/j.compstruct.2015.05.037.
- [10] M. R. Wisnom, “The role of delamination in failure of fibre-reinforced composites” *Philosophical Transactions of the Royal Society A: Mathematical, Physical and Engineering Sciences*, vol. 370, no. 1965, pp. 1850–1870, Apr. 2012, doi: 10.1098/rsta.2011.0441.
- [11] K. L. Reifsnider and A. Talug, “Analysis of fatigue damage in composite laminates” *International Journal of Fatigue*, vol. 2, no. 1, pp. 3–11, Jan. 1980, doi: 10.1016/0142-1123(80)90003-0.
- [12] E. J. Ekoi, A. N. Dickson, and D. P. Dowling, “Investigating the fatigue and mechanical behaviour of 3D printed woven and nonwoven continuous carbon fibre reinforced polymer (CFRP) composites” *Composites Part B: Engineering*, vol. 212, p. 108704, May 2021, doi: 10.1016/j.compositesb.2021.108704.
- [13] D. Biagini, J. A. Pascoe, and R. C. Alderliesten, “Experimental investigation of fatigue after impact damage growth in CFRP” *Procedia Structural Integrity*, vol. 41, pp. 343–350, 2022, doi: 10.1016/j.prostr.2022.12.042.
- [14] J.K. Kim and M.L. Sham, “Impact and delamination failure of woven-fabric composites”, *Composites Science and Technology*, vol. 62, no. 5–6, pp. 655–661, 2002, doi: 10.1016/S0266-3538(02)00005-8.
- [15] B. Ostré, C. Bouvet, C. Minot, and J. Aboissiére, “Experimental analysis of CFRP laminates subjected to compression after edge impact” *Composite Structures*, vol. 152, pp. 767–778, Sep. 2016, doi: 10.1016/j.compstruct.2016.05.068.
- [16] M. R. Abir, T. E. Tay, M. Ridha, and H. P. Lee, “On the relationship between failure mechanism and compression after impact (CAI) strength in composites” *Composite Structures*, vol. 182, pp. 242–250, Dec. 2017, doi: 10.1016/j.compstruct.2017.09.038.

- [17] X. C. Sun and S. R. Hallett, "Failure mechanisms and damage evolution of laminated composites under compression after impact (CAI): Experimental and numerical study" *Composites Part A: Applied Science and Manufacturing*, vol. 104, pp. 41–59, Jan. 2018, doi: 10.1016/j.compositesa.2017.10.026.
- [18] L. G. Melin and J. S. Schön, "Buckling behaviour and delamination growth in impacted composite specimens under fatigue load: an experimental study" [Online].
- [19] S. Sanchez-Saez, E. Barbero, R. Zaera, and C. Navarro, "Compression after impact of thin composite laminates" *Composites Science and Technology*, vol. 65, no. 13, pp. 1911–1919, Oct. 2005, doi: 10.1016/j.compscitech.2005.04.009.
- [20] S. Rivallant, C. Bouvet, and N. Hongkarnjanakul, "Failure analysis of CFRP laminates subjected to compression after impact: FE simulation using discrete interface elements" *Composites Part A: Applied Science and Manufacturing*, vol. 55, pp. 83–93, 2013, doi: 10.1016/j.compositesa.2013.08.003.
- [21] P. Shabani, L. Li, J. Laliberte, and G. Qi, "Compression after impact (CAI) failure mechanisms and damage evolution in large composite laminates: High-fidelity simulation and experimental study" *Composite Structures*, vol. 339, Jul. 2024, doi: 10.1016/j.compstruct.2024.118143.
- [22] N. Yue, A. Broer, W. Briand, M. Rébillat, T. Loutas, and D. Zarouchas, "Assessing stiffness degradation of stiffened composite panels in post-buckling compression-compression fatigue using guided waves" *Composite Structures*, vol. 293, Aug. 2022, doi: 10.1016/j.compstruct.2022.115751.
- [23] D. Biagini, J. A. Pascoe, and R. Alderliesten, "Investigating apparent plateau phases in fatigue after impact damage growth in CFRP with ultrasound scan and acoustic emissions" *International Journal of Fatigue*, vol. 177, Dec. 2023, doi: 10.1016/j.ijfatigue.2023.107957.
- [24] M. N. Saleh, H. M. El-Dessouky, M. Saeedifar, S. T. De Freitas, R. J. Scaife, and D. Zarouchas, "Compression after multiple low velocity impacts of NCF, 2D and 3D woven composites" *Composites Part A: Applied Science and Manufacturing*, vol. 125, Oct. 2019, doi: 10.1016/j.compositesa.2019.105576.
- [25] A. Li et al., "Review on methodologies of fatigue property prediction for carbon fiber reinforced polymer" *Composites Part B: Engineering*, Sep. 2024, doi: 10.1016/j.compositesb.2024.111659.
- [26] A. P. Vassilopoulos, J. Maier, G. Pinter, and C. Gaier, "Computational tools for the fatigue life modeling and prediction of composite materials and structures" in *Fatigue Life Prediction of Composites and Composite Structures*, Elsevier, 2020, pp. 635–680, doi: 10.1016/B978-0-08-102575-8.00018-8.
- [27] J. A. Pascoe, R. C. Alderliesten, and R. Benedictus, "Methods for the prediction of fatigue delamination growth in composites and adhesive bonds – A critical review" *Engineering Fracture Mechanics*, vol. 112–113, pp. 72–96, Nov. 2013, doi: 10.1016/j.engfracmech.2013.10.003.
- [28] H. Rocha, C. Semprinoschnig, and J. P. Nunes, "Sensors for process and structural health monitoring of aerospace composites: A review" *Engineering Structures*, Jun. 2021, doi: 10.1016/j.engstruct.2021.112231.
- [29] A. Güemes, A. Fernandez-Lopez, A. R. Pozo, and J. Sierra-Pérez, "Structural health monitoring for advanced composite structures: A review" *Journal of Composites Science*, vol. 4, no. 1, p. 13, 2020, doi: 10.3390/jcs4010013.
- [30] M. Saeedifar and D. Zarouchas, "Damage characterization of laminated composites using acoustic emission: A review" *Composites Part B: Engineering*, vol. 195, p. 108039, Aug. 2020, Elsevier Ltd. doi: 10.1016/j.compositesb.2020.108039.
- [31] D. Kinet, P. Mégret, K. W. Goossen, L. Qiu, D. Heider, and C. Caucheteur, "Fiber Bragg grating sensors toward structural health monitoring in composite materials: Challenges and solutions" *Sensors*, vol. 14, no. 4, pp. 7394–7419, Apr. 2014, doi: 10.3390/s140407394.

- [32] W. S. Na and J. Baek, "A review of the piezoelectric electromechanical impedance based structural health monitoring technique for engineering structures" *Sensors*, vol. 18, no. 5, p. 1307, May 2018, doi: 10.3390/s18051307.
- [33] Z. Su, L. Ye, and Y. Lu, "Guided Lamb waves for identification of damage in composite structures: A review" *Journal of Sound and Vibration*, vol. 295, no. 3–5, pp. 753–780, Aug. 2006, doi: 10.1016/j.jsv.2006.01.020.
- [34] C. R. Farrar and N. A. J. Lieven, "Damage prognosis: The future of structural health monitoring" *Philosophical Transactions of the Royal Society A: Mathematical, Physical and Engineering Sciences*, vol. 365, no. 1851, pp. 623–632, Feb. 2007, doi: 10.1098/rsta.2006.1927.
- [35] J. Chiachío, S. Sankararaman, M. Chiachío, A. Saxena, and K. Goebel, "Prognostics design for structural health management" in *Emerging Design Solutions in Structural Health Monitoring Systems*, IGI Global, 2015, pp. 234–273, doi: 10.4018/978-1-4666-8490-4.ch011.
- [36] K. Javed, R. Gouriveau, and N. Zerhouni, "State of the art and taxonomy of prognostics approaches, trends of prognostics applications and open issues towards maturity at different technology readiness levels" *Mechanical Systems and Signal Processing*, vol. 94, pp. 214–236, Sep. 2017, doi: 10.1016/j.ymsp.2017.01.050.
- [37] X. S. Si, W. Wang, C. H. Hu, and D. H. Zhou, "Remaining useful life estimation – A review on the statistical data driven approaches" *European Journal of Operational Research*, vol. 213, no. 1, pp. 1–14, Aug. 2011, Elsevier B.V. doi: 10.1016/j.ejor.2010.11.018.
- [38] C. Ferreira and G. Gonçalves, "Remaining useful life prediction and challenges: A literature review on the use of Machine Learning Methods" *Journal of Manufacturing Systems*, vol. 64, pp. 457–481, Apr. 2022, doi: 10.1016/j.jmsy.2022.05.010.
- [39] N. Eleftheroglou, D. Zarouchas, and R. Benedictus, "An adaptive probabilistic data-driven methodology for prognosis of the fatigue life of composite structures" *Composite Structures*, vol. 245, Aug. 2020, doi: 10.1016/j.compstruct.2020.112386.
- [40] K. Tidriri, N. Chatti, S. Verron, and T. Tiplica, "Bridging data-driven and model-based approaches for process fault diagnosis and health monitoring: A review of researches and future challenges" *Annual Reviews in Control*, vol. 42, pp. 63–81, 2016, doi: 10.1016/j.arcontrol.2016.09.008.
- [41] A. Rahbari, M. Rébillat, N. Mechbal, and S. Canu, "Unsupervised damage clustering in complex aeronautical composite structures monitored by Lamb waves: An inductive approach" *Engineering Applications of Artificial Intelligence*, vol. 97, Jan. 2021, doi: 10.1016/j.engappai.2020.104099.
- [42] T. Loutas, N. Eleftheroglou, and D. Zarouchas, "A data-driven probabilistic framework towards the in-situ prognostics of fatigue life of composites based on acoustic emission data" *Composite Structures*, vol. 161, pp. 522–529, Feb. 2017, doi: 10.1016/j.compstruct.2016.10.109.
- [43] G. Galanopoulos, N. Eleftheroglou, D. Milanoski, A. Broer, D. Zarouchas, and T. Loutas, "A novel strain-based health indicator for the remaining useful life estimation of degrading composite structures" *Composite Structures*, vol. 306, Feb. 2023, doi: 10.1016/j.compstruct.2022.116579.
- [44] E. Zio, "Prognostics and Health Management (PHM): Where are we and where do we (need to) go in theory and practice" *Reliability Engineering & System Safety*, Feb. 2022, doi: 10.1016/j.ress.2021.108119.
- [45] M. Philibert, K. Yao, M. Gresil, and C. Soutis, "Lamb waves-based technologies for structural health monitoring of composite structures for aircraft applications" *Advanced Manufacturing: Polymer & Composites Science*, vol. 8, no. 2, pp. 95–109, 2022, doi: 10.1080/26889277.2022.2094839.
- [46] L. Yu, G. Santoni-Bottai, B. Xu, W. Liu, and V. Giurgiutiu, "Piezoelectric wafer active sensors for in situ ultrasonic-guided wave SHM" *Fatigue & Fracture of Engineering Materials & Structures*, vol. 31, no. 8, pp. 611–628, 2008, doi: 10.1111/j.1460-2695.2008.01256.x.

- [47] R. K. Munian, D. R. Mahapatra, and S. Gopalakrishnan, "Lamb wave interaction with composite delamination" *Composite Structures*, vol. 206, pp. 484–498, Dec. 2018, doi: 10.1016/j.compstruct.2018.08.072.
- [48] V. Samaitis, L. Mažeika, and R. Rekuviene, "Assessment of the length and depth of delamination-type defects using ultrasonic guided waves" *Applied Sciences*, vol. 10, no. 15, Aug. 2020, doi: 10.3390/APP10155236.
- [49] V. Memmolo, E. Monaco, N. D. Boffa, L. Maio, and F. Ricci, "Guided wave propagation and scattering for structural health monitoring of stiffened composites" *Composite Structures*, vol. 184, pp. 568–580, Jan. 2018, doi: 10.1016/j.compstruct.2017.09.067.
- [50] H. Zhang, J. Sun, X. Rui, and S. Liu, "Delamination damage imaging method of CFRP composite laminate plates based on the sensitive guided wave mode" *Composite Structures*, vol. 306, Feb. 2023, doi: 10.1016/j.compstruct.2022.116571. doi: 10.1016/j.compstruct.2022.116571.
- [51] M. Barski and P. Pająk, "Determination of dispersion curves for composite materials with the use of stiffness matrix method" *Acta Mechanica et Automatica*, vol. 11, no. 2, pp. 121–128, 2017, doi: 10.1515/ama-2017-0019.
- [52] A. R. Diogo, B. Moreira, C. A. J. Gouveia, and J. M. R. S. Tavares, "A review of signal processing techniques for ultrasonic guided wave testing" *Metals*, vol. 12, no. 6, Jun. 2022, doi: 10.3390/met12060936.
- [53] Y. Lei, "Signal processing and feature extraction" in *Intelligent Fault Diagnosis and Remaining Useful Life Prediction of Rotating Machinery*, 1st ed., Butterworth-Heinemann, Dec. 2017, pp. 17–66, doi:10.1016/B978-0-12-811534-3.00002-0.
- [54] A. Katunin, "Nondestructive damage assessment of composite structures based on wavelet analysis of modal curvatures: State-of-the-art review and description of wavelet-based damage assessment benchmark" *Shock and Vibration*, vol. 2015, Article ID 210379, 2015, doi: 10.1155/2015/210379.
- [55] A. R. Diogo, B. Moreira, C. A. J. Gouveia, and J. M. R. S. Tavares, "A Review of Signal Processing Techniques for Ultrasonic Guided Wave Testing" *Metals (Basel)*, vol. 12, no. 6, Jun. 2022, doi: 10.3390/met12060936.
- [56] M. Rautela, J. Senthilnath, E. Monaco, and S. Gopalakrishnan, "Delamination prediction in composite panels using unsupervised-feature learning methods with wavelet-enhanced guided wave representations" *Composite Structures*, vol. 291, Jul. 2022, doi: 10.1016/j.compstruct.2022.115579.
- [57] D. Balageas, M. Lemistre, R. Gouyon, and H. Kaczmarek, "Damage localization in composite plates using wavelet transform processing on Lamb wave signals" 1999. [Online]. Available: <https://www.researchgate.net/publication/234047073>
- [58] C. Larrosa, K. Lonkar, and F. K. Chang, "In situ damage classification for composite laminates using Gaussian discriminant analysis" *Structural Health Monitoring*, vol. 13, no. 2, pp. 190–204, Mar. 2014, doi: 10.1177/1475921713517288.
- [59] H. Liu, S. Liu, Z. Liu, N. Mrad, and A. S. Milani, "Data-driven approaches for characterization of delamination damage in composite materials" *IEEE Transactions on Industrial Electronics*, vol. 68, no. 3, pp. 2532–2542, Mar. 2021, doi: 10.1109/TIE.2020.2973877.
- [60] A. Saxena, K. Goebel, C. C. Larrosa, V. Janapati, S. Roy, and F.-K. Chang, "Accelerated aging experiments for prognostics of damage growth in composite materials" [Online dataset or report]
- [61] S. Mishra and O. A. Vanli, "Remaining useful life estimation with Lamb-wave sensors based on Wiener process and principal components regression" *Journal of Nondestructive Evaluation*, vol. 35, no. 1, pp. 1–13, Mar. 2016, doi: 10.1007/s10921-015-0328-2.
- [62] R. Gorgin, Y. Luo, and Z. Wu, "Environmental and operational conditions effects on Lamb wave based structural health monitoring systems: A review" *Ultrasonics*, vol. 105, Jul. 2020, doi: 10.1016/j.ultras.2020.106114.

- [63] C. M. Yeum, H. Sohn, J. B. Ihn, and H. J. Lim, "Instantaneous delamination detection in a composite plate using a dual piezoelectric transducer network" *Composite Structures*, vol. 94, no. 12, pp. 3490–3499, Dec. 2012, doi: 10.1016/j.compstruct.2012.06.003.
- [64] J. B. Ihn and F. K. Chang, "Pitch-catch active sensing methods in structural health monitoring for aircraft structures" *Structural Health Monitoring*, vol. 7, no. 1, pp. 5–19, Mar. 2008, doi: 10.1177/1475921707081979.
- [65] V. Janapati, F. Kopsaftopoulos, F. Li, S. J. Lee, and F. K. Chang, "Damage detection sensitivity characterization of acousto-ultrasound-based structural health monitoring techniques" *Structural Health Monitoring*, vol. 15, no. 2, pp. 143–161, Mar. 2016, doi: 10.1177/1475921715627490.
- [66] R. Tawie, H. B. Park, J. Baek, and W. S. Na, "Damage detection performance of the electromechanical impedance (EMI) technique with various attachment methods on glass fibre composite plates" *Sensors*, vol. 19, no. 5, 2019, doi: 10.3390/s19051000.
- [67] M. Schwankl, Z. Sharif Khodaei, M. H. Aliabadi, and C. Weimer, "Electro-mechanical impedance technique for structural health monitoring of composite panels" in *Key Engineering Materials*, Trans Tech Publications Ltd, 2012, pp. 569–572, doi: 10.4028/[www.scientific.net/KEM.525-526.569](http://www.scientific.net/KEM.525-526.569).
- [68] I. Mueller, "Inspection of piezoelectric transducers used for structural health monitoring systems" Thesis.
- [69] C. K. Soh and Y. Y. Lim, "Fatigue damage diagnosis and prognosis using electromechanical impedance technique" in *Structural Health Monitoring (SHM) in Aerospace Structures*, Elsevier Inc., 2016, pp. 429–446, doi: 10.1016/B978-0-08-100148-6.00015-9.
- [70] L. Yu, M. Gresil, P. Pollock, and M. Sutton, "Progressive damage detection/diagnosis on composite using electromechanical impedance spectroscopy" in *Proceedings of the ASME 2011 International Mechanical Engineering Congress and Exposition (IMECE2011)*, 2011. [Online]. Available: [http://asmedigitalcollection.asme.org/IMECE/proceedings/pdf/IMECE2011/54877/255/2773526/255\\_1.pdf](http://asmedigitalcollection.asme.org/IMECE/proceedings/pdf/IMECE2011/54877/255/2773526/255_1.pdf)
- [71] S. K. Singh and P. H. Malinowski, "An innovative data-driven probabilistic approach for damage detection in electromechanical impedance technique" *Composite Structures*, vol. 295, Sep. 2022, doi: 10.1016/j.compstruct.2022.115808.
- [72] M. Gresil, L. Yu, V. Giurgiutiu, and M. Sutton, "Predictive modeling of electromechanical impedance spectroscopy for composite materials" *Structural Health Monitoring*, vol. 11, no. 6, pp. 671–683, Nov. 2012, doi: 10.1177/1475921712451954.
- [73] Y. J. Cha, R. Ali, J. Lewis, and O. Büyüköztürk, "Deep learning-based structural health monitoring" *Automation in Construction*, vol. 163, May 2024, doi: 10.1016/j.autcon.2024.105328.
- [74] M. Schwabacher and K. Goebel, "A survey of artificial intelligence for prognostics" 2007. [Online]. Available: <https://www.researchgate.net/publication/228346641>
- [75] A. Behnia, H. K. Chai, M. GhasemiGol, A. Sepehrinezhad, and A. A. Mousa, "Advanced damage detection technique by integration of unsupervised clustering into acoustic emission" *Engineering Fracture Mechanics*, vol. 210, pp. 212–227, Apr. 2019, doi: 10.1016/j.engfracmech.2018.07.005.
- [76] A. Tabatabaeian, B. Jerkovic, P. Harrison, E. Marchiori, and M. Fotouhi, "Barely visible impact damage detection in composite structures using deep learning networks with varying complexities" *Composites Part B: Engineering*, vol. 264, Sep. 2023, doi: 10.1016/j.compositesb.2023.110907.
- [77] C. Liu, X. Xu, J. Wu, H. Zhu, and C. Wang, "Deep transfer learning-based damage detection of composite structures by fusing monitoring data with physical mechanism" *Engineering Applications of Artificial Intelligence*, vol. 123, Aug. 2023, doi: 10.1016/j.engappai.2023.106245.
- [78] L. Lomazzi, M. Giglio, and F. Cadini, "Towards a deep learning-based unified approach for structural damage detection, localisation and quantification" *Engineering Applications of Artificial Intelligence*, vol. 121, May 2023, doi: 10.1016/j.engappai.2023.106003.

- [79] Z. Yang, H. Yang, T. Tian, D. Deng, M. Hu, J. Ma, D. Gao, J. Zhang, S. Ma, L. Yang, H. Xu, and Z. Wu, "A review on guided-ultrasonic-wave-based structural health monitoring: From fundamental theory to machine learning techniques" *Ultrasonics*, vol. 133, Aug. 2023, doi: 10.1016/j.ultras.2023.107014.
- [80] Y. Wang, Y. Zhao, and S. Addepalli, "Remaining useful life prediction using deep learning approaches: A review" in *Procedia Manufacturing*, Elsevier B.V., 2020, pp. 81–88, doi: 10.1016/j.promfg.2020.06.015.
- [81] Z. Zhao, B. Liang, X. Wang, and W. Lu, "Remaining useful life prediction of aircraft engine based on degradation pattern learning" *Reliability Engineering & System Safety*, vol. 164, pp. 74–83, Aug. 2017, doi: 10.1016/j.ress.2017.02.007.
- [82] R. Miorelli, C. Fisher, A. Kulakovskiy, B. Chapuis, O. Mesnil, and O. D’Almeida, "Defect sizing in guided wave imaging structural health monitoring using convolutional neural networks" *NDT & E International*, vol. 122, Sep. 2021, doi: 10.1016/j.ndteint.2021.102480.
- [83] J. Wu, X. Xu, C. Liu, C. Deng, and X. Shao, "Lamb wave-based damage detection of composite structures using deep convolutional neural network and continuous wavelet transform" *Composite Structures*, vol. 276, Nov. 2021, doi: 10.1016/j.compstruct.2021.114590.
- [84] M. Moradi, F. C. Gul, and D. Zarouchas, "A novel machine learning model to design historical-independent health indicators for composite structures" *Composites Part B: Engineering*, vol. 275, Apr. 2024, doi: 10.1016/j.compositesb.2024.111328.
- [85] S. Hassani, U. Dackermann, M. Mousavi, and J. Li, "A systematic review of data fusion techniques for optimized structural health monitoring" *Information Fusion*, vol. 103, Mar. 2024, doi: 10.1016/j.inffus.2023.102136.
- [86] A. A. R. Broer, R. Benedictus, and D. Zarouchas, "The need for multi-sensor data fusion in structural health monitoring of composite aircraft structures" *Aerospace*, vol. 9, no. 4, Apr. 2022, doi: 10.3390/aerospace9040183.
- [87] A. Broer, G. Galanopoulos, R. Benedictus, T. Loutas, and D. Zarouchas, "Fusion-based damage diagnostics for stiffened composite panels" *Structural Health Monitoring*, vol. 21, no. 2, pp. 613–639, Mar. 2022, doi: 10.1177/14759217211007127.
- [88] M. Moradi, A. Broer, J. Chiachío, R. Benedictus, T. H. Loutas, and D. Zarouchas, "Intelligent health indicator construction for prognostics of composite structures utilizing a semi-supervised deep neural network and SHM data" *Engineering Applications of Artificial Intelligence*, vol. 117, Jan. 2023, doi: 10.1016/j.engappai.2022.105502.
- [89] ASTM International, "Standard test method for compressive residual strength properties of damaged polymer matrix composite plates," ASTM D7137/D7137M-17, doi: 10.1520/D7137\_D7137M-17.
- [90] V. Giurgiutiu, "Lamb wave generation with piezoelectric wafer active sensors for structural health monitoring"
- [91] G. B. Santoni, L. Yu, B. Xu, and V. Giurgiutiu, "Lamb wave-mode tuning of piezoelectric wafer active sensors for structural health monitoring" *Journal of Vibration and Acoustics*, vol. 129, no. 6, pp. 752–762, 2007, doi: 10.1115/1.2748469.
- [92] I. Mueller and C. P. Fritzen, "Inspection of piezoceramic transducers used for structural health monitoring" *Materials*, vol. 10, no. 1, 2017, doi: 10.3390/ma10010071.
- [93] J. L. Rose, *Ultrasonic Guided Waves in Solid Media*. Cambridge University Press, 2014, doi: 10.1017/CBO9781107273610.
- [94] V. Giurgiutiu, "Structural health monitoring (SHM) of aerospace composites" in *Polymer Composites in the Aerospace Industry*, Elsevier, 2019, pp. 491–558, doi: 10.1016/B978-0-08-102679-3.00017-4.
- [95] A. Katunin, "Nondestructive damage assessment of composite structures based on wavelet analysis of modal curvatures: State-of-the-art review and description of wavelet-based damage assessment benchmark" *Shock and Vibration*, vol. 2015, 2015, doi: 10.1155/2015/735219.

- [96] D. Balageas, M. Lemistre, R. Gouyon, and H. Kaczmarek, "Damage localization in composite plates using wavelet transform processing on Lamb wave signals," 1999. [Online].
- [97] J. M. Lilly and S. C. Olhede, "Generalized morse wavelets as a superfamily of analytic wavelets" *IEEE Transactions on Signal Processing*, vol. 60, no. 11, pp. 6036–6041, 2012, doi: 10.1109/TSP.2012.2210890.
- [98] M. J. Shensa, "The discrete wavelet transform: Wedding the à trous and Mallat algorithms" *IEEE Transactions on Signal Processing*, vol. 40, no. 10, pp. 2464–2482, 1992, doi: 10.1109/78.151719.
- [99] A. Sharma, S. Kumar, and A. Tyagi, "Noise filtering techniques for Lamb waves in structural health monitoring" *Multidiscipline Modeling in Materials and Structures*, vol. 14, no. 4, pp. 676–694, Oct. 2018, doi: 10.1108/MMMS-08-2017-0089.
- [100] V. N. Vapnik, *The Nature of Statistical Learning Theory*, 2nd ed., Springer, 2010, doi: 10.1007/978-1-4757-3264-1.
- [101] J. Zhang, P. Wang, R. Yan, and R. X. Gao, "Long short-term memory for machine remaining life prediction" *Journal of Manufacturing Systems*, vol. 48, pp. 78–86, Jul. 2018, doi: 10.1016/j.jmsy.2018.05.011.
- [102] X. Glorot, A. Bordes, and Y. Bengio, "Deep sparse rectifier neural networks" in *Proceedings of the Fourteenth International Conference on Artificial Intelligence and Statistics (AISTATS 2011)*, 2011.
- [103] A. Krizhevsky, I. Sutskever, and G. E. Hinton, "ImageNet classification with deep convolutional neural networks" [Online].
- [104] S. Kiranyaz, O. Avci, O. Abdeljaber, T. Ince, M. Gabbouj, and D. J. Inman, "1D convolutional neural networks and applications: A survey" *Mechanical Systems and Signal Processing*, vol. 151, Apr. 2021, doi: 10.1016/j.ymsp.2020.107398.
- [105] H. Ismail Fawaz, G. Forestier, J. Weber, L. Idoumghar, and P. A. Muller, "Deep learning for time series classification: A review" *Data Mining and Knowledge Discovery*, vol. 33, no. 4, pp. 917–963, Jul. 2019, doi: 10.1007/s10618-019-00619-1.
- [106] S. Hochreiter and J. Schmidhuber, "Long short-term memory" *Neural Computation*, vol. 9, no. 8, pp. 1735–1780, Nov. 1997, doi: 10.1162/neco.1997.9.8.1735.
- [107] D. P. Kingma and J. Ba, "Adam: A method for stochastic optimization" Dec. 2014, [Online]. Available: <http://arxiv.org/abs/1412.6980>
- [108] N. Srivastava, G. Hinton, A. Krizhevsky, I. Sutskever, and R. Salakhutdinov, "Dropout: A simple way to prevent neural networks from overfitting" *Journal of Machine Learning Research*, vol. 15, pp. 1929–1958, 2014, doi: 10.5555/3045390.3045400.
- [109] F. T. Lima and V. M. A. Souza, "A large comparison of normalization methods on time series" *Big Data Research*, vol. 34, p. 100407, 2023, doi: 10.1016/j.bdr.2023.100407.
- [110] ASTM International, "Standard test method for compressive residual strength properties of damaged polymer matrix composite plates," ASTM D7137/D7137M-17, doi: 10.1520/D7137\_D7137M-17.
- [111] F. C. Gul and D. Zarouchas, "C-C fatigue testing for impacted woven-type CFRP samples," Version 1, 2024, 4TU.ResearchData, dataset, doi: 10.4121/bb64d43c-2ecc-4841-9744-a2377cac9167.v1.
- [112] Henkel Corporation, *LOCTITE® EA 9394 AERO epoxy paste adhesive (known as Hysol® EA 9394) [Product data sheet]*. [Online]. Available: <https://www.henkel-adhesives.com>. [Accessed: Apr. 20, 2025].
- [113] PI Ceramic, *Piezoelectric ceramic products: Piezo technology [Product brochure]*. [Online]. Available: <https://www.piceramic.com>. [Accessed: Apr. 20, 2025].
- [114] B. Zima and M. Rucka, "Application of wavelet transform in analysis of guided wave propagation signals for damage detection in a steel plate" *Diagnostyka*, vol. 16, no. 2, pp. 43–48, 2015.
- [115] A. Grossmann and J. Morlet, "Decomposition of Hardy functions into square integrable wavelets of constant shape" *SIAM Journal on Mathematical Analysis*, vol. 15, no. 4, pp. 723–736, 1984, doi: 10.1137/0515056.

- 
- [116] J. Zhou, Z. Li, and J. Chen, “Application of two dimensional Morlet wavelet transform in damage detection for composite laminates” *Composite Structures*, vol. 318, Aug. 2023, doi: 10.1016/j.compstruct.2023.117091.
- [117] H. Chen, M. J. Zuo, X. Wang, and M. R. Hoseini, “An adaptive Morlet wavelet filter for time-of-flight estimation in ultrasonic damage assessment” *Measurement*, vol. 43, no. 4, pp. 570–585, May 2010, doi: 10.1016/j.measurement.2010.01.001.
- [118] A. Saxena, J. Celaya, E. Balaban, K. Goebel, B. Saha, S. Saha, and M. Schwabacher, “Metrics for evaluating performance of prognostic techniques” in *Proceedings of the 2008 International Conference on Prognostics and Health Management (PHM 2008)*, Denver, CO, USA, 2008, doi: 10.1109/PHM.2008.4711436.
- [119] J. Coble and J. W. Hines, “Identifying optimal prognostic parameters from data: A genetic algorithms approach”. *Proceedings of the Annual Conference of the Prognostics and Health Management (PHM) Society*, 2009

# Acknowledgments

Finishing this thesis has been a deeply meaningful milestone. When I first started to this PhD journey, reaching this point felt like a distant goal. I began with energy and determination, ready to face the challenges ahead. As expected, the journey was not always easy. There were moments of progress and moments of doubt, and plenty of in-between times that tested both my perseverance and my confidence. Every part of the experience has helped me grow, and I'm truly grateful for everything it has taught me. I am thankful to the people who stood by me through it all, offering support during the difficult times and celebrating the successes, no matter how big or small.

First and foremost, I would like to express my sincere gratitude to my PhD advisor, Dr. Dimitrios Zarouchas. From the beginning, I envisioned an ideal supervisor as someone who upholds high standards, fosters personal and academic growth, generously shares knowledge, and maintains empathy throughout the journey. In Dr. Zarouchas, I found all of these qualities and more. His insightful and constructive feedback was always delivered with patience and respect, and even during times of uncertainty, especially when I questioned my own abilities, he offered encouragement and perspective. His unwavering belief in my potential often provided the support I needed to persist. I am deeply thankful for his guidance, mentorship, and trust throughout the course of my PhD.

I would like to extend my heartfelt thanks to my promotor, Professor Rinze Benedictus. His welcoming attitude and steady encouragement from the very beginning made a lasting difference. I am truly grateful for his guidance, and the confidence he showed in me throughout this journey.

I would like to sincerely thank Dr. Rafik Hadjria and Dr. Yevgeniya Lugovtsova, who served as my daily supervisors during the first three years of my PhD. Dr. Hadjria's professional guidance, rigorous feedback, and technical expertise were instrumental in shaping the foundations of my research. Dr. Lugovtsova's technical guidance, continuous availability, encouragement, and personal support made a profound difference throughout this demanding journey. Their supervision not only strengthened the quality and direction of my work, but also provided me with invaluable academic and personal support that I will carry well beyond this thesis.

Throughout the journey of this research, I have had the privilege of working alongside colleagues whose support, collaboration, and technical expertise played a crucial role in shaping the outcome of this thesis. I would like to extend my sincere thanks to Alexandre, Dave, and Chantal for their consistent support and assistance during long hours in the laboratory. Their reliability, hands-on help, and attention to detail made a significant difference in the progress and success of many experiments. I am also grateful to Rose, Sylvia, Wenjie, Deniz, Daniele, Onur, Eva, Davide, Nan, Nick and Morteza for the many stimulating technical discussions, the willingness to share knowledge, and for fostering a collaborative spirit that enriched both the scientific process and the daily work environment. I would like to especially thank Davide for his support during the experiments, and Morteza for his valuable technical insights and the open collaboration that significantly supported the advancement of my research.

I would like to express my sincere gratitude to Safran providing the opportunity and support that allowed me to embark on this research journey. Their commitment and resources played a crucial role in enabling me to develop and carry out my doctoral research in the best possible conditions. I would like to thank Olivier, Oscar, Maya, Wendy, Raouia, Ioannis and Jean-Claude for their consistent kindness, openness, and willingness to help.

I would like to sincerely acknowledge the GW4SHM project for providing the opportunity that enabled me to take part in this PhD research. I am thankful to Dr. Jens Prager, the project manager, and Dr. Yevgeniya Lugovtsova, as the project coordinator, for their dedicated leadership and continuous support throughout the project. To my dear colleagues and friends from the GW4SHM project, Enes, Ahmed, Masoud, Aadhik, Mateen, Mohsen, Vivek, André, Daniel, Omar, Emiel, and Panpan, thank you for enriching this experience with your expertise, friendship, and collaborative spirit. Each of you played a valuable role in the project, and I am deeply grateful for the insightful discussions, shared travels, dinners, and all the light-hearted moments in between. Your presence made this journey not only intellectually fulfilling but also personally unforgettable. Thank you for your dedication and the warmth you brought into this shared chapter.

I owe my deepest gratitude to my husband Ahmet Kursad, my partner in every sense. Your unwavering support, strength, and steady belief in me carried me through the most difficult and defining moments of this journey. From the breakdowns to the breakthroughs, your love has been a constant. Together, we've learned that no matter where life takes us, we are always home as long as we are with each other.

To Esra my dear friend and one of the most constant figures in my life. We have stood by each other through every difficulty, offering strength, honesty, and unwavering support. You were one of my biggest supporters when I moved abroad, and throughout this journey, we have always found ways to lift each other up academically, emotionally, and beyond. I am so proud of all that we've overcome together, and I can't wait to celebrate what's ahead—*polymer-party* we planned 15 years ago!

To my family my mother Zeliha, my father Zekeriya and my two wonderful brothers Huseyin and Eren, thank you for your endless love, patience, and encouragement. You have always been there with open arms, wise words, and humor when I needed it most. Thank you especially for graciously sitting through my tea-time research "presentations," even when the content made little sense. Your presence, even from afar, has meant more than words can say. To my mother-in-law and father-in-law Sevgi, Bekir and brother Cagatay, thank you for your support, kindness, and love throughout this journey. Your presence and encouragement have meant more than I can express.

Kutay and Gizem, your unwavering support has meant the world during some of our most difficult and most joyful moments. A heartfelt thank you to Burak and Melike, with whom I shared not only the PhD struggles but also countless laughs, motivation, and unforgettable moments that made this journey truly special. I am also grateful to my dear friend Gülsah, who stood by me during the most challenging phases of my experimental work in Delft, offering encouragement when I needed it most. Gladys and Nestor, with whom I shared cheerful and meaningful moments in Paris, I truly value the connection we built. To our beloved friends who became like family in Paris, Ezgi, Can, Esin, Orkun, Gizem, Brice, Dilek, Aynur, and Emre, thank you for filling our lives with joy, laughter, and unforgettable memories. From our amazing trips and château weekends to boat tours and spontaneous gatherings, every moment we shared made the challenges of this journey lighter and helped us feel a deeper sense of belonging in this new chapter of our lives. To my dear friends back home, Aycan, Şebnem, and Banu, thank you for being just a call away. Your constant love and encouragement have never failed to reach me, no matter the distance. I am also thankful to my former colleagues, Nisa Onal and Kamil Karacuha, who, despite the physical distance, were always close in spirit throughout this demanding process and

This PhD has been one of the most challenging and rewarding chapters of my life. I am deeply thankful to everyone who walked this path with me, offering support, encouragement, and companionship along the way. Through it all, I was lucky to have my little travel companion, my purry kitty Vegas, by my side, blissfully unaware of how many borders she crossed, yet always there, making every place feel just a bit more like home.

## Curriculum Vitae



She was born in June 1992 in Istanbul, Türkiye. She completed her undergraduate studies in Physics Engineering at Istanbul Technical University (ITU). She then pursued her master's degree in Information and Communication Engineering at the Informatics Institute of ITU. Her research focused on applied electromagnetics, and she worked on advanced antenna designs for radar and mobile communication systems operating at high frequencies. During this period, she also worked as a full-time research assistant at the Informatics Institute.

After completing her master's degree, she was awarded a Marie Skłodowska-Curie grant under the European Union's Horizon 2020 research and innovation program. Through the Marie Skłodowska-Curie Innovative Training Network, she joined the GW4SHM project and began her PhD in collaboration with Safran (Paris, France) and TU Delft (Delft, the Netherlands). At TU Delft, she became a member of the Structural Integrity & Composites section and the Center of Excellence in Artificial Intelligence for Structures, Prognostics & Health Management. Her PhD is supervised by Dr. Dimitrios Zarouchas, with Prof. Rinze Benedictus as her promotor. At Safran, she works in the Digital Sciences & Technologies Department, Safran Tech, within the Safran Sensing Systems research unit, focusing on structural health monitoring technologies.

Her research interests include artificial intelligence, signal processing, guided waves, structural health monitoring, prognostics and health management, non-destructive testing, applied electromagnetics, sensors and antennas, and composite structures. She is particularly interested in exploring the boundaries of current knowledge, where uncertainty and complexity often define the most critical engineering and scientific challenges. Her motivation is to better understand, predict, and manage the behavior of complex systems under real-world conditions. This pursuit of insight into the unknown remains at the core of her research vision.



## List of Publications

- [1] Gül, F. C., Moradi, M., & Zarouchas, D. (2025). *Active sensing-based prognostics for impacted CFRP structures under compressive fatigue loading*. Structural Health Monitoring. <https://doi.org/10.1177/14759217251317747>
- [2] Gül, F. C., Moradi, M., & Zarouchas, D. (2025) *Prognosis of delamination induced failure blending deep learning with signal processing*. Under review.
- [3] Gül, F. C., Moradi, M., & Zarouchas, D. (2024). *An integrated approach for prognosis of remaining useful life for composite structures under in-plane compressive fatigue loading*. Composites Structures: Part C. <https://doi.org/10.1016/j.jcomc.2024.100531>
- [4] Gül, F. C., & Zarouchas, D. (2024). *C-C fatigue testing for impacted woven-type CFRP samples*. 4TU.ResearchData. <https://doi.org/10.4121/BB64D43C-2ECC-4841-9744-A2377CAC9167.V1>
- [5] Moradi, M., Gül, F. C., & Zarouchas, D. (2024). *A novel machine learning model to design historical-independent health indicators for composite structures*. Composites Part B: Engineering, 275, 111328. <https://doi.org/10.1016/j.compositesb.2024.111328>
- [6] Gül, F. C., Moradi, M., Hadjria, R., Lugovtsova, Y., Benedictus, R., & Zarouchas, D. (2023). *Delamination size prediction for compressive fatigue loaded composite structures via ultrasonic guided wave based structural health monitoring*. In Proceedings of the International Workshop on Structural Health Monitoring (IWSHM). <https://doi.org/10.12783/shm2023/36863>
- [7] Gül, F. C., Moradi, M., Hadjria, R., Lugovtsova, Y., Benedictus, R., & Zarouchas, D. (2023). *Data-driven remaining useful life prognostic for aeronautical composite structures based on guided waves*. e-Journal of Non-destructive Testing, 28(8). <https://www.ndt.net/?id=28383>
- [8] Moradi, M., Gül, F. C., Chiachío, J., Benedictus, R., & Zarouchas, D. (2023). *A novel machine learning model to design historical-independent health indicators for composite structures*. In Proceedings of the International Workshop on Structural Health Monitoring (IWSHM). <https://doi.org/10.12783/shm2023/36862>
- [9] Gül, F. C., Benedictus, R., Hadjria, R., Lugovtsova, Y., & Zarouchas, D. (2022). *Data-driven prognostics of delamination growth under fatigue loading with emphasis on aeronautical composite structures – methodology*. International Conference of Condition based Maintenance (ICCBM) .
- [10] Yıldız, E. M., Gül, F. C., Karaçuha, K., & Eker, S. (2022). *A gain enhancement study on a Vivaldi antenna for radar applications*. IEEE International Symposium on Antennas and Propagation and USNC-URSI Radio Science Meeting. IEEE. [doi: 10.1109/AP-S/USNC-URSI47032.2022.9887110](https://doi.org/10.1109/AP-S/USNC-URSI47032.2022.9887110)
- [11] Gül, F. C., & Eker, S. (2020). *Microstrip fed circular patch antenna for 5G and wireless communication*. In 2020 28th Signal Processing and Communications Applications Conference (SIU) (pp. 1–4). IEEE. <https://doi.org/10.1109/SIU49456.2020.9302444>
- [12] Gül, F. C., Karaçuha, K., & Eker, S. (2020). *A two-element array design of dual-band quasi-Yagi antenna with reflector*. IEEE International Symposium on Antennas and Propagation and North American Radio Science Meeting (pp. 1915–1916). IEEE. <https://doi.org/10.1109/IEEECONF35879.2020.9330424>